Theses and Dissertations   Student Graduate Works

3-24-2016

Fatigue behavior of an advanced SiC/SiC composite at 1300° C in air and steam

Michael Lee

Follow this and additional works at: https://scholar.afit.edu/etd

Part of the Structures and Materials Commons

Recommended Citation

Lee, Michael, "Fatigue behavior of an advanced SiC/SiC composite at 1300° C in air and steam" (2016). *Theses and Dissertations*. 447.
https://scholar.afit.edu/etd/447

Fatigue Behavior of an Advanced SiC/SiC Composite at 1300° C in Air and Steam

THESIS

Lee Michael, 2d Lt, USAF

AFIT-ENY-MS-16-M-223

DEPARTMENT OF THE AIR FORCE
AIR UNIVERSITY

AIR FORCE INSTITUTE OF TECHNOLOGY

Wright-Patterson Air Force Base, Ohio

The views expressed in this thesis are those of the author and do not reflect the official policy or position of the United States Air Force, Department of Defense, or the United States Government. This material is declared a work of the U.S. Government and is not subject to copyright protection in the United States.

AFIT-ENY-MS-16-M-223

FATIGUE BEHAVIOR OF AN ADVANCED SIC/SIC COMPOSITE WITH AN OXIDATION INHIBITED MATRIX AT 1300°C IN AIR AND IN STEAM

THESIS

Presented to the Faculty

Department of Aeronautical and Astronautical Engineering

Graduate School of Engineering and Management

Air Force Institute of Technology

Air University

Air Education and Training Command

In Partial Fulfillment of the Requirements for the

Degree of Master of Science in Material Science and Engineering

Michael Lee, B.S.

2d Lt, USAF

March 2016

FATIGUE BEHAVIOR OF AN ADVANCED SIC/SIC COMPOSITE WITH AN OXIDATION INHIBITED MATRIX AT 1300˚C IN AIR AND IN STEAM

Michael D. Lee, BS

2d Lt, USAF

Committee Membership:

Marina B. Ruggles-Wrenn, PhD

Chair

Lt Col Sheena Winder

Member

Thomas Eason, PhD

Member

Abstract

The fatigue behavior of an advanced silicon carbide/silicon carbide (SiC/SiC) ceramic matrix composite (CMC) was investigated at 1300 ºC in laboratory air and in steam environments. The composite was manufactured using chemical vapor infiltration (CVI). The composite consisted of an oxidation-inhibited matrix, which was comprised of alternating layers of silicon carbide and boron carbide and was reinforced with laminated Hi-Nicalon™ fibers woven in a plain weave. Fiber preforms had pyrolytic carbon fiber coating with boron carbon overlay applied. Two specimen geometries were evaluated, a dog bone and an hourglass geometry. Tensile stress-strain behavior and tensile properties were evaluated at 1300 ºC. Tension-tension fatigue tests were conducted in both laboratory air and in steam at 1300 ºC at 1.0 Hz with a minimum to maximum stress ratio of R = 0.05. Fatigue behavior was evaluated for a maximum stress of 70-160 MPa in air and in steam environments. Fatigue run-out was defined as 2×10^5 cycles. Strain accumulation with cycles and modulus evolution with cycles were analyzed for each fatigue test. The CMC fatigue performance was affected little by the presence of steam. The fatigue limit was between 80 and 100 MPa. Retained tensile properties were characterized for all specimens that achieved fatigue run-out. Failure surfaces were examined to study composite microstructure as well as damage and failure mechanisms.

Acknowledgments

I would like to thank my Kayla for all of the support that she has given me since last May. Without her insurmountable workload in PT school, I would never have been able to keep my own workload in perspective. I would also like to thank my advisor Dr. Marina Ruggles-Wrenn for all of the hard work and dedication she provided to me for this research effort. I would also like to extend a big thank you to Dr. Craig Przybyla (AFRL/RXCCP) for sponsoring this thesis research and for providing the test specimens. I would also like to thank Jaime Smith and Barry Page for all the time effort they put into to helping me understand the equipment and fixing my bungling mistakes. Another special thanks goes to Kathleen Shugart at AFRL for taking time out of her busy schedule to help both me and Jaime Smith learn to operate the SEM. One final thanks goes to Connor Wiese. Without his constant small talk and jokes, insanity might have taken me long ago.

Table of Contents

List of Figures

xiii

List of Tables

FATIGUE BEHAVIOR OF AN ADVANCED SIC/SIC COMPOSITE WITH AN OXIDATION INHIBITED MATRIX AT 1300˚C IN AIR AND IN STEAM

I. Introduction

In the world of aviation, maximizing performance is an important consideration when designing or modifying aircrafts. Aircraft performance can be increased either by increasing the power output of the engines or decreasing the overall weight of the aircraft. Currently engine designs are reaching an upper limit on the amount of thrust due to temperature constraints on the air that is pushed out of the engine. The current class of metallic materials cannot function under any higher temperature demands [18]. This requires the exploration and design of newer materials that can sustain good mechanical performance at higher temperatures. If these materials were to weigh less than their metallic counterparts, it would be even more beneficial. From the manufacturer data, the dry engine weight of the F-22 and F-16 is 12% and 20% respeicitvely. Being able to design a material to reduce these weight percentages could greatly increase performance without affecting mechanical failure rates. New age materials, like ceramic matrix composites (CMCs), have shown promise in fulfilling this need for a lighter thermally stable material.

The materials side of the aviation world has always been an evolving process. Pre-World War I planes were predominantly made from wood, which was the lightest and strongest material made in bulk at the time. However, with the increase in steel processing, steel became the desired material for aircraft fuselages. Unfortunately, its increased weight was a major downside to the increase in material strength. This quickly gave way to aluminum which provided good strength with much better weight, a more desired material characteristic for aircraft. The

1

predominance of aluminum continued into World War II and today. After WWII titanium alloys were added to the growing list of advantageous materials for aircraft. Titanium offered better high temperature stability than aluminum with better strength, but with a slight increase in weight. It soon became apparent that the best option for continued reduction in weight would have to be a material that was not a metallic alloy.

The world of composites was born from this need and a constantly evolving understanding of how to manipulate material behaviors and properties. Effectively, the aircraft industry has returned to its roots in terms of structural materials. Wood, the first natural composite, has been eventually replaced by man-made composites. Composites have proved irreplaceable in providing strength and safety while minimizing weight of the structural components of many modern aircrafts. Figure 1 below shows the increased dependence on composites in the aircraft industry.
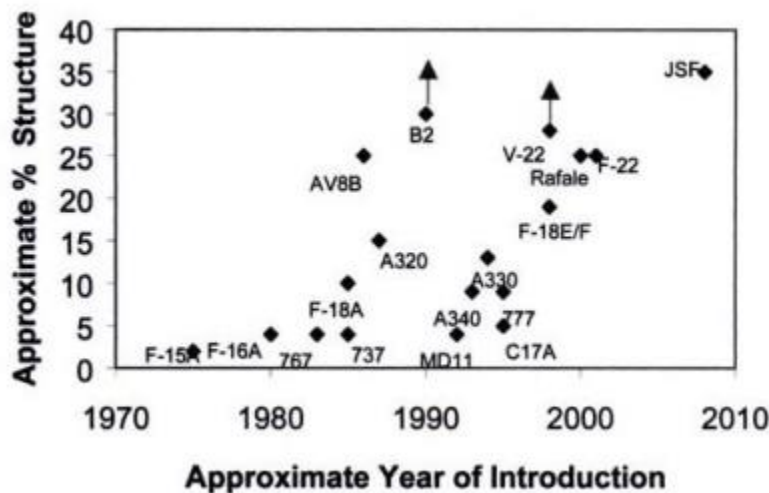
Figure 1. Advanced composite use in aircraft structure. From Baker, A., S. Dutton, and D. Kelly. *Composite Materials for Aircraft Structures (Second Edition)***; reprinted with permission of the American Institute of Aeronautics and Astronautics, Inc. [2]**

Now the same evolving understanding is taking root with engine components. Current engine materials, i.e. metals, are at their operational limits in terms of thermal stability. Improving engine performance has become about minimizing weight and increasing exhaust temperature and speed [13]. Designing new composite materials that can provide these will decrease weight, increase aircraft fuel efficiency, and increase the performance envelope for new generation aircraft. These new composite materials will need to maintain good mechanical strength, both static and fatigue, at high temperatures, provide similar or better damage tolerance and resistance, have low densities, and resist oxidative environments [2].

CMCs currently hold the most promise for being able to achieve the desired properties for engine applications. However, there are some factors holding CMCs back from being the perfect replacement material. These factors are lack of fibers with high elastic moduli and strength, chemical stability, and oxidation resistance at high temperatures [2]. Micro-cracking in the matrix makes it difficult to isolate the fibers from the external environment, allowing for oxidation of the fibers. Current processing and design techniques are aiming at protecting the fiber from environmental contact as long as possible. The purpose of this research is to test silicon carbide fiber/silicon carbide matrix (SiC/SiC) ceramic matrix composite at 1300˚C in steam and air to see if it could be a possible candidate for internal engine components.

3

II. Background

2.1 Ceramic Materials

Ceramics are typically classified into two categories: traditional ceramics and engineering/advanced ceramics [19]. Examples of traditional ceramics include brick and tile and are generally only useful in construction, where compressive stresses dominate the loading of the material. Unfortunately in engineering, there cannot just be compressive stresses. This is where advanced ceramics become useful. Some examples of advanced ceramics are aluminum oxide (alumina), silicon carbide (SiC), and silicon nitride. Generally these ceramics are processed and created in a manner to be able to hold tensile stresses at very high temperatures, which make them useful in many engineering applications like engines. These properties are controlled by the electronic structure of the atomic bonds. The lack of conduction electrons in these ceramics make them excellent insulators and give these materials excellent thermal stability. The strength of these atomic bonds also make the materials high strength and provide protection against hostile environments. Unfortunately, this bond strength also causes ceramic materials to have very little ductility as well as low fracture toughness. These materials tend to be very hard and brittle and are prone to sudden catastrophic failure.

One of the biggest drawbacks to ceramics as a useful material is their low damage tolerance. Small defects on the surface can provide an excellent initiation point for almost instantaneous catastrophic failure of the material. This gives ceramics a low fracture toughness and limits their use in many engineering environments. It is desirable for a material to have a minimal amount of damage tolerance so that inspection cycles can detect possible failures before they become catastrophic. Table 1 below shows various fracture toughness values for multiple

4

engineering materials. Current metal alloy systems have fracture toughness values that are 10-20

times those of current ceramics.

Table 1. Fracture toughness values of various engineering materials [5].

Material	K_{IC}, MPa m$^{1/2}$
Polymers	
Polyethylene	1-2
Nylon	3
Epoxy	0.5
Metals	
Pure metals	100-300
Aluminum Alloys	20-50
Titanium Alloys	50-110
Low Carbon Steels	50
Cast Iron	40,278
Ceramics	
Sodalime Glass	0.5-1
Magnesium Oxide	3
Alumina	1-3
Silicon Oxide	2-4
Silicon Nitride	3-5

The idea of fracture toughness is important when considering applications for ceramics as

engine components. Many of the components in engines undergo continuous cyclic loading

which causes fatigue fracturing. Nearly 36% of all jet engine failures can be attributed to cyclic

fatigue of engine components [8]. Fatigue loading feeds crack initiation and propagation causing

an eventual failure of the material. For this reason research began to focus on ways of improving

the damage tolerance and fracture toughness of ceramic systems. The primary focus currently is

generating composite systems with these ceramics.

2.2 Composites

Composites are material systems that have been expanding in popularity in the aircraft industry due to their high strength to weight ratios. A composite is defined as a material system consisting of two or more phases on a macroscopic scale, whose properties and/or performance are designed to be superior to those of the constituent materials separately [9]. Composites are comprised of a matrix and a dispersed phase. The dispersed phase is most often the reinforcement fibers. The matrix acts as a bonding agent to provide structure and organization to the reinforcing material. In general the reinforcing material comprises the majority of the material systems strength. These material systems are classified by the chemical structure of their matrix phases.

Matrix phases that are made from resins or epoxy like cured agents are classified as polymer matrix composites (PMC). These systems are well known for high strength to weight ratios but low thermal stability. Another type of composite is the metal matrix composite (MMC). Currently part of the F-16 landing gear is comprised of a SiC/Titanium MMC which has provided a significant weight reduction without the loss of mechanical properties [4]. The last category is ceramic matrix composites (CMC). These systems are well known for their high temperature stability and can be either carbide or oxide systems.

The choice of which system and reinforcing materials to mix and use depends on the application of the material system. A desire for better strength, thermal stability, fracture toughness, or damage tolerance will drive the decision for a particular composite system. This research is focused on a CMC that has better fracture toughness and was specifically designed to provide a CMC that has improved damage tolerance even at elevated temperatures.

6

2.3 Ceramic Matrix Composites

2.3.1 General Information

Ceramic matrix composites are a class of composites that were first designed in order to take advantage of the benefits of strongly bonded atoms with little to no electronic movement. The stability of the bonds provides protection from hostile environments as well as stability at elevated temperatures. One of their biggest draw backs was lack of damage tolerance, catastrophic failure occurred too quickly. By creating a composite of a material with a silicon carbide matrix and silicon carbide fibers, the damage tolerance of the material is increased substantially [6]. The composite of a ceramic matrix with ceramic fibers allows CMCs to maintain high strength even at elevated temperatures as shown in Figure 2 below.
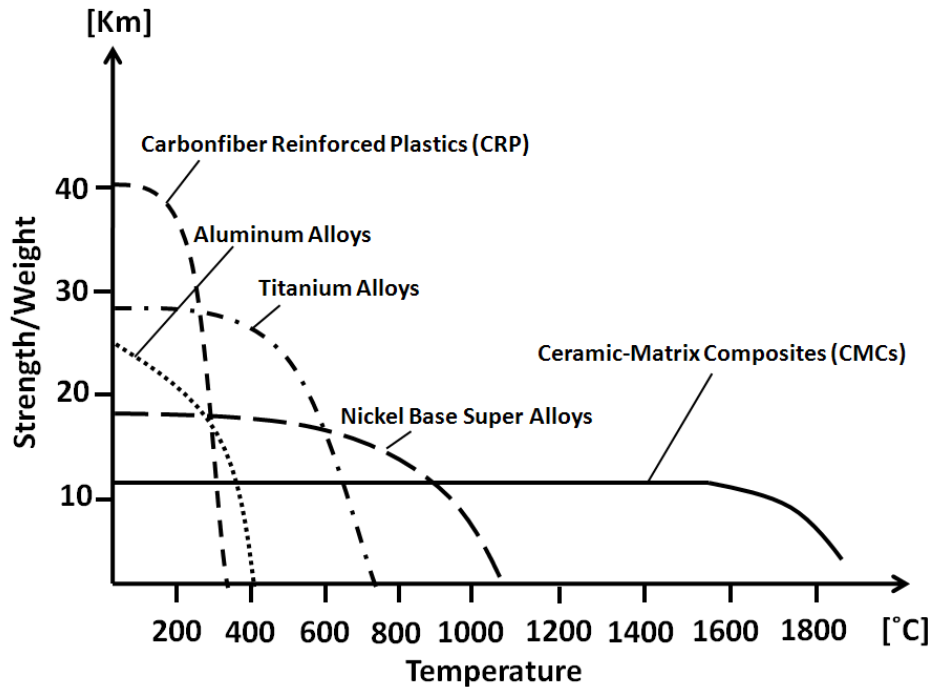
Figure 2. Mechanical performance of materials versus temperature [18].

Generally with PMCs and MMCs, the fiber reinforcements are much stronger than the matrix. This allows the material to be much stronger than just the matrix normally would.

7

However, this is not the design philosophy for ceramic matrix composites. For PMCs and MMCs, the reinforcement is designed to provide additional strength for the material system. For CMCs the reinforcement of a matrix with a fiber of the same material has two design purposes. Ceramic materials are generally high strength materials without reinforcement. First, instead of strength enhancement, these fibers are designed to provide increased damage tolerance. Cracks that are initiated in the ceramic matrix can only propagate until they contact the interface of the matrix with a fiber. This slows cracking and allows for more graceful failure. Second, since the matrix and fiber are the same material they will have the same thermal expansion coefficients. This prevents internal stresses from damaging the composite from the inside during highly elevated temperature applications [5]. Essentially increasing the toughness of CMCs can be simplified down to impeding crack initiation and/or propagation. Generally this is done in CMCs by generating a porous matrix and having a weak matrix-fiber bond so that the crack cannot propagate straight through the fiber without significant disruption.

2.3.2 Types of Ceramic Matrix Composites

There are two different categories of CMCs which are based on the chemical composition of the ceramic. These two types are known as oxide and non-oxide ceramics. The oxide ceramics typically used in CMCs are alumina and silica, Al_2O_3 and SiO_2 respectively [5]. The oxide ceramics are known for having high moduli and strength. Also due to their chemical composition, these materials are resistant to oxidation even at extremely high temperatures. Unfortunately, fibers made from oxide ceramics are known to have higher creep rates than non-oxide ceramics [5]. Non-oxide ceramics include carbides and nitrides, such as SiC and Si_3N_4. These ceramics generally are stronger and less prone to creep than their oxide counter parts. Unfortunately, the lack of oxygen in their chemical composition increases the susceptibility of

8

non-oxide ceramics to oxidation, especially at very high temperatures. This oxidation degrades the material and reduces its strength, eventually causing material failure. Highly oxidative environments like water vapor have also been shown to increase the rate of oxidation of SiC systems at elevated temperatures [17]. There is a great amount of effort going towards producing carbide systems with reduced oxidation potential.

Currently there is a focus on increasing CMCs resistance to cracking, which is the primary mode of failure under fatigue loading. There are two ways for improving fracture toughness. One of these ways is decreasing the bond strength between the matrix and the fiber. This is accomplished by coating the fibers with carbon or boron nitride. This allows for crack deflection and sliding of fibers which absorbs energy and slows crack growth in the material. Figure 3 below shows a schematic depiction of a strong versus weak fiber-matrix interface. These weak interfaces allow for crack deflection around fibers inhibiting sudden failure. Without the weak interphase a small crack would cause a sudden catastrophic failure by cutting through fibers.
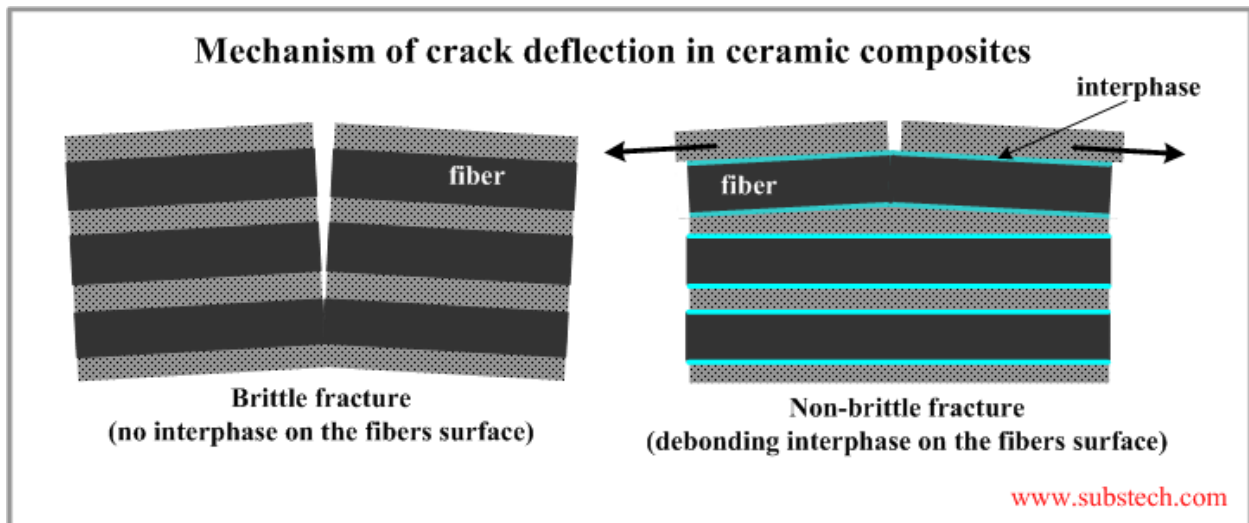
Figure 3. Crack deflection from interphase bind strength [12]

9

The other method for improving fracture toughness of ceramics is to control the matrix porosity. It has been shown that controlling the porosity of the matrix successfully deflect cracks in oxide/oxide ceramics [21]. Unfortunately, this porosity also provides a route for hostile environments, like moisture or gases, to penetrate the matrix and reach the fibers even without cracks.

Currently one of the biggest drawbacks for SiC/SiC systems is that the fibers are extremely susceptible to oxidative attack. There would be a large benefit for any material that was capable of maintaining its strength in hostile environments at high temperatures. The purpose of this research is to analyze a SiC/SiC composite at elevated temperatures in air and steam to determine its mechanical limits.

2.3.3 Previous Research on SiC/SiC Ceramic Matrix Composites

Research on SiC/SiC CMCs was previously performed at AFIT [7,10]. The composite tested by Christensen consisted of a SiC matrix reinforced with a boron nitride (BN) coated Hi-Nicalon^{TM} fibers woven in an eight harness satin weave. This SiC matrix was densified using the chemical vapor infiltration process. Tensile test and tension-tension fatigue test were conducted at 1200°C. The fatigue tests were conducted in laboratory air and steam at 1200°C at frequencies of 0.1 Hz, 1.0 Hz, and 10 Hz with a max stress ranging from 80 to 120 MPa in air and from 60 to 110 MPa in steam. The fatigue limit was 100 MPa (46% UTS) in air and 80 MPa (37% UTS) in steam. With run-out defined as 2 x 10^5 cycles at 1.0 Hz and 10 Hz test and as 10^5 cycles for 0.1 Hz. All specimens tested in air retained 100% of their tensile strength and only one specimen in steam showed minor strength degradation as seen in Figure 4. The change in slope of the stress strain curve corresponds to cracking of the matrix in the composite. At this point the load is transferred to the fibers.

10
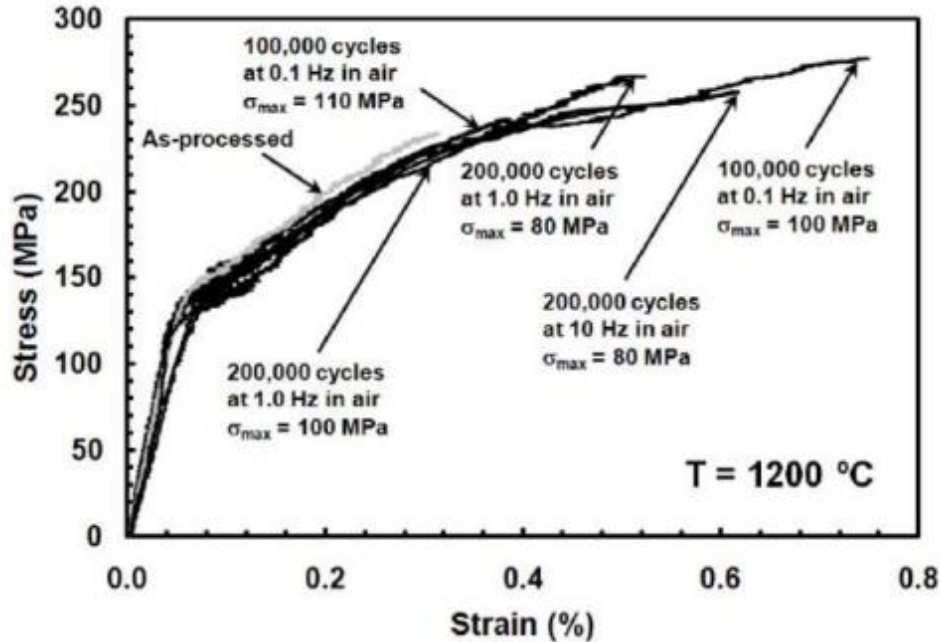
Figure 4. Stress-strain response of Hi-Nicalon/BN/SiC specimens fatigue in air at 1200˚C then subjected to a monotonic tensile test to failure in laboratory air at 1200˚C at displacement rate of 0.05 mm/s [7].

Jacob Delapasse studied a Hi-Nicalon/SiC-B$_4$C composite system [10]. Delapasse completed tension-tension fatigue tests at 1200 ˚C in laboratory air and in steam at frequencies of 0.1 Hz, 1.0 Hz, and 10 Hz with a max stress ranging from 100 to 140 MPa. The fatigue limit at 1.0 Hz was 116 MPa (38% UTS) in air. Fatigue run-out was defined as 2 x 10^5 cycles at 1.0 Hz and 10 Hz test and as 10^5 cycles at 0.1 Hz. The composite studied by Delapasse produced larger strains than the baseline CMC analyzed by Christensen, see Figure 5 and 6. The presence of steam had little influence on the fatigue life at 1.0 Hz but noticeably degraded fatigue lifetimes at 0.1Hz for stress greater than or equal to 120 MPa. Delapasse also reported strain ratcheting along with strain accumulation up to 2%.

11
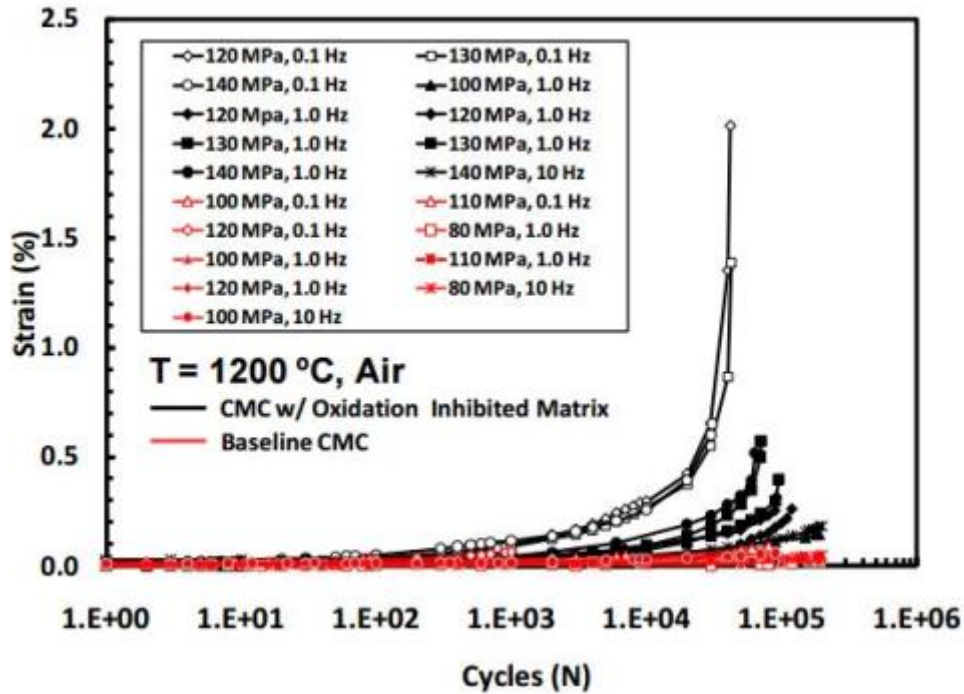
Figure 5. Accumulated strain vs. fatigue cycles for the Hi-Nicalon/SiC-B$_4$C and HiNicalon/BN/SiC ceramic composites at 1200°C in laboratory air. Data for Hi-Nicalon/BN/SiC from Christensen. Graph from Delapasse [10]
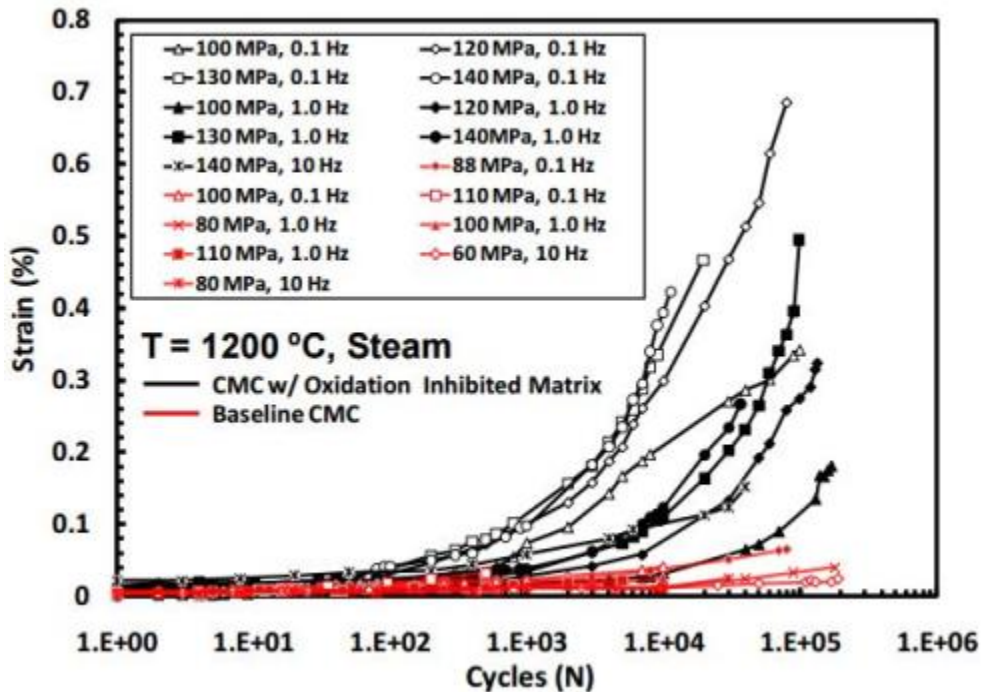
Figure 6. Accumulated strain vs. fatigue cycles for the Hi-Nicalon/SiC-B$_4$C and HiNicalon/BN/SiC ceramic composites at 1200°C in steam. Data for Hi-Nicalon/BN/SiC from Christensen. Graph from Delapasse[10].

12

Specimens that achieved fatigue run-out in air and in steam retained 42% and 59% of their tensile strength respectively. Delapasse showed that there was a noticeable strain increase and loss of strength after extended exposure to fatigue at elevated temperatures. He attributed the strain and eventual failure to creep of the reinforcing fibers. The Hi-Nicalon/SiC-B_4C composite system had a self-healing matrix to protect the fibers against oxidative damage. A study of the fatigue behavior of Hi-Nicalon/SiC-B_4C at 1300°C is desired to assess how significant temperature increases will affect the fatigue performance of this composite system.

III. Material and Test Specimen

3.1 Material Specifications

The material used for this investigation is the same material used by Delapasse in his research. The composite was manufactured by Hyper-Therm High-Temperature Composites, Inc., Huntington Beach CA. The composite was processed via chemical vapor infiltration (CVI) of HyprSiC oxidation inhibited matrix material into the woven Hi-Nicalon fiber preforms. The composite consisted of eight plies of Hi-Nicalon [0°/90°] fibers woven in a plain weave, shown in Figure 7. To produce the laminated preforms, the 9 [0°/90°] plies were laid-up symmetric about mid-plane with warp and fill plies alternated. Prior to infiltration with the matrix, the preforms were coated with pyrolytic carbon and with boron carbide overlay in order to decrease interface bonding between fibers and matrix. The thickness of the pyrolytic carbon fiber coating was approximately 0.40 μm and the thickness of the boron carbide overlay was approximately 1.0 μm. The HyprSiC oxidation inhibited matrix was densified by CVI. The tensile specimens had an outer seal coating of HyprSiC that was applied by chemical vapor deposition (CVD) after the specimens had been machined. The material specifications as reported by Hyper-Therm HTC Inc. are provided in table 2 below.

13

Table 2. Material specifications as reported by Hyper-Therm HTC Inc.

Material	Geometry	Planform Size (in)	Thickness (in)	Density (g/cm^3)	Fiber Volume (%)
Hi-Nicalon/PyC/HyperSiC	Both	7.75 x 7.75	0.11	2.50	34.1
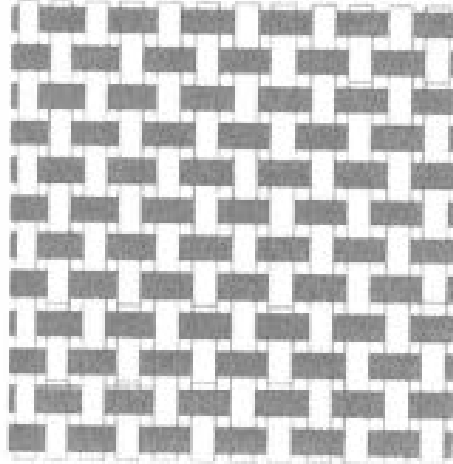
Figure 7. Plain weave [9].

The oxidation inhibited matrix of the CMC studied in this work consists of alternating layers of silicon carbide (SiC) and boron carbide (B_4C). When the composite is exposed to an oxidizing environment, oxygen diffuses through the network of matrix cracks and reacts with B_4C layers of the multilayered self-healing matrix to produce fluid oxide phases that can fill cracks as soon as they are formed. This oxygen is trapped in the oxide phases and is prevented from attacking the oxidation prone load-bearing fibers. The SEM micrographs showing typical microstructure of the Hi-Nicalon/SiC-B_4C composite are presented in Fig 8. Note the oxidation inhibited matrix consisting of alternating layers of SiC and B_4C and the Hi-Nicalon fibers with PyC fiber coating and B_4C overlay.

Pore
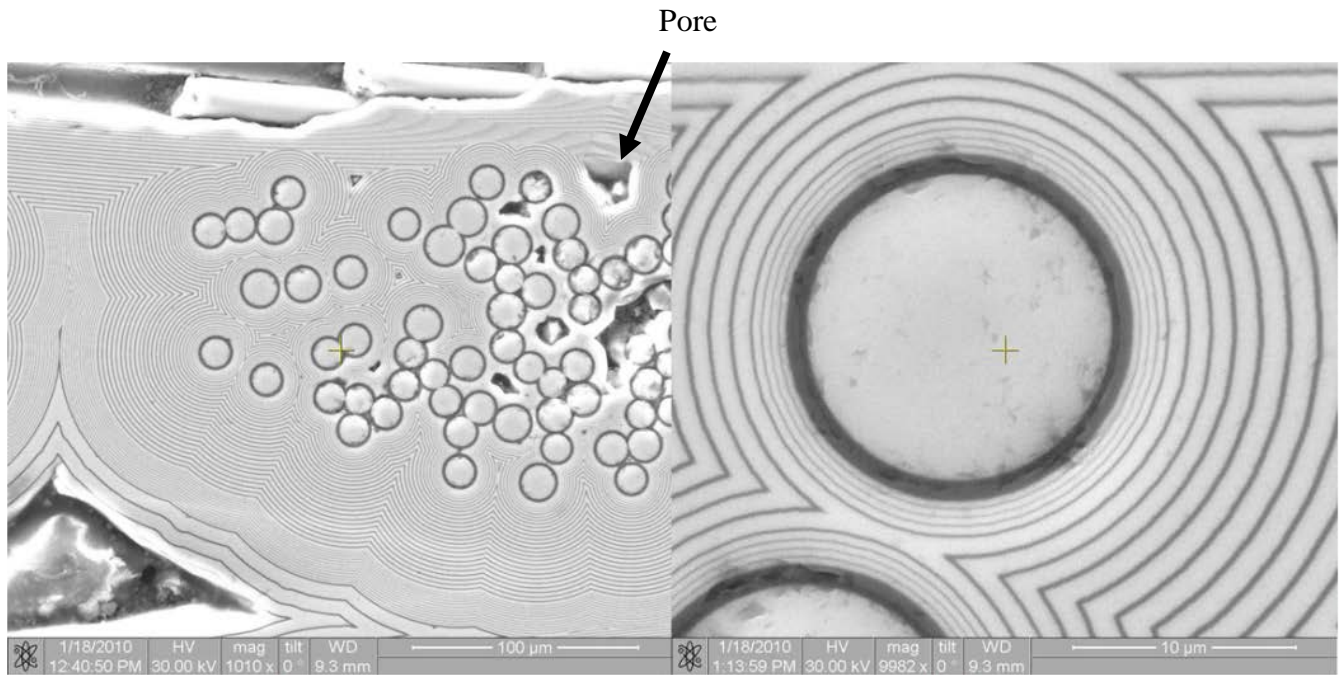
Figure 8. Hi-Nicalon/SiC-B₄C oxidation inhibitor matrix reproduced from [10].

The SiC-B$_4$C matrix was densified by chemical vapor infiltration (CVI). CVI is similar to chemical vapor deposition (CVD), which is often used to create films or surfaces on materials. The main difference between CVI and CVD is that CVD is used to create a surface on some bulk exposed material like a silicon wafer. CVI is a similar process but instead of flowing the composition gases across the surface of a bulk material, the gas is directed through a fiber preform. To start the process, a preform array of fibers is placed into a high temperature furnace. Reactant gases are then pumped into the chamber and flow around and react forming a surface on the fibers. As the flow of reactant gases continues the fiber diameter increases until the volume of the fiber preform is filled with the ceramic matrix of the CMC. One of the main drawbacks of CVI is unintended creation of pores in the matrix. These porous areas are seen in Figure 8 above. These pores can be initiation points for cracking within the ceramic matrix [10].

The CMC studied in this work is reinforced with SiC Hi-Nicalon fibers, which are known to have good tensile strength and elastic modulus and is capable of maintaining these properties

15

at high temperatures [3]. Commercially produced Hi-Nicalon fibers consists of a mixture of β-SiC, free carbon, and SiO_2. The designation "Hi" indicates low oxygen content. The fiber coating of pyrolytic carbon is intended to provide a weak fiber-matrix interface to guarantee sufficient debonding of the fibers in the matrix. This weak interface provides a higher fracture toughness and strength. The coating of boron carbide, which has low density, high melting point, and high hardness, is intended to protect the fiber from oxidative environments. At elevated temperatures and in oxidative atmospheres, boron carbide is oxidized to boron oxide which acts as a self-healing layer to protect the fibers. A higher magnification view of fibers and fiber coatings is shown in Figure 9 below.
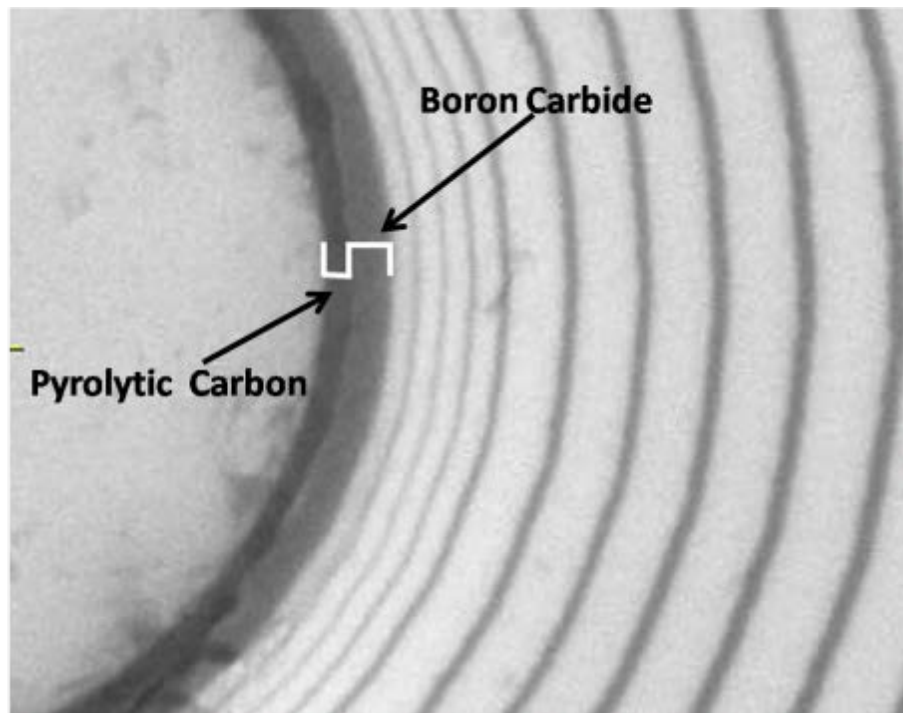
Figure 9. Coated Hi-Nicalon fiber, pyrolytic carbon (0.4 µm) and boron carbide (1.0µm) [10].

3.2 Test Specimen

All test specimens were machined to the specifications in Figure 10. The 0° fibers were oriented along the axis of the test specimens. All specimens were cut into the traditional dog bone shape produce uniform tensile stress in the gage section. Due to the non-uniformity caused by the fiber weave, all specimen widths and thicknesses were measured three times using a Mitutoyo Corporation Digital Micrometer and an average value was recorded for each. Dimensions of all the test specimens are shown in table 3.
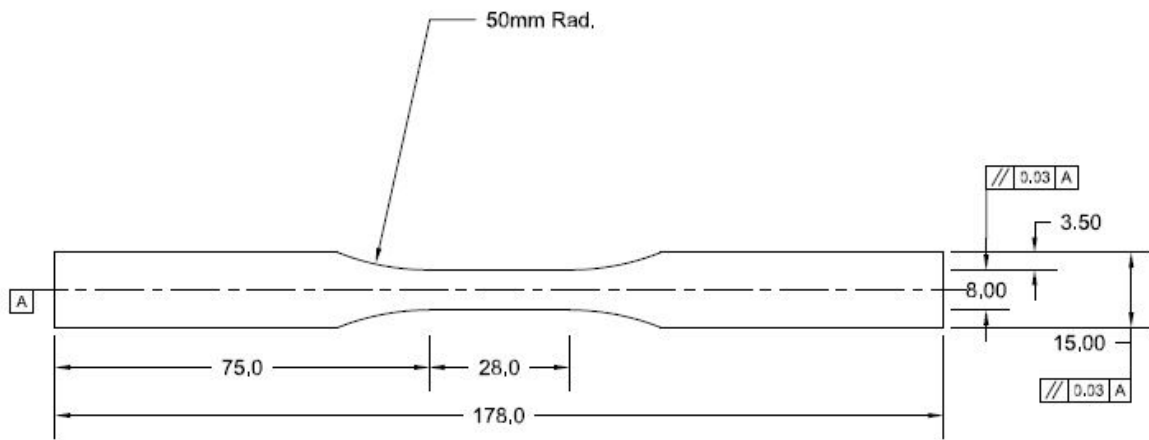
Figure 10. Dogbone shaped test specimen. All dimensions in mm.

Table 3. Dimensions of dogbone shaped test specimens

I.D. Number	Width (mm)	Thickness (mm)	Area (mm^2)
L94	8.04	2.34	18.79
L97	8.03	2.60	20.88
L98	8.06	2.64	21.30
L99	8.02	2.57	20.62
M03	8.08	2.66	21.48
M04	8.05	2.56	20.64
M07	8.02	2.47	19.81
M08	8.05	2.50	20.13
M11	8.07	2.48	20.01
M12	8.07	2.42	19.56
M16	8.03	2.60	20.89
M18	8.07	2.48	19.98
L93	8.06	2.45	19.74

To prevent damage or crushing of the specimen by the grips, fiber glass tabs were attached to the top and bottom gripping sections of the test specimen using M-Bond 200. Each tab was then marked with a U or L, specifying whether it was the upper or lower section in the test manifold. A specimen prepared for testing is shown in Figure 11.
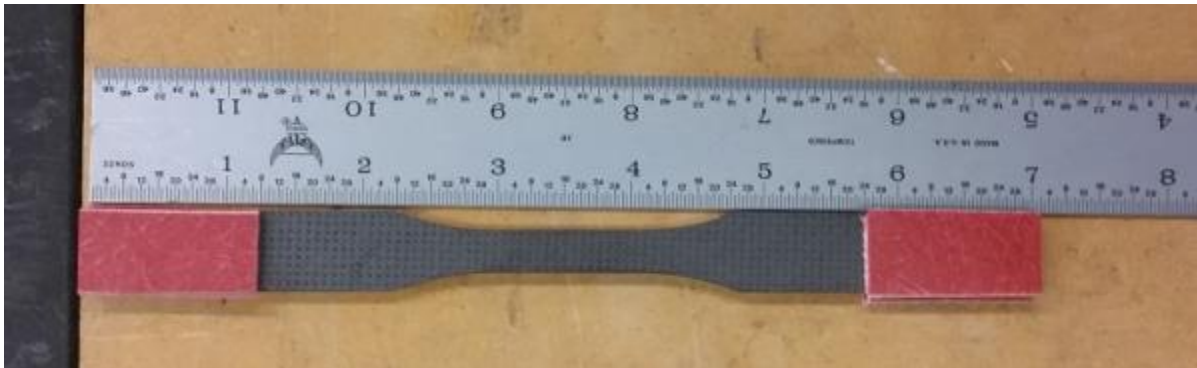
Figure 11. Example dogbone test specimen with tabs.

An additional 10 specimens of the same CMC were also tested. These specimens had an hourglass shape shown in Figure 12. Dimensions of the hourglass-shaped specimens are summarized in Table 4.
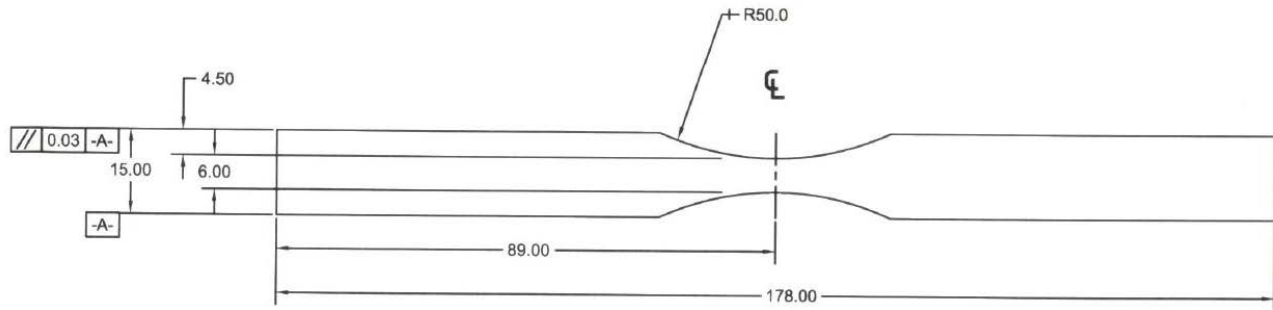
Figure 12. Hourglass-shaped test specimens. All dimensions in mm.

Table 4. Dimensions of hourglass-shaped test specimens

I.D. Number	Width (mm)	Thickness (mm)	Area (mm^2)
M38	6.10	2.42	14.76
M39	6.06	2.65	16.06
M40	6.06	2.52	15.27
M41	6.09	2.51	15.29
M42	6.08	2.36	14.35
M43	6.08	2.60	15.81
M44	6.07	2.64	16.02
M45	6.09	2.52	15.35
M46	6.14	2.55	15.66
M47	6.07	2.64	16.02

19

IV. Experimental Setup and Procedure

4.1 Test Equipment

A 5 kip hydraulic MTS mechanical testing machine was used for all tests. The MTS testing machine was equipped with water cooled collet grips and a two zone resistance heating furnace with a temperature control system for each zone. The machine is shown in Figure 13. Prior to all tests the system was warmed up using a 0.1 in. amplitude sine wave under displacement control for approximately 20 min.

Figure 13. 5 Kip MTS machine.

For all tests, the test specimen was mounted into the MTS Series 647 hydraulic wedge grips with precautions to ensure that the specimen was parallel to the loading direction. The collet grip surfaces were coated with a Surfalloy grip texture to prevent slipping. The wedge grip pressure was set to 10 MPa to prevent slippage while also not crushing the test specimen. The grips were cleaned with a wire brush after each test to insure proper function and remove any build-up of the fiberglass dust from the specimen tabs. The grips were cooled using 15 ˚C water from the Naslab model HX-75 chiller. An alumina susceptor (Fig. 14) was used in tests to ensure a uniform temperature environment in air and in steam around the specimen gage section and to protect the furnace elements from the steam. An AMTECO steam generator and deionized water were used to generate steam which entered the susceptor through a feeding tube to create a near 100% steam environment.

Figure 14. Test Specimen with alumina susceptor.

Strains were measured using a high temperature uniaxial extensometer, MTS Model 632.53 E-14. The test set up is shown in Figure 15.
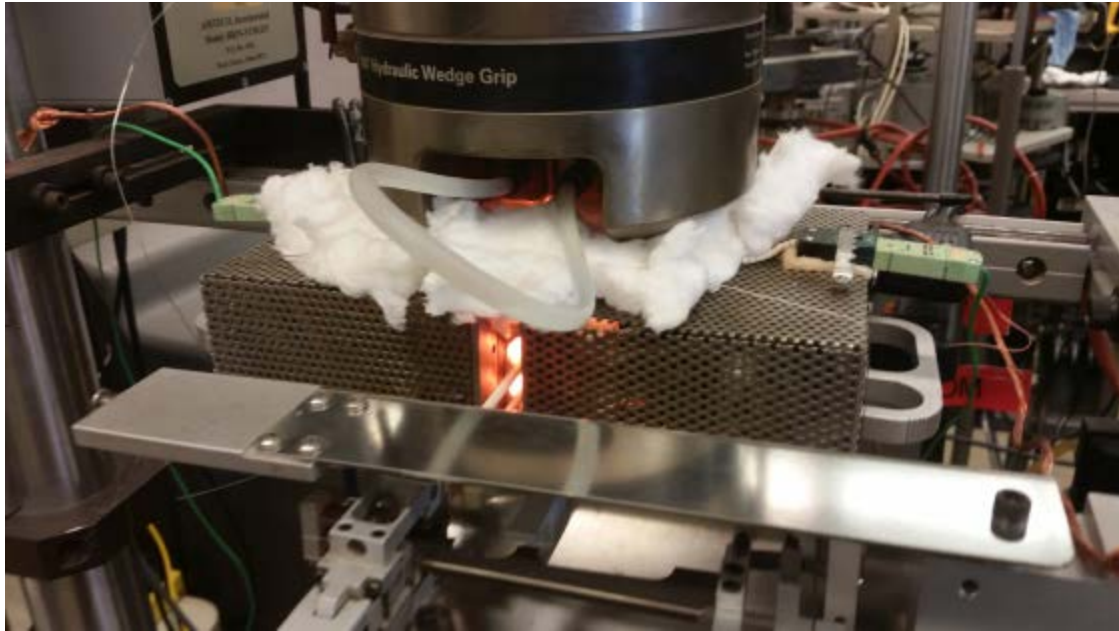
Figure 15. Test specimen mounted with extensometer testing.

Prior to testing, specimens were enclosed by an AMTECO Hot Rail two zone furnace. The furnace temperature was controlled by two MTS Model 409.83B Temperature Controllers. The controllers managed two separate furnace zones dubbed the left and right zones. To ensure the furnace could produce the desired test temperature, thermal insulation was used to cover the top and bottom of the furnace to reduce heat loss.

4.2 Temperature Calibration

To ensure that the specimen is tested at the desired temperature, a temperature calibration was completed. In order to achieve a temperature of 1300˚C, the furnace output power was increased to 75% and the temperature control max setting parameters were increased from 1400˚C to 1450˚C.

The temperature calibration was completed by attaching two R-type thermocouples to the test specimen. The test specimen was then enclosed in an alumina susceptor and placed in the chamber. The calibration specimen is shown in Figure 16.
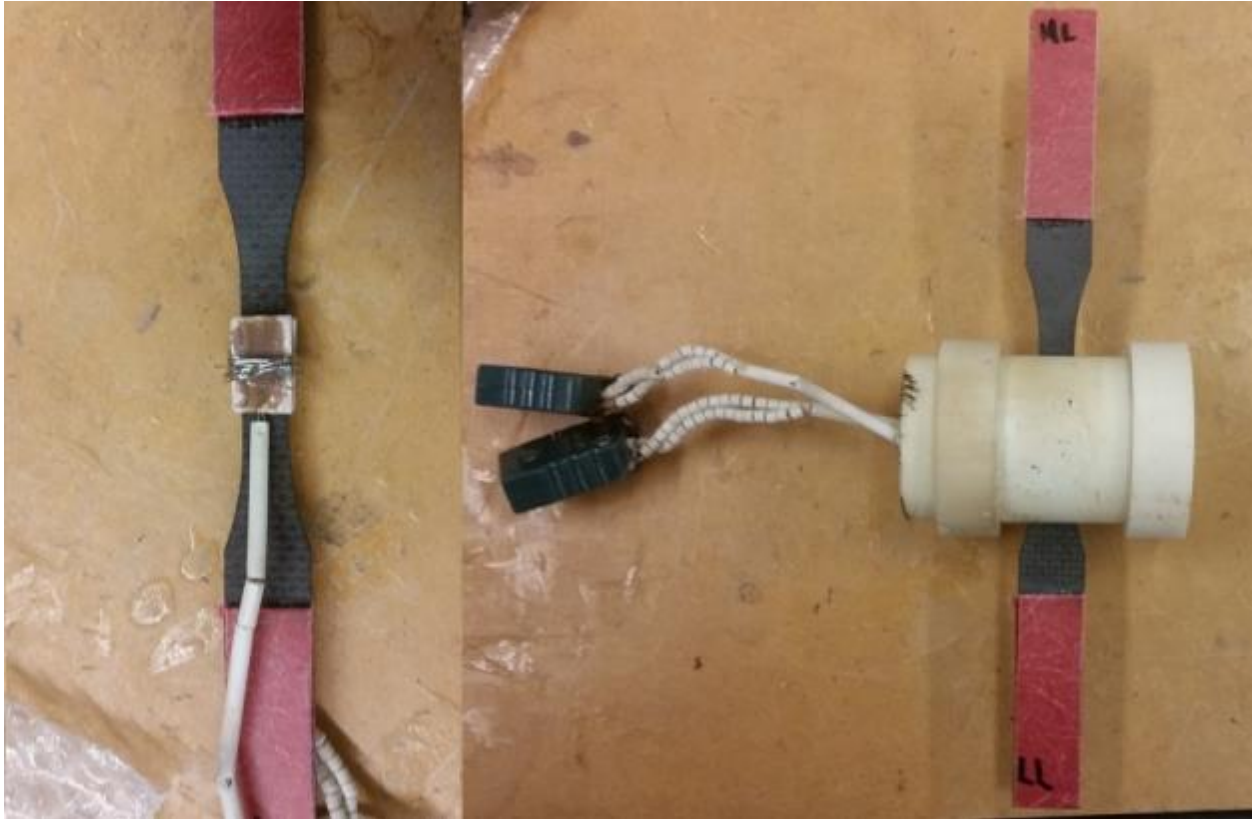
Figure 16. Temperature calibration specimen without (left) and with (right) susceptor.

The specimen was held at zero load under load control during heating to allow for material expansion during the temperature rise. The temperature on the sides of the specimen were measured using an Omega HH501BR digital thermometer attached to both R-type thermocouples. The temperature controller settings were increased until the temperature of the specimen reached 1300˚C. The settings were recorded and used during testing. The same process was completed in steam environment.

4.3 Microstructural Characterization

After testing the specimen fracture surfaces were examined using a Zeiss Stemi SV II optical microscope equipped with a Zeiss AxioCam HRc digital camera and the Quanta 200 scanning electron microscope (SEM). Optical micrographs were taken of all of the dog bone specimens and some representative micrographs were taken of the hour glass specimens. After the optical micrographs were completed the lower section of each specimen was examined in the SEM. The specimens were cut with a diamond coated saw 4-6 mm below the edge of the fracture surface. The samples were then mounted onto metallic SEM sample platforms with double sided carbon tape.

4.4 Experimental Procedure

4.4.1 Monotonic Testing

A specimen was tested under monotonic tensile loading to provide baseline tensile properties of Hi-Nicalon/SiC-B$_4$C at 1300°C. With the MTS at a zero load condition, the temperature was raised to 1300˚C at a rate of 1.0 °C/s. Once the specimens reached 1300˚C, the temperature was held constant for 20 minutes. Then, the specimen was loaded in the displacement control at the rate of 0.05 mm/s until failure. During testing, strain, load, left and right oven temperature, displacement, displacement control, and time were all recorded.

4.4.2 Fatigue Testing

All specimens were tested in tension-tension fatigue at 1 Hz with a maximum to minimum stress ratio (R) of 0.05 in air and steam. With the MTS 5 kip machine set in force control, temperature was raised to 1300˚C at a rate of 1.0 °C/s. Once the specimens reached 1300˚C, the system was allowed to dwell for 20 minutes to ensure a steady temperature

environment. After the dwell period, specimens were loaded to the minimum stress level in 20 seconds, then subjected to cyclic loading. The fatigue run-out was set to 2×10^5 cycles. If a specimen achieved run-out, it was unloaded to zero load, then subjected to tensile test in order to measure the retained properties. The data collected included strain, load, load command, displacement, cycle number, temperature and time. The data was collected in four different data files titled "Specimen," "Cycle," "Peak and Valley," and "Tensile." The "Specimen" file collected data during the warm up, dwell period, and ramp to minimum stress. The "Cycle" file collected full stress-strain data during the following cycles: i) cycles 1 to 10, ii) every tenth cycle between cycles 20 and 100, iii) every 100th cycle between cycles 100 and 1000, iv) every 1000th cycle between cycles 1000 and 10000, and v) every 10000th cycle between cycles 10000 and run-out. The "Peak and Valley" file collected peak and valley data for each cycle. The "Tensile" file collected data during the post-fatigue tensile test if the specimen achieved fatigue run-out. A screen shot of the program used to input the test procedures is in Figure 17.

Note that strain data were collected for the dogbone-shaped specimens only. Strain data were not collected for the hourglass-shaped specimens. Without a flat gage-section on the specimen, the uniaxial low-contact force extensometer cannot be used.
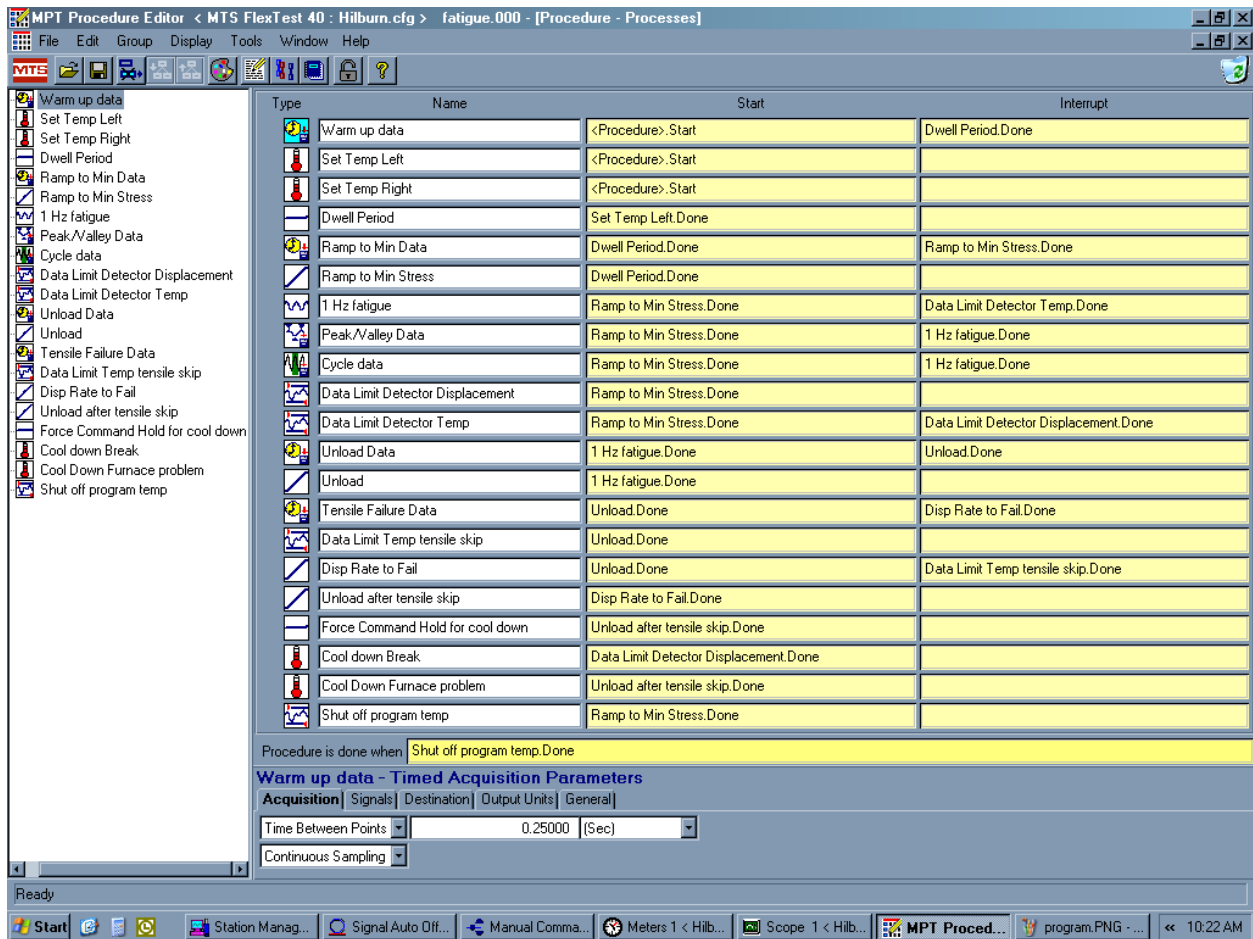
Figure 17. Screen shot of the program used for all testing.

V. Results and Discussion

5.1 Chapter Overview

This chapter presents the results of all tests conducted for this research. Section 5.2 summarizes the thermal expansion data taking during warm up to test temperature. Section 5.3 presents the results of the tensile tests. Section 5.4 presents the data collected during the tension-tension fatigue test performed in air and in steam. Fatigue run-out was defined as $2x10^5$ cycles. The tests performed in this work are summarized in Table 5.

26

Table 5. Summary of Hi-Nicalon/SiC-B$_4$C ceramic composite test results obtained at 1300°C

Specimen	Environment	Maximum Stress (MPa)	Elastic Modulus (GPa)	Cycles (N)	Time (h)	Failure Strain (%)
Tensile Test						
L94	Tension	341	179.5	-	-	0.57
L97	Tension	322	-	-	-	-
Tension-Tension Fatigue Test- (Dogbone-shaped specimens)						
L99	Air	140	160.8	20069	5.6	2.62
M18	Air	130	181.4	38828	10.8	1.13
M03	Air	120	183.5	55199	15.3	1.26
M04	Air	100	261.3	84855	23.6	0.34
M07	Air	70	244.9	200000[a]	55.6	0.50
M16	Steam	160	142.9	17811	4.9	0.55
M11	Steam	140	209.6	72074	20.0	1.07
M08	Steam	120	227.1	93016	25.8	1.07
M12	Steam	100	242.8	200000[a]	55.6	0.13
Tension-Tension Fatigue Test- (Hourglass-shaped specimens)						
M41	Air	145	-	54385	15.1	-
M42	Air	145	-	68831	19.1	-
M43	Air	114	-	115435	32.1	-
M45	Air	100	-	170033	47.2	-
M46	Air	80	-	200000[a]	55.6	-
M38	Steam	150	-	13266	3.7	-
M39	Steam	130	-	45670	12.7	-
M40	Steam	120	-	134071	37.2	-
M47	Steam	100	-	200000[a]	55.6	-

a. Run-out. Failure of specimen did not occur when the test was terminated.

5.2 Thermal Expansion

For each test, the temperature was increased at a rate of 1°C/s to the test temperature and allowed to dwell for 20 minutes under zero load to ensure a steady state thermal environment prior to testing. During this time, strain data were collected in order to determine the coefficient of thermal expansion. The coefficient of thermal expansion, α, was determined as:

$$\alpha = \frac{\varepsilon}{\Delta T} \qquad (1)$$

Where ε is the thermal strain and ΔT is the temperature change from 23°C to 1300°C. All thermal strain data are summarized in Table 6. The recorded thermal strain varied between 0.56% and 0.70% with an average of 0.61%. The average thermal expansion coefficient was 4.74×10^{-6} 1/°C with a standard deviation of 0.37×10^{-6} 1/°C. This value is similar to those reported previously by Delapasse [10] and reproduced in Table 6.

Table 6. Thermal strain and coeffiecient of linear thermal expansion for Hi-Nicalon/SiC-B₄C CMC.

Specimen	Thermal Strain (%)	Coefficient of Linear Thermal Expansion $(10^{-6}/°C)$
L99	0.59	4.61
M03	0.57	4.46
M04	0.57	4.42
M07	0.57	4.48
M08	0.63	4.93
M12	0.59	4.63
M16	0.56	4.39
M18	0.67	5.25
L93	0.60	4.70
L94	0.70	5.48
Average	0.60	4.74
Std. Dev.	0.05	0.37

Panal	Average Thermal Strain (%)	Average Coefficient of Linear Thermal Expansion $(10^{-6}/°C)$
Panal 5[a]	0.57	4.85
Panal 6[a]	0.56	4.72
Panal 7[a]	0.58	4.90
Average	0.57	4.82

a. Data from Delapasse [10]

28

5.3 Monotonic Tension

Tension tests to failure were performed in displacement control at 0.05 mm/s. The results of the tensile tests are summarized in Table 7. The ultimate tensile stress (UTS) reported by AFRL for this material and temperature was 298 MPa [15]. This value of the UTS was combined with the initial tensile test of L97 in this work to calculate the average UTS of 311 MPa. The proportional limit was determined to be 117 MPa (~38% UTS). Figure 18 shows the method used to determine the proportional limit. Tensile stress-strain curve obtained for Hi-Nicalon/SiC-B_4C ceramic composite at 1300°C in air is also shown in Figure 18. An example of how this was calculated is shown in Figure 18. No stain measurements were taken for L97 due to an equipment malfunction.

A representative stress-strain curve obtained at 1300°C in this work is compared to that obtained at 1200°C by Delapasse [10] in Figure 19. A comparison of the tensile properties obtained at 1200°C and 1300°C is presented in Table 7.

Table 7. Tensile properties for Hi-Nicalon/SiC-B_4C CMC at 1300°C and 1200°C. Delapasse[10].

Specimen	Temperature	Elastic Modulus (GPa)	Proportional Limit (MPa)	Stress (MPa)	Strain (%)
L94	1300	179.5	117	341	0.57
L97[a]	1300	-	-	322	-
Delapasse	1200	206.3	116.3	306.8	0.686

a. No strain measurements taken
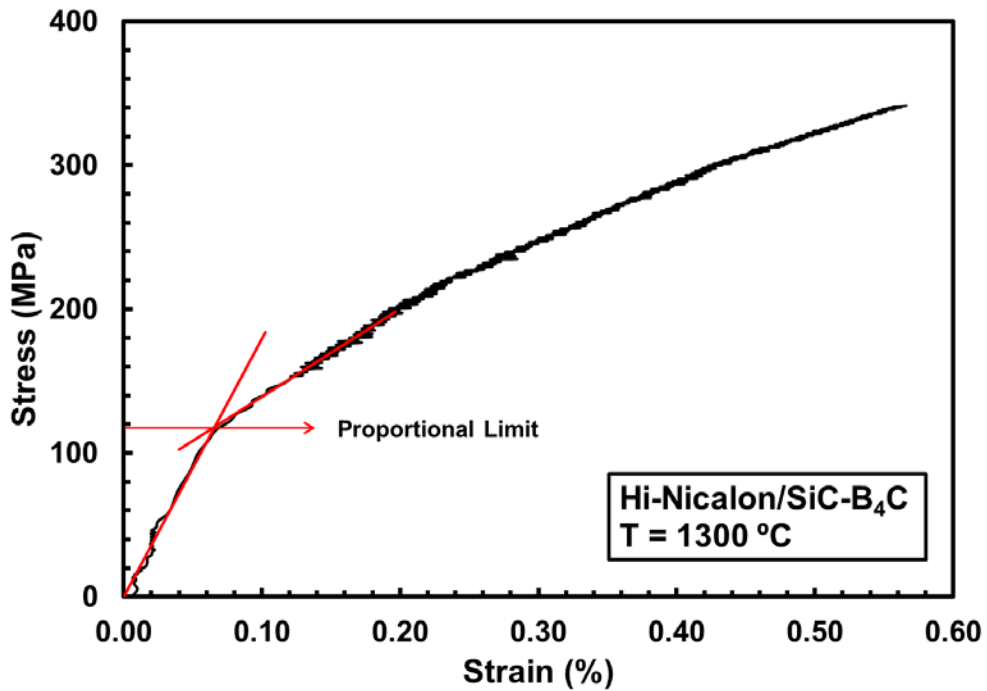
Figure 18. Tensile stress-strain curve obtained for Hi-Nicalon/SiC-B₄C CMC at 1300°C in air.
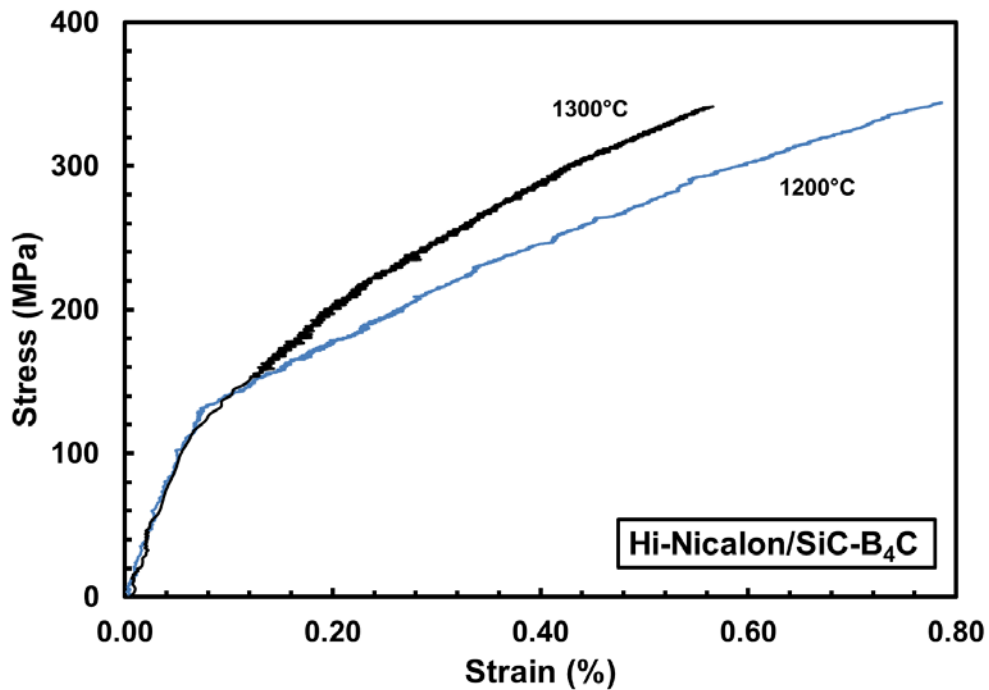
Figure 19. Tensile stress-strain curves obtained for Hi-Nicalon/SiC-B₄C CMC at 1300°C. Data at 1200°C from Delapasse[10].

As seen in Figure 19, the bi-linear nature of the stress-strain curve visible at 1200°C disappears at 1300°C. At 1300°C the knee in the stress-strain curve is no longer present. While the tensile strength does not seem adversely affected by the temperature increase from 1200°C to 1300°C, the material accumulates less strain before failure at the higher temperature. Notably similar elastic moduli and proportional limits were produced at 1200 and 1300°C. One notable feature is that the specimen tested at 1300°C shows stiffer behavior above the proportional limit.

5.4 Tension-Tension Fatigue

Tension-tension fatigue tests were conducted at a frequency of 1.0 Hz at 1300°C in laboratory air for both types of specimen geometry. The maximum stress level ranged from 70 MPa to 160 MPa. Run-out was defined as 2×10^5 cycles. The results obtained for both types of specimen geometry in air and in steam are summarized in Table 8. Results obtained for the dogbone-shaped specimens are also presented in Figure 20 as the maximum stress vs. cycles to failure curves. Recall that strain measurements were not taken for the hourglass-shaped specimens due to the lack of a gage section.

Table 8. Summary of fatigue results for Hi-Nicalon/SiC-B$_4$C ceramic composite at 1300°C in laboratory air and in steam.

Specimen	Test Environment	Maximum Stress (MPa)	Elastic Modulus (GPa)	Cycles to Failure (N)	Time to Failure (h)	Failure Strain (%)
Dogbone-shaped Specimens						
L99	Air	140	160.8	20069	5.6	2.62
M18	Air	130	181.4	38828	10.8	1.13
M03	Air	120	183.5	55199	15.3	1.26
M04	Air	100	261.3	84855	23.6	0.34
M07	Air	70	244.9	200000[a]	55.6	0.50
M16	Steam	160	142.9	17811	4.9	0.55
M11	Steam	140	209.6	72074	20.0	1.07
M08	Steam	120	227.1	93016	25.8	1.07
M12	Steam	100	242.8	200000[a]	55.6	0.13
Hourglass-shaped Specimens						
M41	Air	145	-	54385	15.1	-
M42	Air	145	-	68831	19.1	-
M43	Air	114	-	115435	32.1	-
M45	Air	100	-	170033	47.2	-
M46	Air	80	-	200000[a]	55.6	-
M38	Steam	150	-	13266	3.7	-
M39	Steam	130	-	45670	12.7	-
M40	Steam	120	-	134071	37.2	-
M47	Steam	100	-	200000[a]	55.6	-

a. Run-out defined as 2x10^5 cycles. Failure of specimen did not occur when the test was terminated.
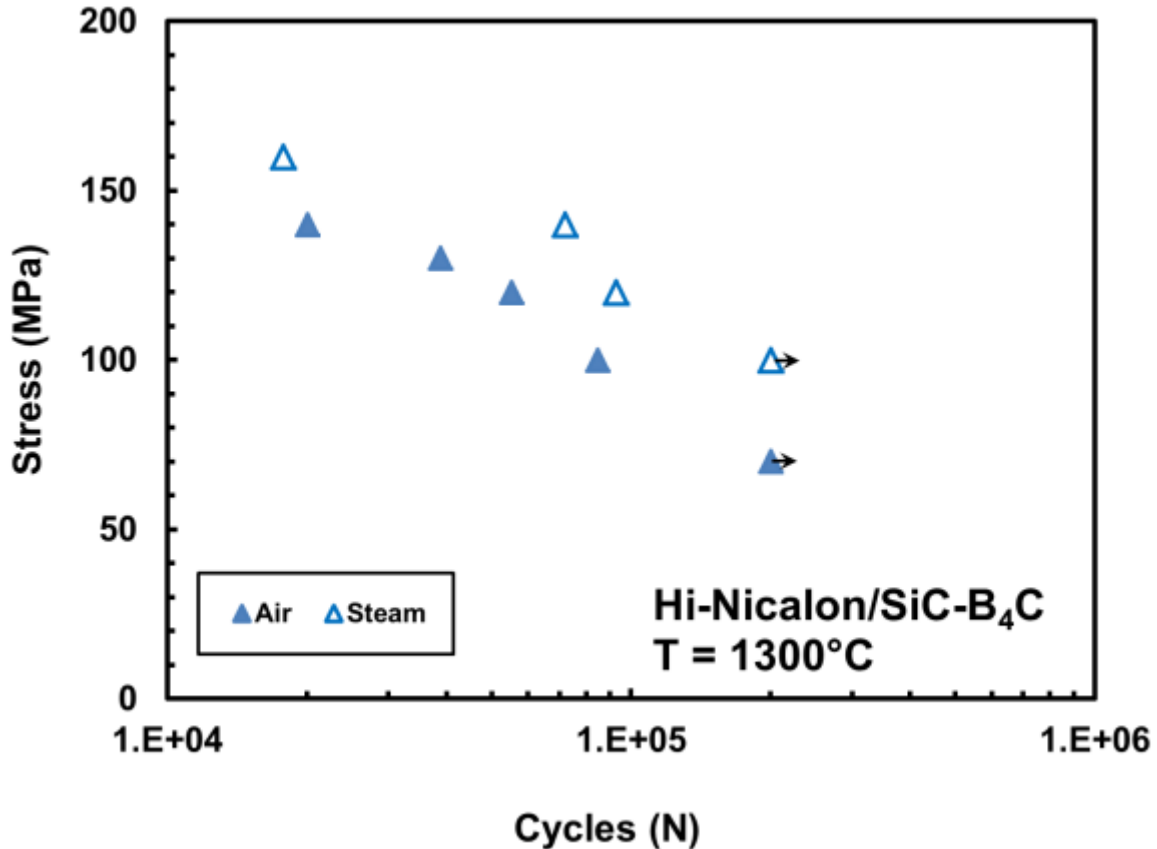
Figure 20. Stress vs. cycles to failure for dogbone-shaped specimens of Hi-Nicalon/SiC-B$_4$C ceramic composite at 1300°C in air and in steam. Arrow indicates that failure of specimen did not occur when the test was terminated

Results in Figure 20 shows that the environment affected the fatigue life of this material. The data in Table 8 also shows accumulated failure strains as high as 1-2% prior to failure at higher stress levels. The S-N diagram shows that for all stress levels the fatigue life in steam was higher than that of air. The steam environment also showed a higher run out stress level than that obtained in air. For the dogbone-shaped specimens, fatigue run-out in air and in steam was achieved at 70 MPa and 100 MPa respectively. For the hourglass-shaped specimens, fatigue run-out stress was 80 MPa and 100MPa in air and in steam respectively. Table 9 below summarizes the change in cyclic life due to the presence of a steam environment for the dogbone-shaped specimens.

33

Table 9. Change in fatigue life due to steam for dogbone-shaped specimens of Hi-Nicalon/SiC-B$_4$C ceramic composite at 1300°C.

Maximum Stress (MPa)	Cycles to failure (N)		Change in life (%)
	Air	Steam	
140	20069	72074	259.1
120	55199	93016	68.5
100	84855	200000[a]	135.7

a. Run-out defined as 2×10^5 cycles. Failure of specimen did not occur when the test was terminated.

Results in Table 9 suggest that steam has a moderately beneficial effect on the fatigue life at 1300°C. It is instructive to compare results obtained in this work to the results by Delapasse [10] for the same composite at 1200°C, shown in Table 10 and Figure 21.

Table 10. Summary of fatigue results for dogbone-shaped specimens of Hi-Nicalon/SiC-B$_4$C ceramic composite at 1200°C and 1300°C in air and in steam. Data from Delapasse[10].

Temperature (°C)	Maximum Stress (MPa)	Cycles (N)		Change in life (%)
		Air	Steam	
1300	140	20069	72074	259.1
1300	120	55199	93016	68.5
1300	100	84855	200000[a]	135.7
Delapasse				
1200	140	63458	36679	-42.2
1200	130	95712	98462	2.8
1200	120	119530	119931	0.3
1200	100	200000[a]	200000[a]	0.0

a. Run-out defined as 2×10^5 cycles. Failure of specimen did not occur when the test was terminated.
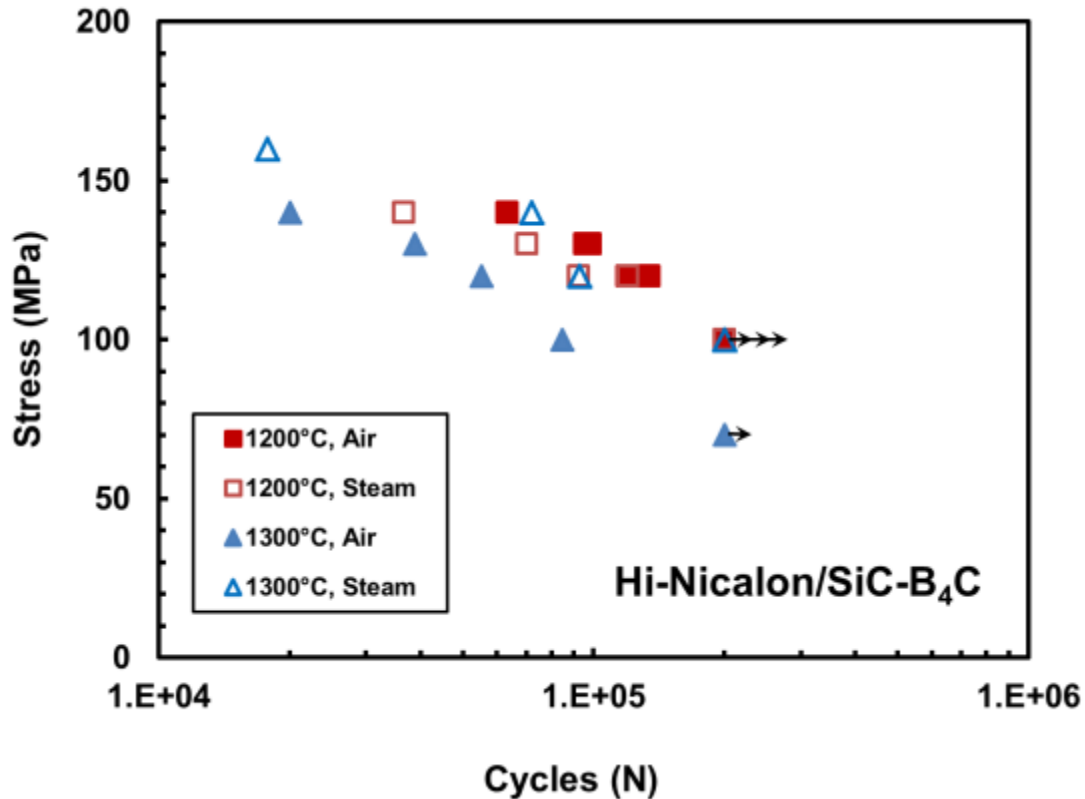
Figure 21. Stress vs. cycles to failure for dogbone-shaped specimens of Hi-Nicalon/SiC-B$_4$C ceramic composite at 1200°C and 1300°C in air and in steam. Data at 1200°C from Delapasse[10].

Results in Figure 21 reveal that fatigue life decreases as the temperature increases from 1200 to 1300°C. Cyclic lives obtained at 1300°C are reduced by at least a factor of 2 compared to cyclic lives produced at 1200°C. Furthermore, at 1200°C moderate degradation of fatigue life due to steam was observed at higher stress levels. At 1300°C steam appears to have a somewhat beneficial effect on the fatigue life. Fatigue results obtained for the hourglass-shaped (HG) and the dogbone-shaped (DB) specimens at 1300°C in air and in steam are presented in Figure 22 and 23, respectively.

www.manaraa.com
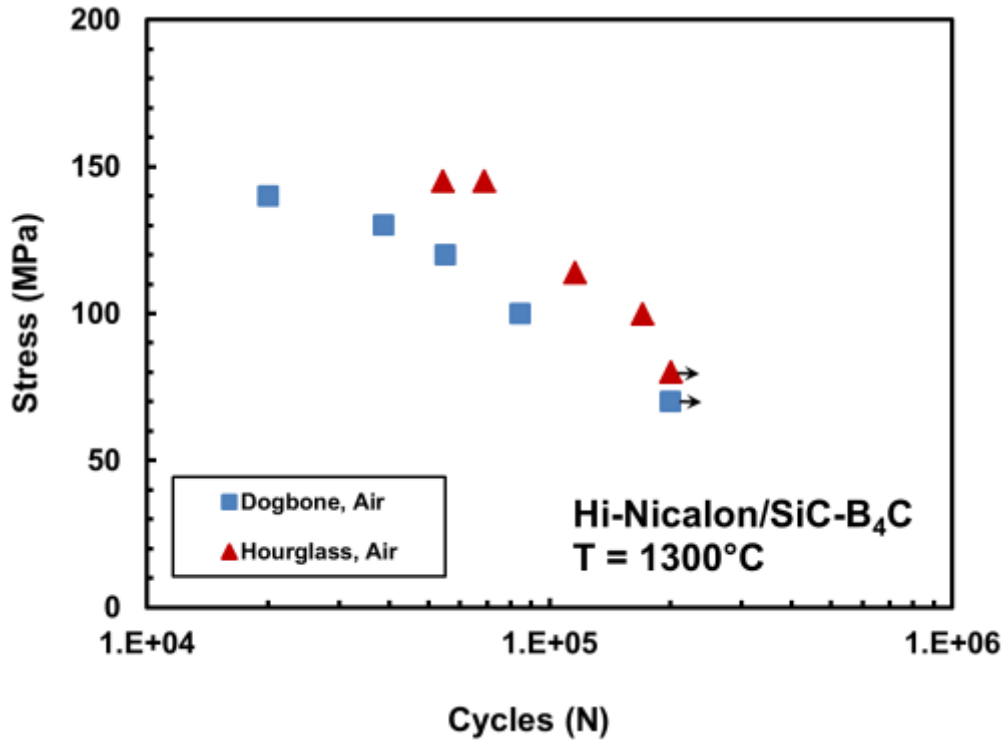
Figure 22. Stress versus cycles to failure for the DB and HG specimens at 1300°C in air.
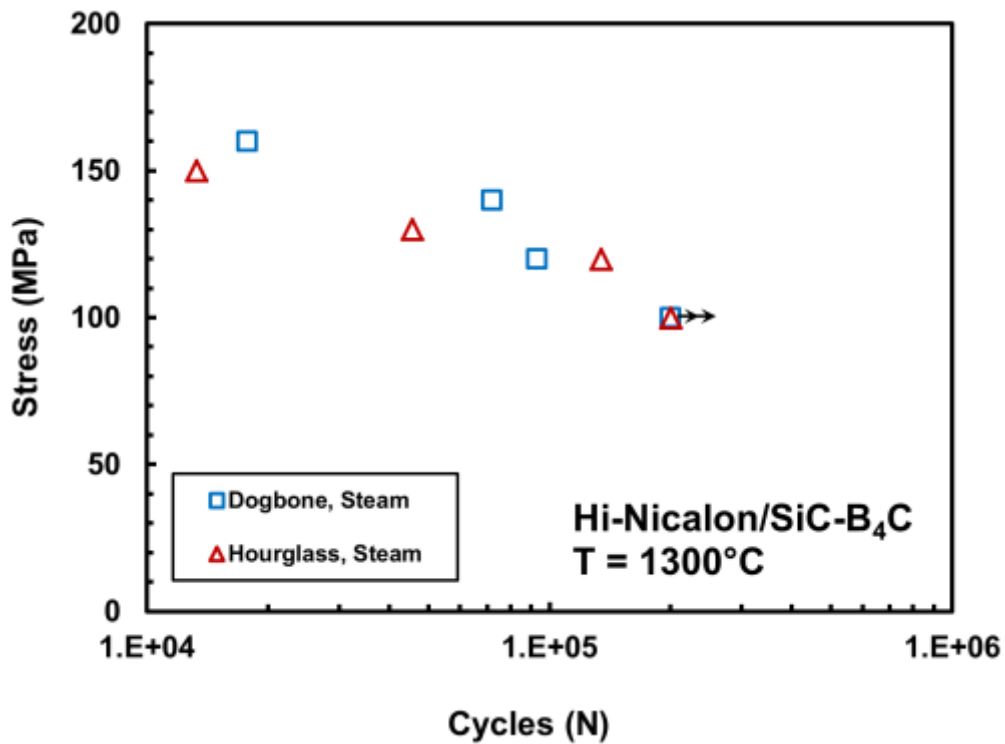
Figure 23. Stress versus cycles to failure for the DB and HG specimens at 1300°C in steam.

36

At 1300°C in air, slightly longer lives were produced for the HG specimens than for the DB specimens. This result is likely due to the rapidly changing cross sectional area of the HG specimen starting at the center and moving towards the ends of the specimen. A finite element analysis of the HG specimen performed at AFRL shows that the stress quickly decays moving from the center towards the ends of the HG specimen. Such stress decreases does not occur in a DB specimen with a straight gage section [11]. The S-N diagram in Figure 24 reveals that steam has little effect on the fatigue life of the HG specimens at 1300°C.
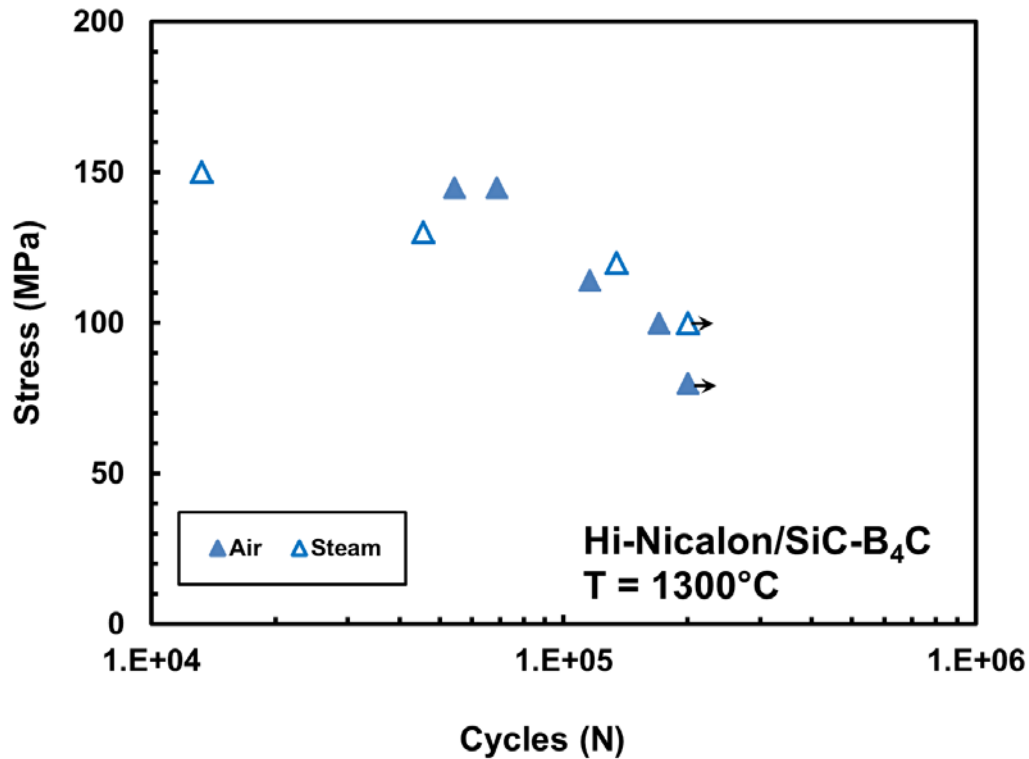
Figure 24. Stress vs. cycles to failure for HG specimens for Hi-Nicalon/SiC-B₄C ceramic composite at 1300°C in air and in steam.

37

Understanding how the fatigue cycling affects the stiffness of the material specimens is important. The hysteretic modulus was determined for each specimen by using the minimum and maximum stress and strain values from the peak-valley data collected during testing. The normalized modulus was generated by dividing the modulus determined at each cycle by the modulus of the first cycle. Figure 25 and Figure 26 show the evolution of the normalized modulus with fatigue cycles at 1300°C in air and in steam, respectively. The data showed a loss of stiffness as fatigue cycles increased for every sample tested at 1300°C in air except for the run-out specimen tested at 70 MPa. Generally the loss of stiffness with cycles increased as the maximum stress increased.
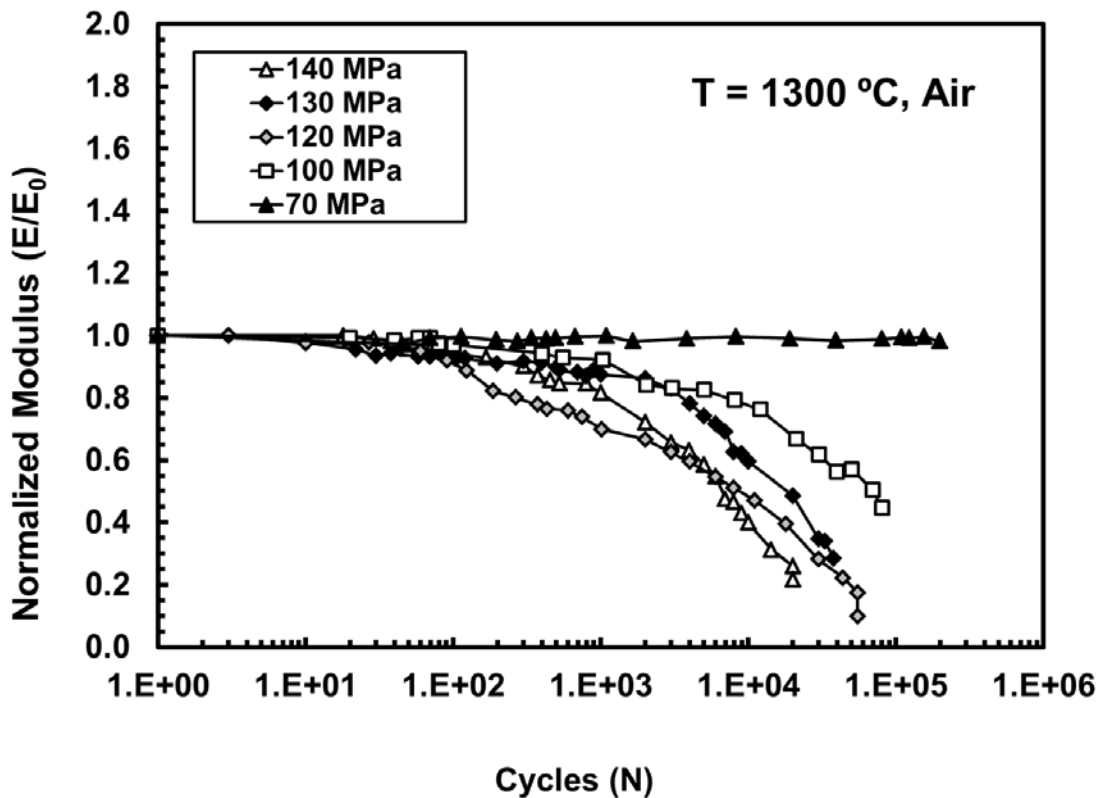
Figure 25. Normalized modulus vs. fatigue cycles for Hi-Nicalon/SiC-B₄C at 1300°C in air.
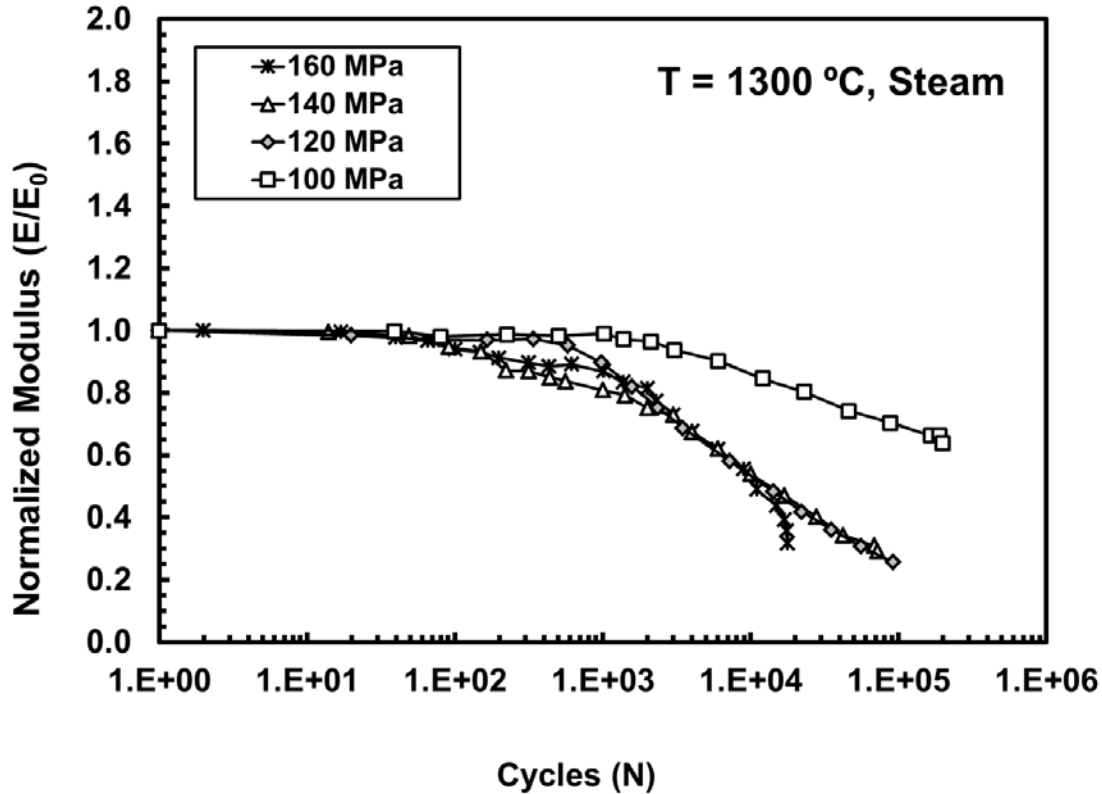
Figure 26. Normalized modulus vs. fatigue cycles for Hi-Nicalon/SiC-B$_4$C at 1300°C in steam.

The figure above shows that the same trends occur in the steam environment. All specimens tested in the steam environment including the run-out specimen showed degradation. Furthermore, the modulus degraded faster at higher maximum stress levels. The reduction in stiffness reached 90% in air and nearly 80% in steam.

The variation of normalized modulus with fatigue cycles observed at 1300°C were compared with the results reported by Delapasse [10] at 1200°C (see Figure 27). It appears that the modulus degradation with fatigue cycles is accelerated at 1300°C. Evolution of the normalized modulus with fatigue cycles is presented In Figure 28. Greater reductions in modulus are seen at 1300°C in steam that at 1200°C in steam. For example modulus reduction in the 120 MPa test in steam was ~50% at 1200°C and ~75% at 1300°C.

39
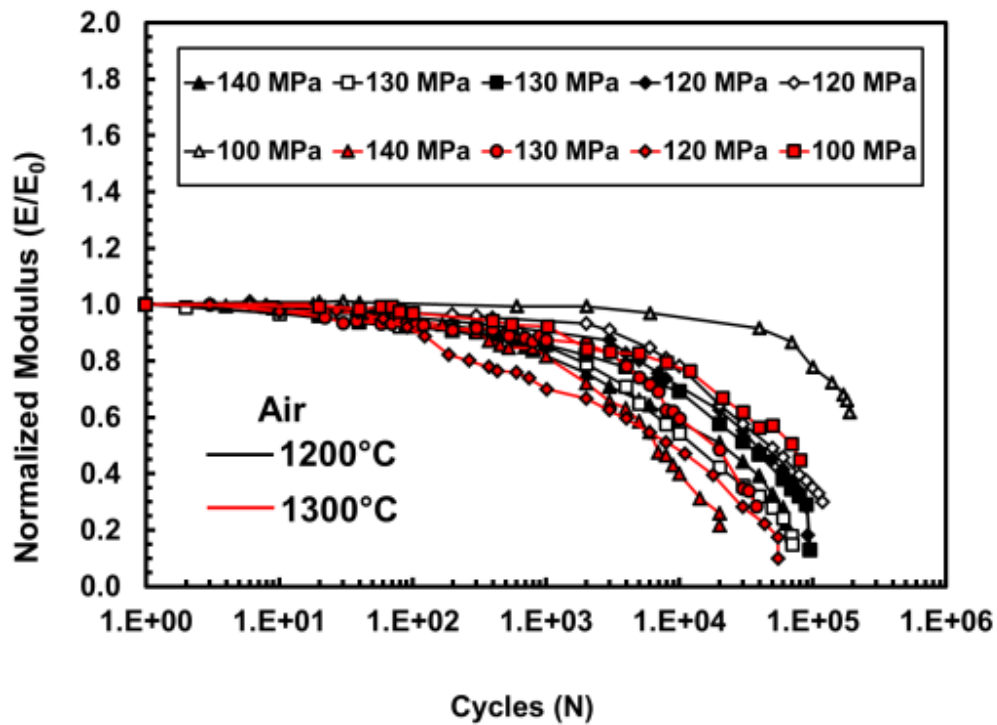
Figure 27. Normalized modulus vs. fatigue cycles for Hi-Nicalon/SiC-B₄C at 1200°C and 1300°C in laboratory air. Data at 1200°C from Delapasse [10].
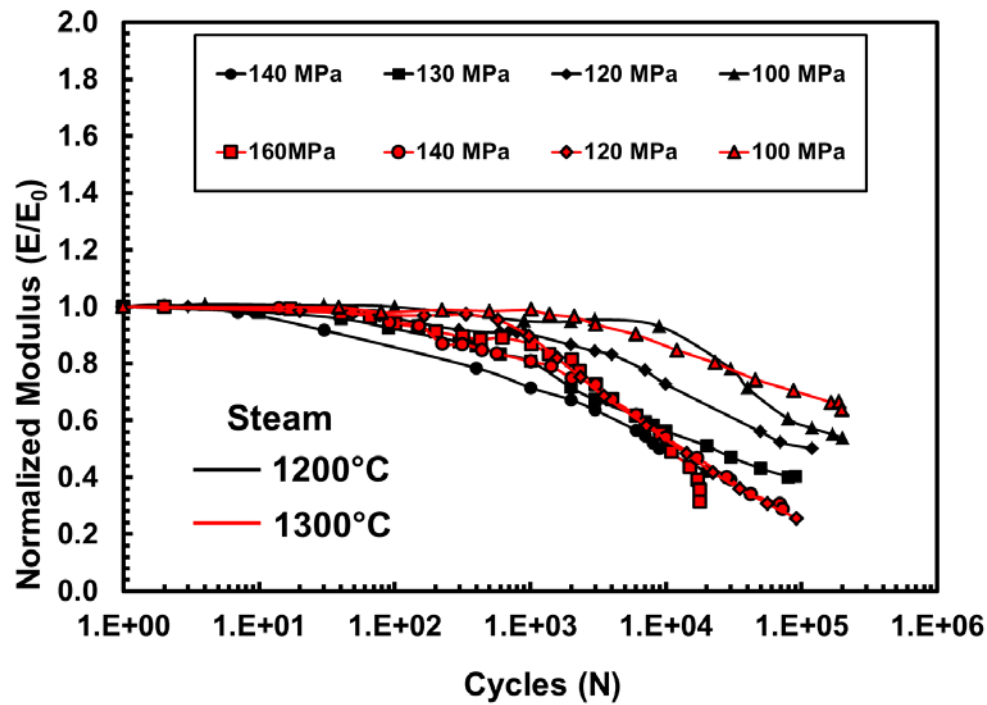
Figure 28. Normalized modulus vs. fatigue cycles for Hi-Nicalon/SiC-B₄C at 1200°C and 1300°C in steam. Data at 1200°C from Delapasse [10].

The accumulated strain was also evaluated for this composite at 1300°C in air (Figure 29) and in steam (Figure 30). At 1300°C in air, the accumulated strain increased as the maximum stress increased. The highest accumulated strain was 2.6% at 140 MPa and the lowest was 0.34% at 100 MPa. In steam, the highest strains of 1.07% were accumulated in 140 and 120 MPa tests (Figure 30).
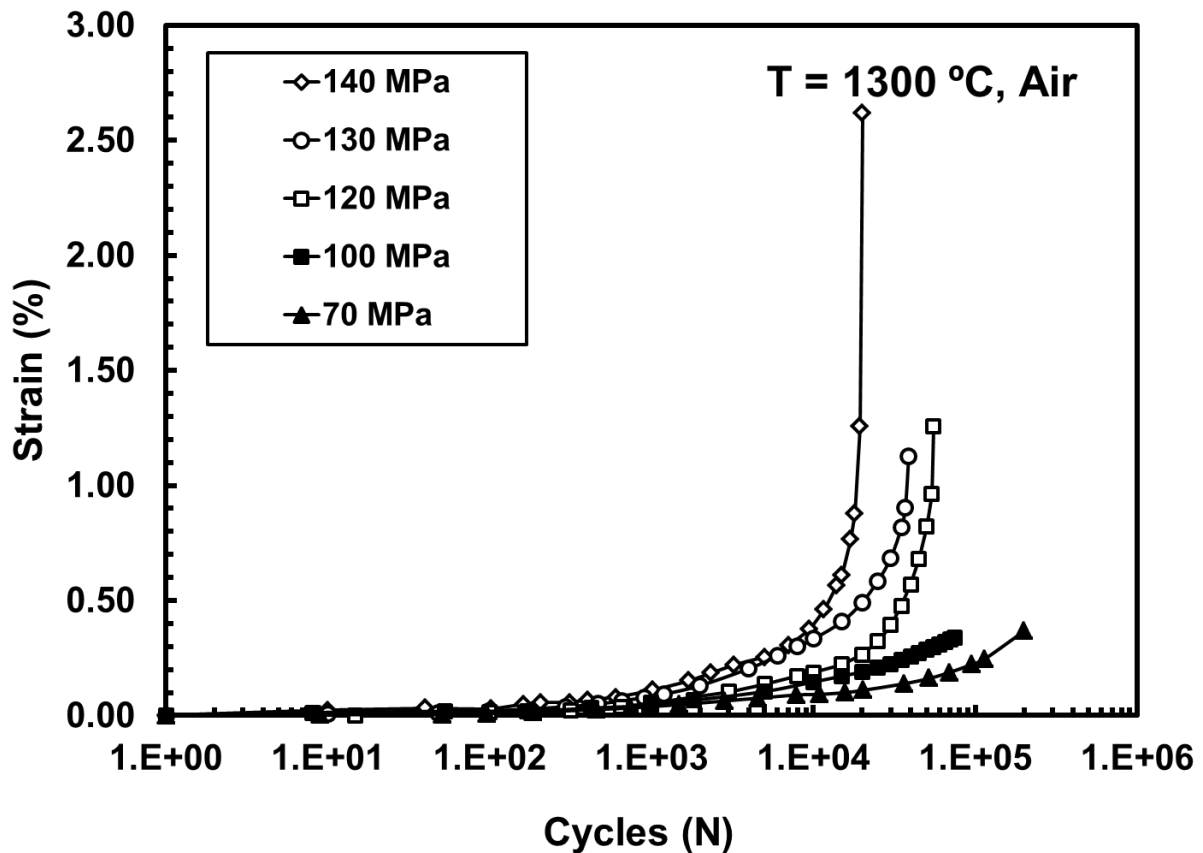
Figure 29. Accumulated strain vs. fatigue cycles for Hi-Nicalon/SiC-B$_4$C **at 1300°C in laboratory air.**
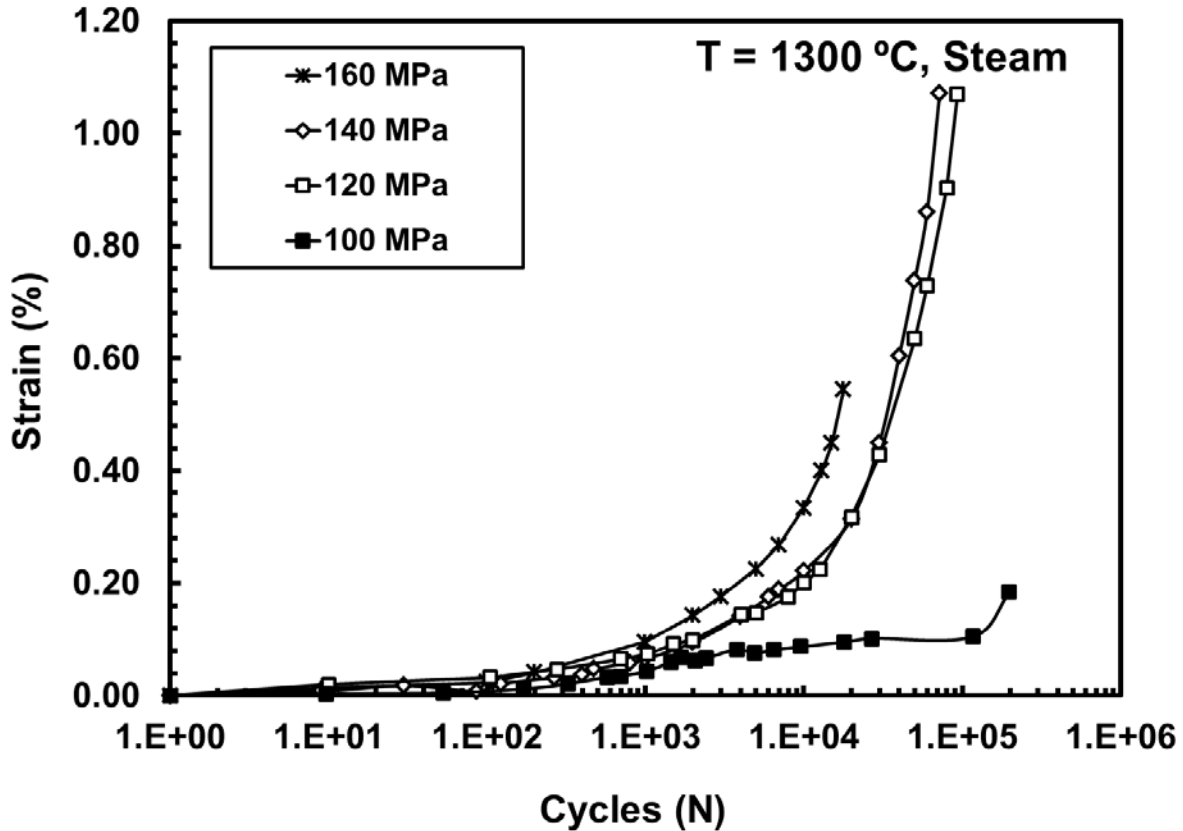
Figure 30. Accumulated strain vs. fatigue cycles for Hi-Nicalon/SiC-B$_4$C at 1300°C in steam.

The accumulation of strain with fatigue cycles observed at 1300°C in air was compared with results reported by Delapasse [10] at 1200°C (see Figure 31 and 32). At 1300°C in air, we observed in higher accumulated strain for all stress levels over those reported by Delapasse. It appears that strain accumulation is accelerated at 1300°C over 1200°C. For example in air, the accumulated strain for the 140MPa test at 1300°C reached 2.6% while the same stress at 1200°C only reached 0.57%. Accumulated strain with fatigue cycles in steam at 1200°C and 1300°C is presented in Figure 32. Higher accumulated strain was observed at 1300°C in steam than at 1200°C in steam. For example in steam, the 140 MPa test at 1300°C and 1200°C in steam showed accumulated strains of 1.07% and 0.27% respectively.

42
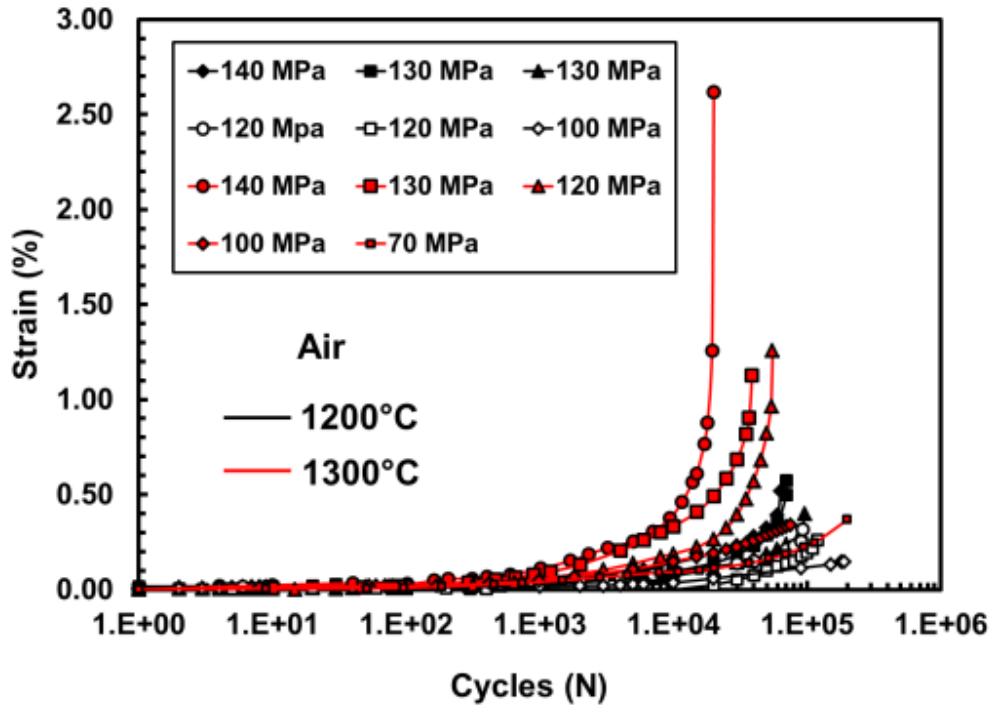
Figure 31. Accumulated strain vs. fatigue cycles for Hi-Nicalon/SiC-B₄C at 1200°C and 1300°C in laboratory air. Data at 1200°C from Delapasse [10].
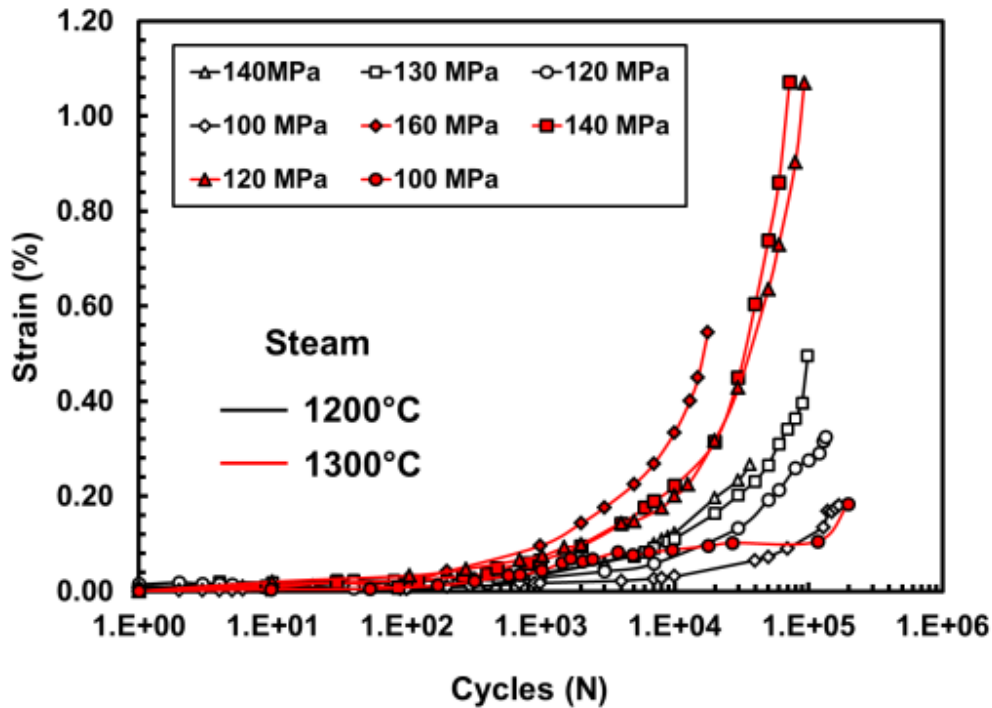
Figure 32. Accumulated strain vs. fatigue cycles for Hi-Nicalon/SiC-B₄C at 1200°C and 1300°C in steam. Data at 1200°C from Delapasse [10].

Typical evolution of the hysteretic stress-strain response with cycles obtained with σ_{max}

of 140 MPa at 1300°C in air and in steam is shown in Figure 33 and Figure 34, respectively.

Recall that the specimen tested with σ_{max} of 140 MPa in air survived 20,069 cycles, while the

specimen tested with σ_{max} of 140 MPa in steam survived 72,074 cycles. The data shows a

continuous increase in strain with increasing fatigue cycles, often termed strain ratcheting. The

graphs also show the reduction in the modulus as the slope, from valley to peak, of the overall

cycle decreases with increasing cycles. Recall that the strain data were collected for DB

specimens only. The first cycle does not reach the maximum stress due to the stiffness of the

material. The feedback then adjusts to better reach the desired load on the subsequent cycles.
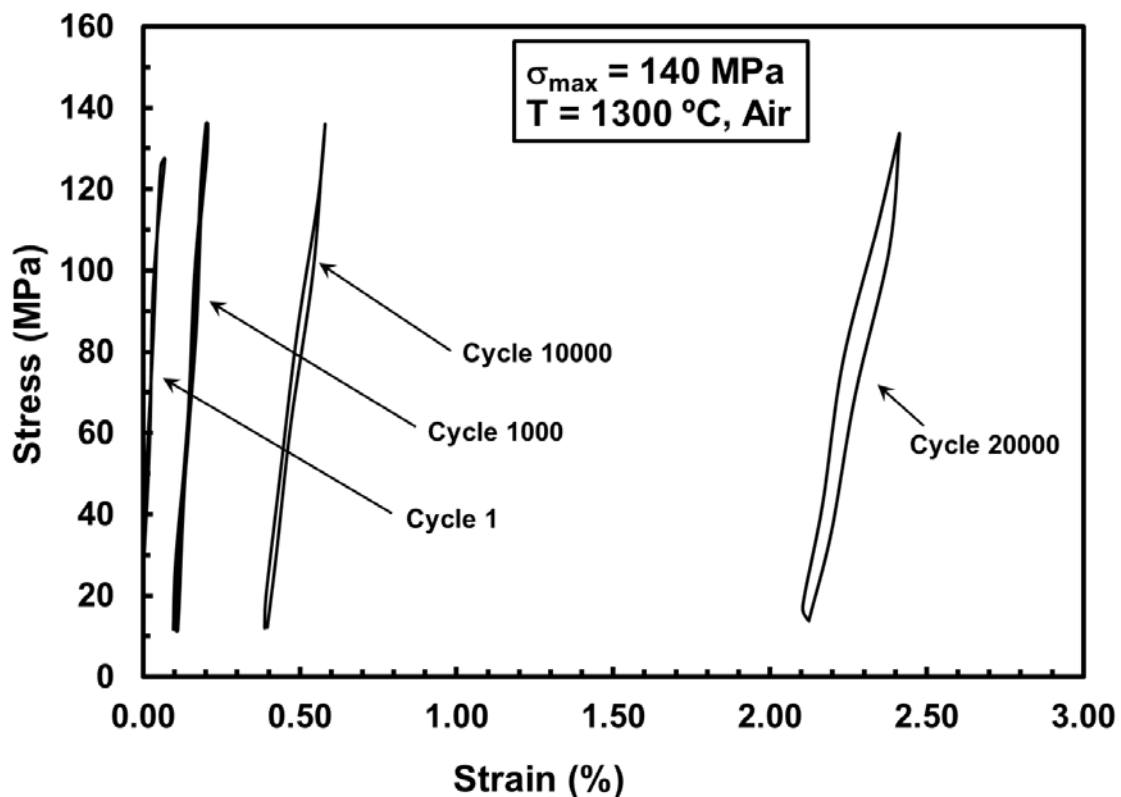
Figure 33. Evolution of hysteretic stress-strain response of Hi-Nicalon/SiC-B₄C ceramic composite with fatigue cycles in air at 1300 °C, σ_{max} = 140 MPa, N_f = 20,069.

44
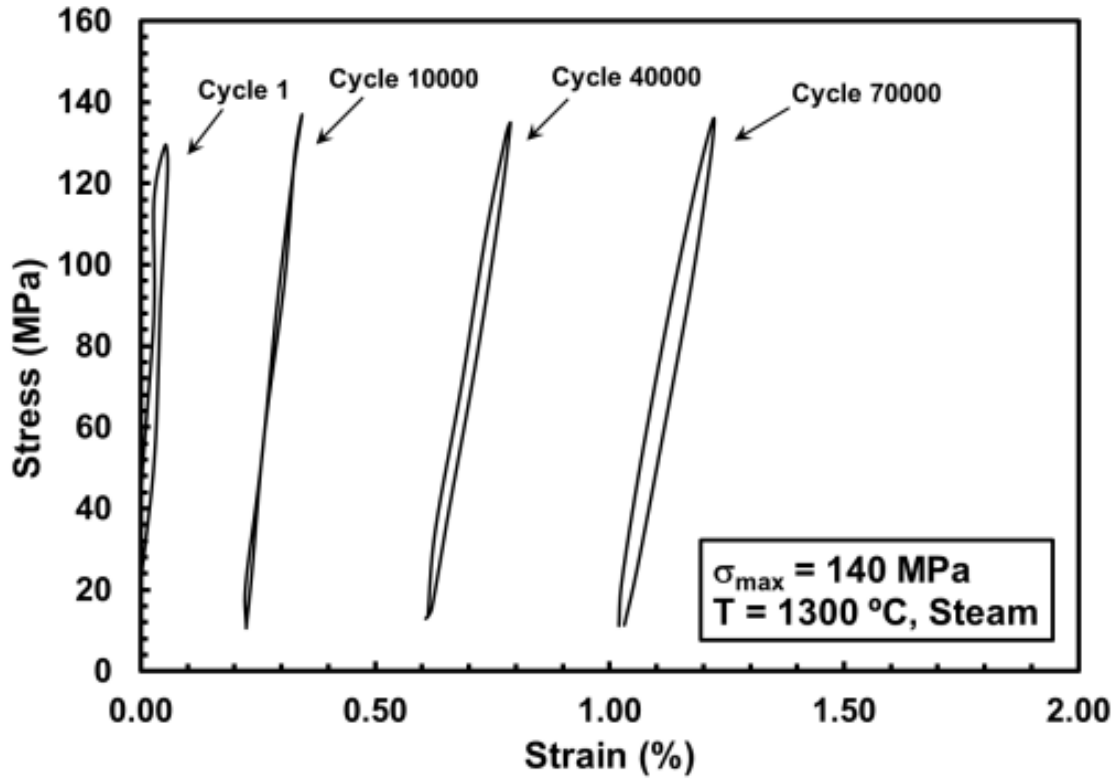
Figure 34. Evolution of hysteretic stress-strain response of Hi-Nicalon/SiC-B₄C ceramic composite with fatigue cycles in steam at 1300 ˚C, σ_max = 140 MPa, N_f = 72,074

5.5 Effects of Prior Fatigue on Tensile Properties

All specimens that achieved fatigue run-out were tested to failure in tension to determine the retained tensile properties. The data collected from these tensile tests are summarized in 11. The DB specimen pre-fatigued in air at 70 MPa experienced no loss in strength or modulus. However, the DB specimen that was pre-fatigued at 100 MPa in steam retained only about 49% of its strength and 64% of its stiffness. The HG specimens that achieved run-out at 80 MPa in air retained about 94% of its tensile strength. The HG specimen fatigued at 100 MPa in steam retained only about 59% of its tensile strength.

Table 11. Retained tensile properties of Hi-Nicalon/SiC-B$_4$C specimens subjected to prior fatigue in laboratory air and in steam at 1300˚C.

Fatigue Stress (MPa)	Test Environment	Retained Strength (MPa)	Strength Retention (%)	Retained Modulus (GPa)	Modulus Retention (%)	Failure Strain (%)
70	Air	311	100	238	100	0.50
100	Steam	152.1	48.9	155.1	63.9	0.13
Hourglass Specimens						
80	Air	291	93.6	-	-	-
100	Steam	183	58.8	-	-	-

The stress-strain curves obtained from the post-fatigue tensile tests are shown in Figure 35 for the DB specimens. A representative for the as-processed composite is included for comparison. As the figure shows, prior fatigue with σ_{max} of 70 MPa in air failed at a lower strain but still achieved the average UTS of 311 MPa. Conversely, the specimen pre-fatigued at 100 MPa in steam failed at less than half of the average UTS (311 MPa). The specimen also showed a reduced modulus as compared to that measured on the first cycle. Prior fatigue in air and steam had little effect on the shape of the tensile stress-strain behavior when compared to that of the as-processed material.
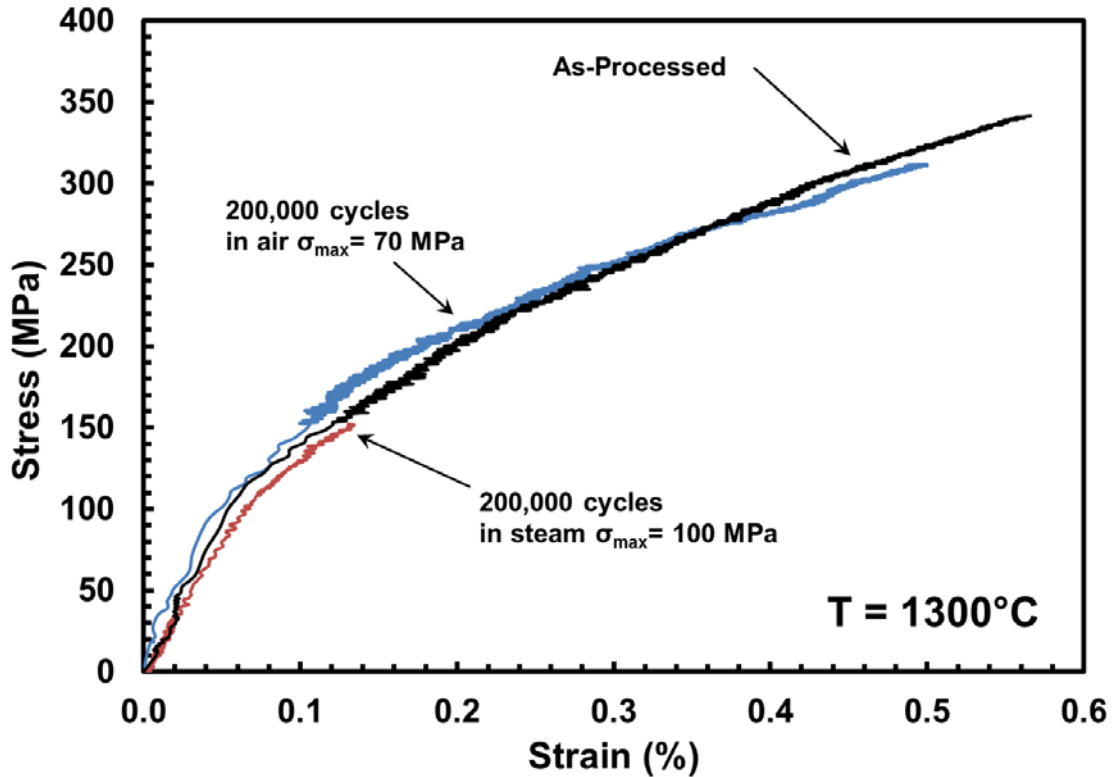
Figure 35. Effect of prior fatigue on tensile stress-strain behavior of Hi-Nicalon/SiC-B$_4$C ceramic composite at 1300°C.

5.6 Composite Microstructure

The following sections provide analysis of the fracture surfaces of the tested specimens using an optical microscope and an SEM. All of the DB-shaped specimens and a representative group of the HG-shaped specimens were analyzed using these techniques. A representative group of HG-shaped specimens were used because similar surface features were observed in all specimens subjected to the same test conditions. When a specimen failed the testing system was promptly shut off and the bottom half of the specimen was removed from the furnace. Hence, the interior of the fracture surface of the bottom half of the failed specimen was exposed to significant temperatures and prolonged oxidation for a few minutes at most. These are the fracture surfaces that were examined with optical microscopy and the SEM.

5.6.1 Microstructural Characterization of Tensile Test Specimens

Optical and SEM micrographs were taken of the tensile test specimen L97 to analyze the fracture surface. Figure 36 below shows both a front and side view of the tensile specimen after failure. The specimen fractured transversely, perpendicular to the loading direction. The optical micrograph shows that there is very little fiber pull-out along the fracture surface. The side view shows no delamination of the specimen. Figure 37 below shows an SEM micrograph of the full top down fracture surface. Figure 37 shows there is very little change across the fracture surface of the specimen. The brushy nature is caused by the exposed fibers after failure. There are no visible oxidized regions.
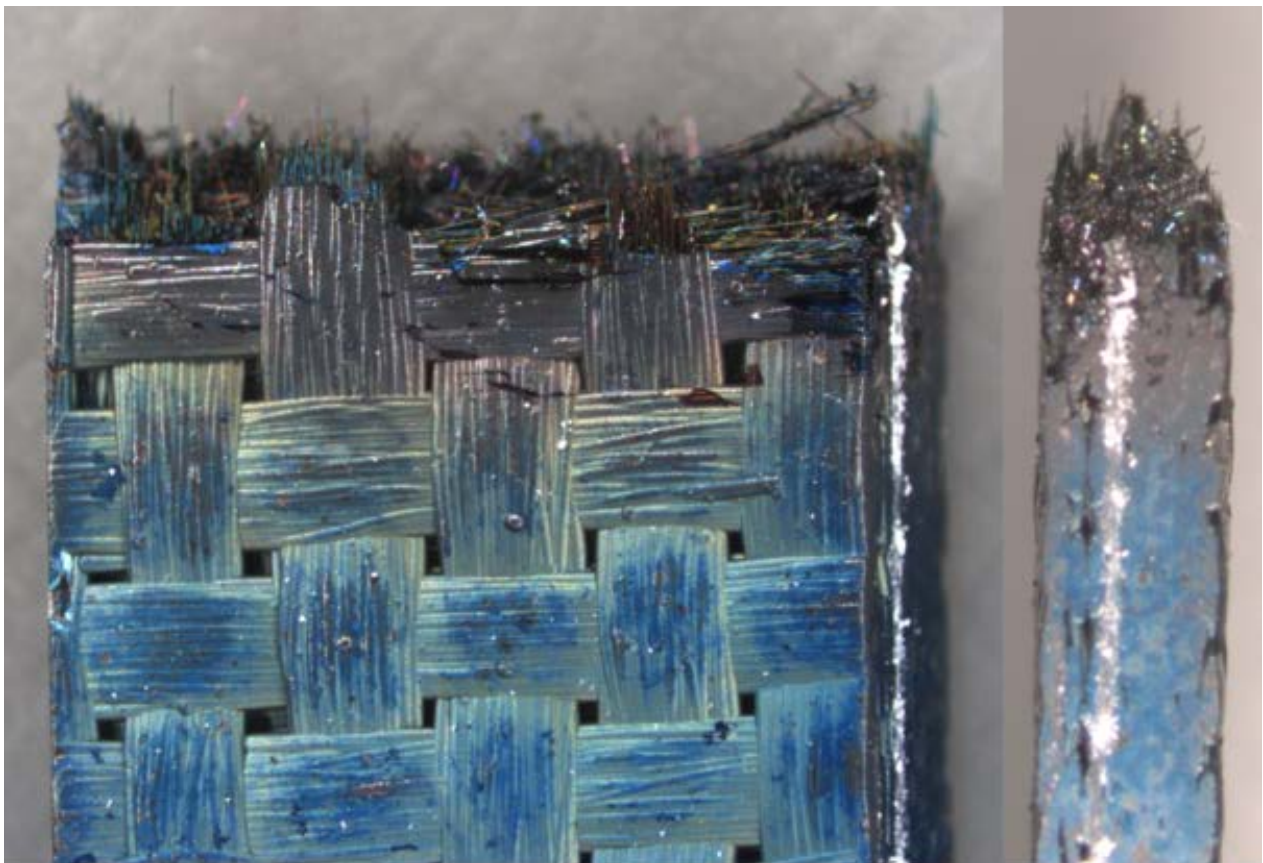
Figure 36. Optical micrographs of the fracture surface produced in tensile test to failure of specimen L97 conducted at 0.05 mm/s at 1300 °C in air.

Figure 37. SEM micrograph of fracture surface of the specimen tested in tension to failure at 1300 °C.

49

Figure 38 shows three micrographs of regions on the sample in various locations along outer edge of the sample. These micrographs confirm there is no visible oxidation of the matrix surface, with the matrix layers still visible in the bottom right micrograph. Since this sample was tensile tested, the specimen only spent about 30 seconds within the thermal environment before fracture. There is some slight oxidation on the surface of the pull out fibers as shown by the smooth slightly rounded surfaces at the tip of the fibers in Figure 39 .
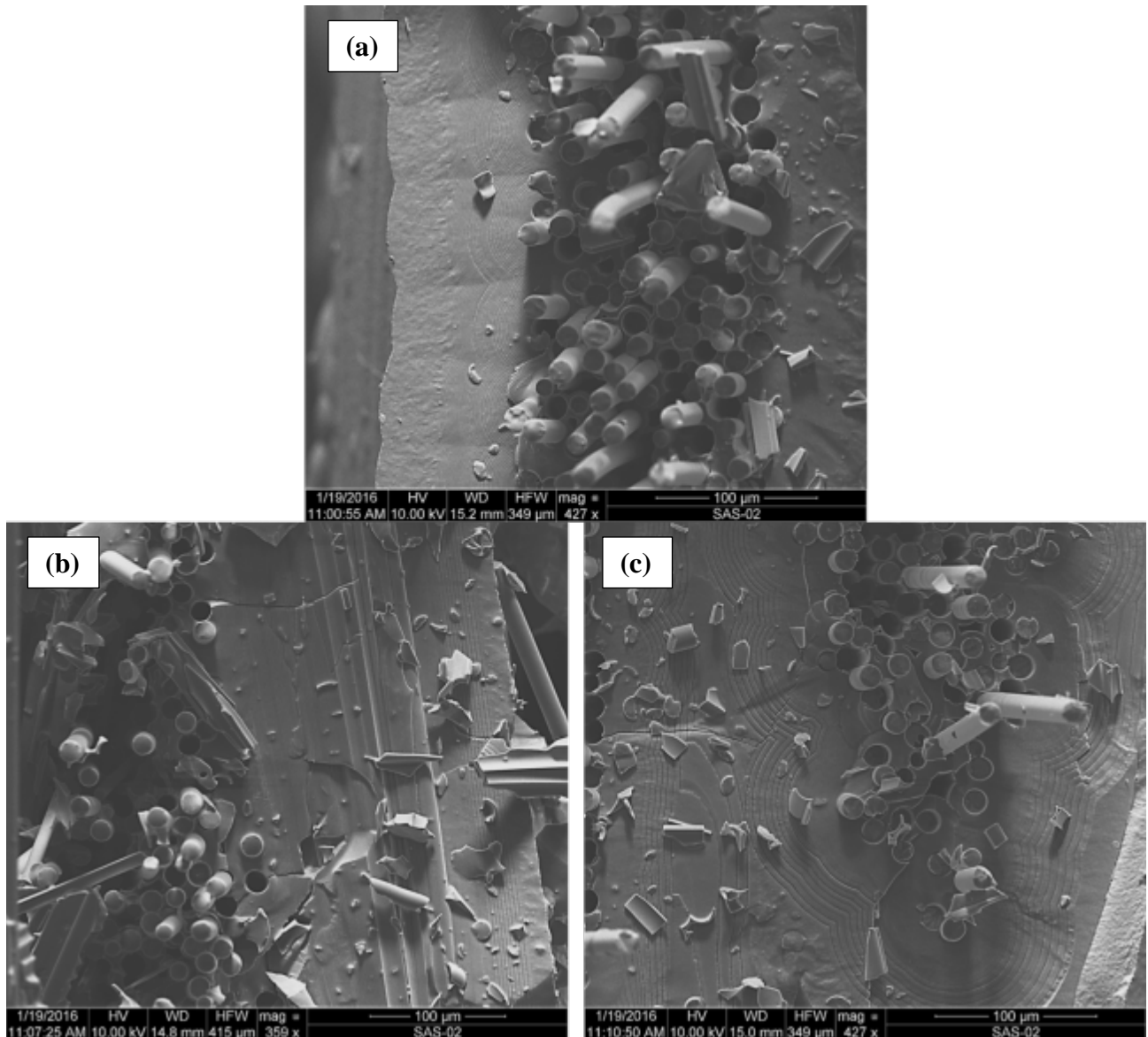
Figure 38. SEM micrographs of non-oxidized regions of the tensile test specimen L97, 0.05 mm/s at 1300 °C in air. Shows regions with no matrix oxidation.

50
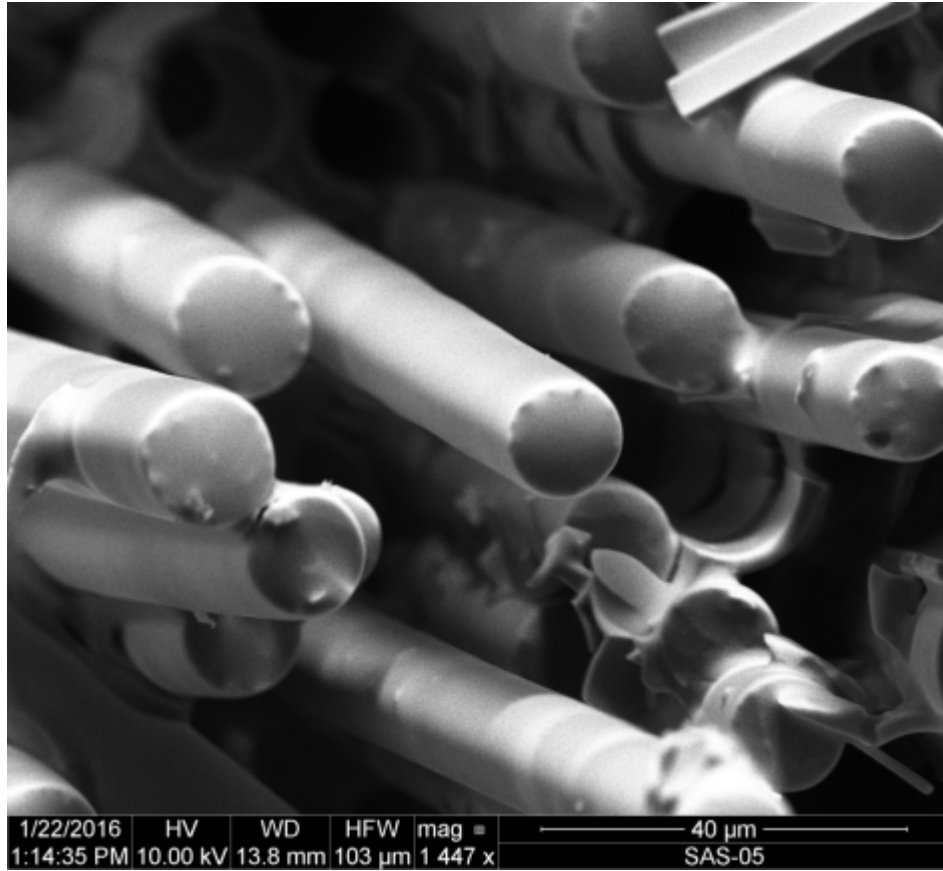
Figure 39. SEM micrograph of pulled out fibers. Note oxidation on the fiber fracture surface.

51

5.6.2 Microstructural Characterization of Fatigue Test Specimens

Optical and SEM micrographs were also taken of most of the fatigue specimen. These were analyzed qualitatively to provide information about specimen failure. Optical micrographs are provided for the DB-shaped specimens tested with σ_{max} of 140 MPa and 70 MPa in air in Figure 40 and Figure 41, respectively. Optical micrographs are also provided for the DB-shaped specimens tested with σ_{max} of 160 MPa and 100 MPa in steam in Figure 42 and Figure 43 respectively. Optical micrographs are provided for the HG-shaped specimens tested with σ_{max} of 145 MPa in air and of 150 MPa in steam in Figure 44 and Figure 45 respectively.

The optical micrographs in Figure 40 show that the specimen tested with σ_{max} of 140 MPa had increased fiber pull-out. Furthermore, we notice the cracking of the 0° fiber bundles on the specimen surface (see arrows in Fig. 40 (a)). In DB-shaped specimens, this type of cracking is seen only in specimens tested with higher levels of σ_{max}. Figure 41 presents the fracture surface of the specimen that achieved fatigue run-out with σ_{max} of 70 MPa in air and was subsequently tested in tension to failure at 1300°C. Notably the fracture surface in Figure 41 (a) is similar to that produced in tension test to failure of the as-processed specimen (Fig. 36). The side views of both specimens exhibit little to no delamination. While it looks like there is some debonding of the fiber tows shown in the side view in Figure 41 (b), it does not translate all the way through the specimen so is not considered delamination.

52

Figure 40: Optical micrograph of fracture surface of the DB-shaped specimen tested in fatigue at 1300°C in air. σ_{max} = 140 MPa, N_f = 20,069, t_f = 5.6 h. (a) front, (b) side.

Figure 41. Optical micrograph of fracture surface of the DB-shaped specimen tested in fatigue at 1300°C in air. σ_{max} = 70 MPa, N_f = 200,000, t_f = 55.6 h. (a) front, (b) side.

Figure 42 and 43 show optical micrographs of the fracture surfaces produced in fatigue

tests performed at 1300°C in steam with σ_{max} of 160 MPa and 100 MPa, respectively. The

fracture surfaces in figures 42 and 43 show some fiber pull-out but little or no delamination.

Note the transverse cracking of some 0° fiber bundles on the specimen surface (see arrows in

Figures 42 (a) and 43 (a)) akin to that seen in Figure 40 (a). Also seen in Figure 42 (a) and Figure

43 (a) are the presence of large rounded surface features. These surfaces features are attributed to

being oxidation products on the surface of the specimen. The specimens tested in steam have

larger areas of oxidation products on the surface than the specimens tested in air (Figure 40 and

41). Their presence on the specimens subjected fatigue in steam is most likely due to the more

aggressive oxidizing environment that steam causes.

Figure 42. Optical micrograph of fracture surface of the DB-shaped specimen tested in fatigue at 1300°C in steam. σ_{max} = 160 MPa, N_f = 17,811, t_f = 4.9 h. (a) front, (b) side.

Surface reaction products

Figure 43. Optical micrograph of fracture surface of the DB-shaped specimen tested in fatigue at 1300°C in steam. σ_{max} = 100 MPa, N_f = 200,000, t_f = 55.6 h. (a) front, (b) side.

The optical micrographs of the fracture surfaces of the HG-shaped specimens tested in fatigue with the highest maximum stress levels are shown in Figure 44 and 45. The fracture surfaces in Figs 44 and 45 are similar to those obtained for the DB-shaped specimens. There is little or no delamination and some fiber pull-out. We also note the transverse cracking of the 0° fiber bundles on the surface of the HG specimens.
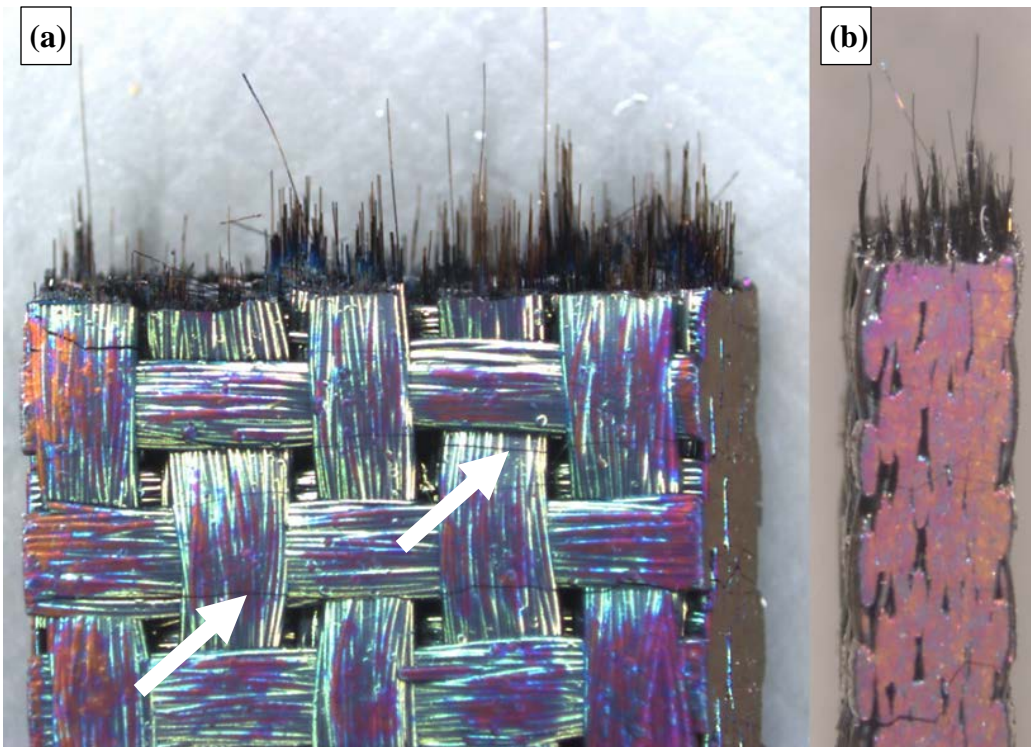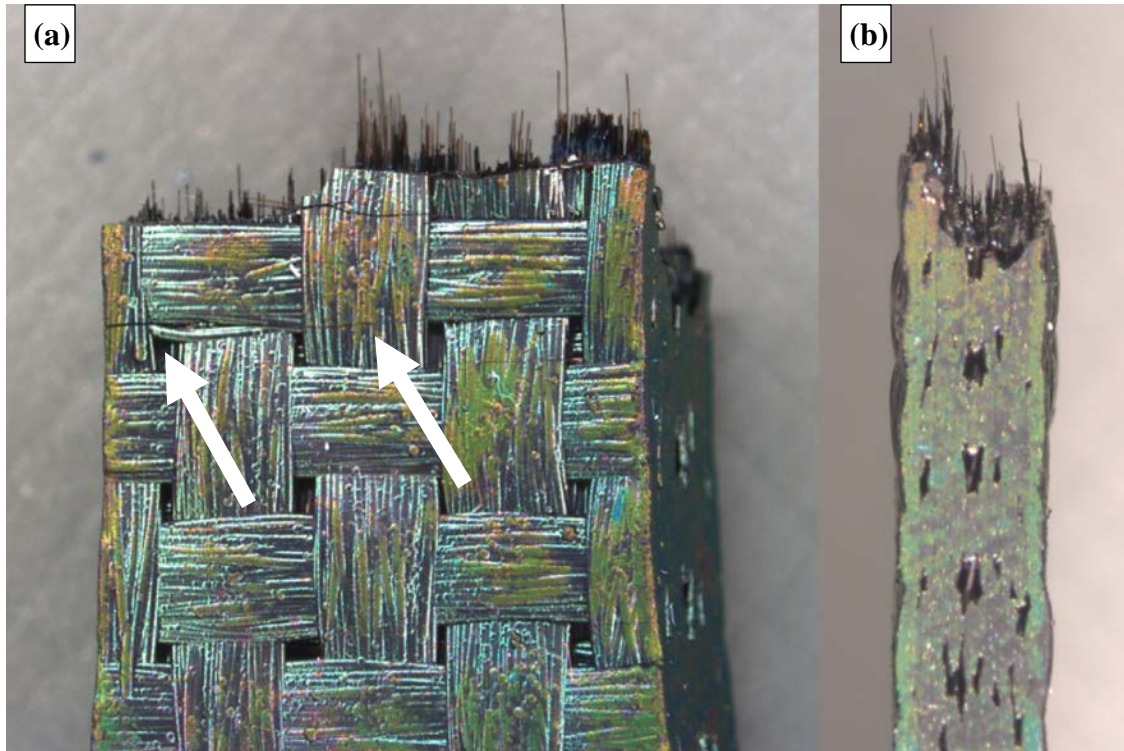
Figure 44. Optical micrograph of fracture surface of the HG-shaped specimen tested in fatigue at 1300°C in air. σ_{max} = 145 MPa, N_f = 68,831, t_f = 19.1 h. (a) front, (b) side.
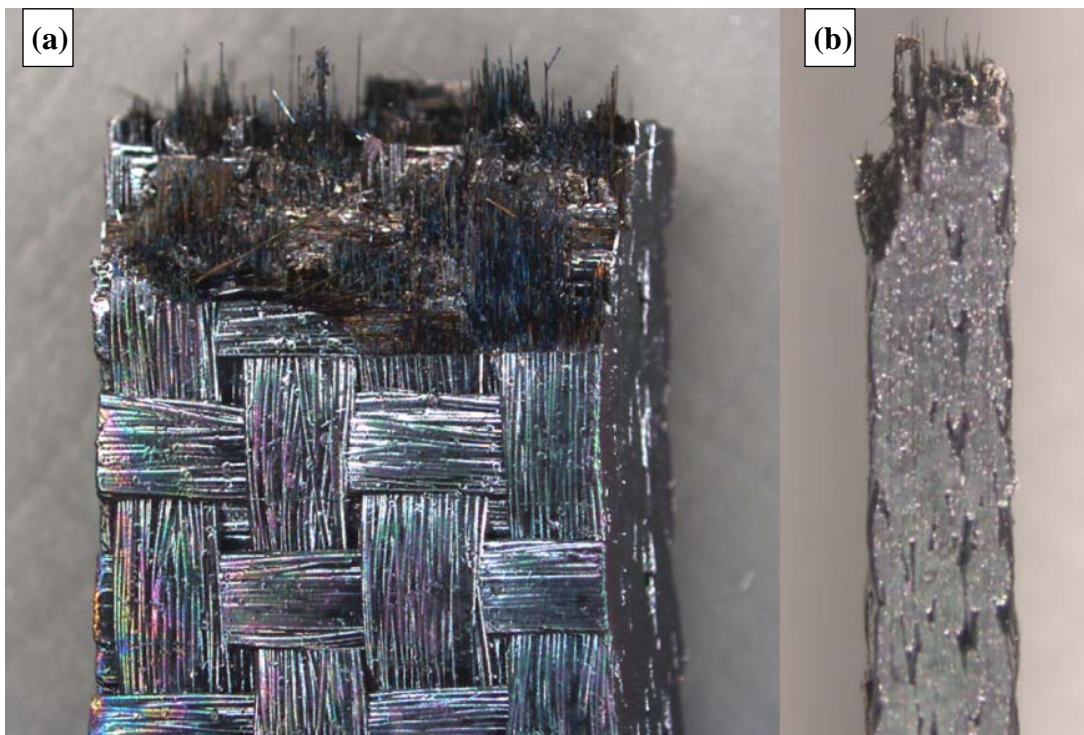
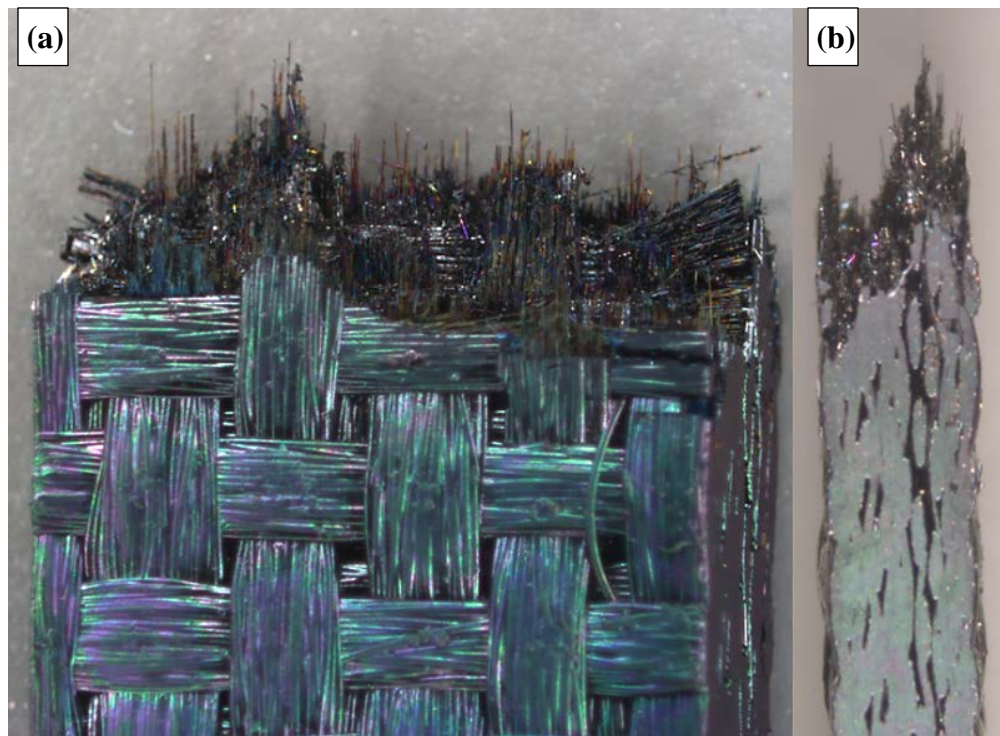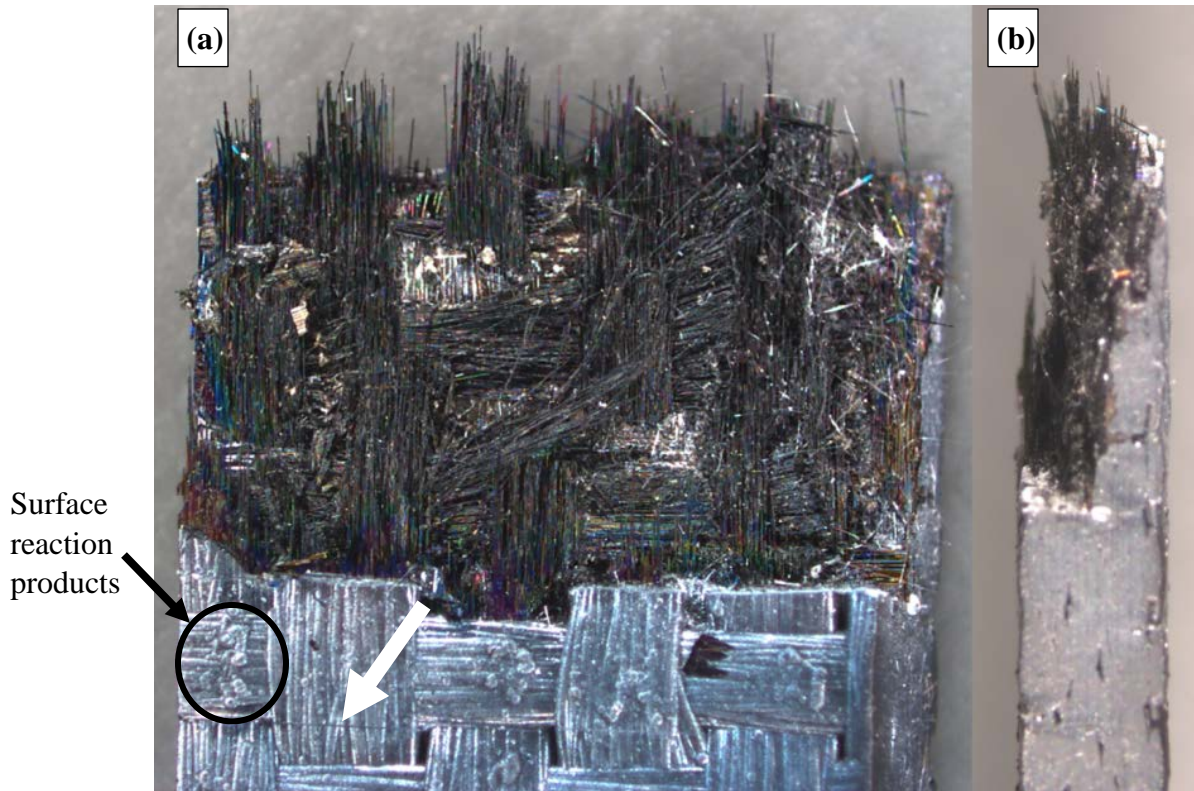**Figure 45. Optical micrograph of fracture surface of the HG-shaped specimen tested in fatigue at 1300°C in steam. σ_{max} = 150 MPa, N_f = 13,266, t_f = 3.7 h. (a) front, (b) side.**

An important feature seen in the micrographs in Figures 40 and 42-44 is the transverse cracking of the 0° fiber bundles of the specimen surface. The majority of these cracks are located at tow cross-overs in the woven surface layer. It is recognized that in woven CMCs bending and straightening of wavy fiber tow segments at tow cross-overs results in stress and strain concentrations [20]. Hence the transverse cracking of the 0° tows at the aforementioned locations in not surprising. Figure 46 shows the DB-shaped specimen tested in tension to failure. We do not observe transverse cracking of the 0° fiber bundles on the surface of the specimen shown in Figure 46. Conversely, the surface of the DB-shaped specimen tested in fatigue with σ_{max} of 140 MPa in air (see Figure 47) shows a proliferation of large transverse cracks of the 0° fiber bundles (arrows in Figure 47). Nearly the entire gage section of the specimen in Figure 47 exhibits such transverse cracks. Contrastingly, the surface of the DB-shaped specimen tested in fatigue with σ_{max} of 140 MPa in steam (Figure 48) shows only a few transverse cracks of the 0° fiber bundles. It is believed that the presence of steam accelerated the oxidation of the self-healing layered matrix at or near the specimen surface. The glassy phases formed as a result of oxidation filled and sealed most surface cracks.

57

Figure 46. Gage section of the DB-shaped specimen L97, tested in tension to failure at 0.05 mm/s at 1300°C in air.

Figure 47. Gage section of the DB-shaped specimen tested in fatigue at 1300°C in air, σ_{max} = 140 MPa, N_f = 20,069, t_f = 5.6 h. Transverse cracks of the 0° fiber bundles are visible on the specimen surface.

The gage section of the HG-shaped specimen tested in fatigue with σ_{max} of 145 MPa in air is shown in Figure 49. Some transverse cracks of the 0° fiber bundles are visible on the surface of this specimen as well. However, these cracks are few and most are located near the fracture surface. Recall that in the case of the HG-shaped specimen the stress begins to drop drastically as we move away from the middle of the hourglass section to the ends of the specimen. Hence only the small portion of the specimen in the vicinity of the middle of the hourglass section is subject to fatigue with the high maximum stress of 145 MPa. The rest of the specimen is subjected to fatigue with considerably lower stress. As a result we observe less damage to the specimen during fatigue and somewhat longer fatigue lives for the HG-shaped specimens compared to the DB-shaped specimens.

Figure 48. Gage section of the DB-shaped specimen tested in fatigue at 1300°C in steam. σ_{max} = 140 MPa, N_f = 72,074, t_f = 20.0 h. Transverse cracks of the 0° fiber bundles are visible on the specimen surface.

Figure 49. Gage section of the HG-shaped specimen tested in fatigue at 1300°C in air. σ_{max} = 145 MPa, N_f = 68,831, t_f = 19.1 h. Transverse cracks of the 0° fiber bundles are visible on the specimen surface.
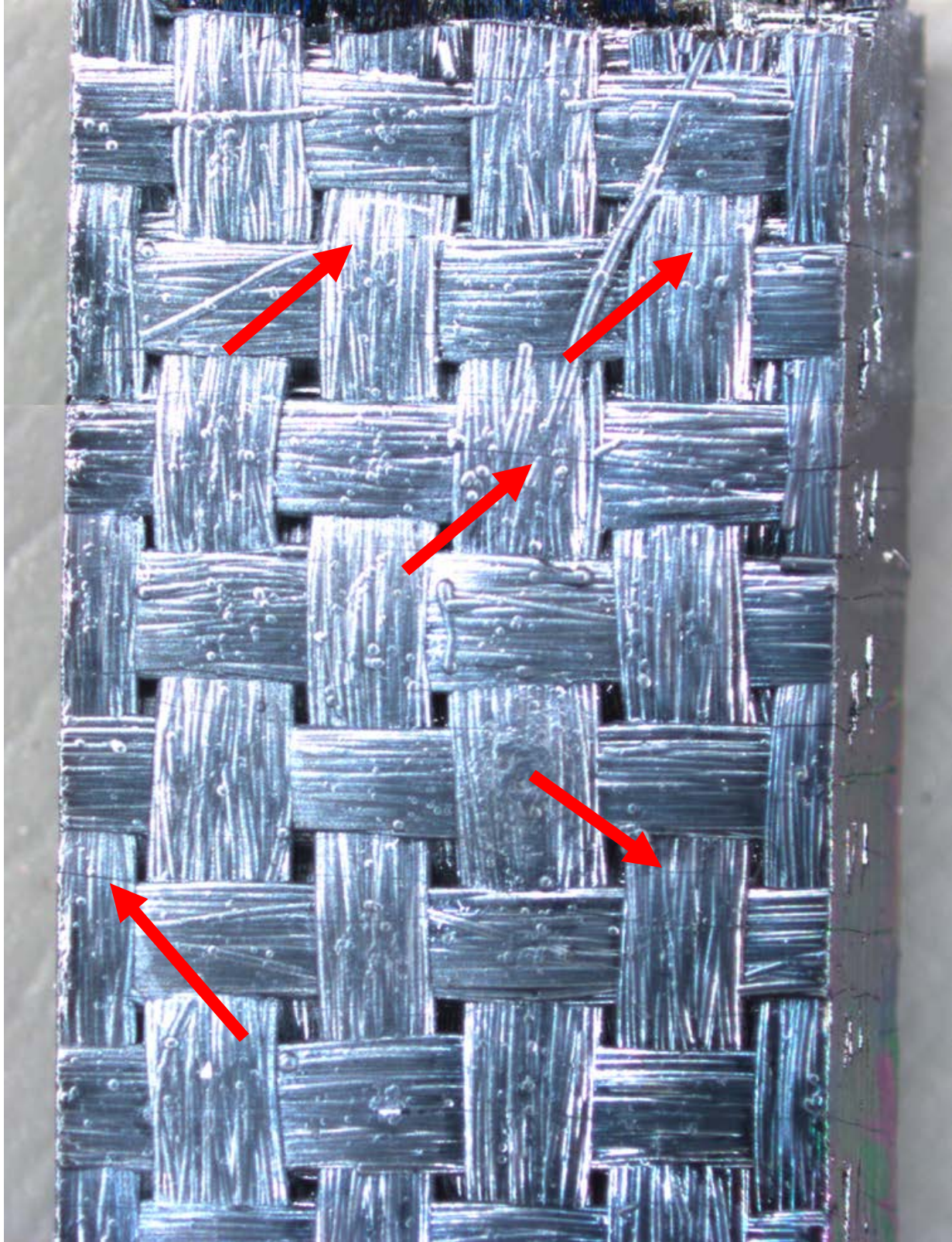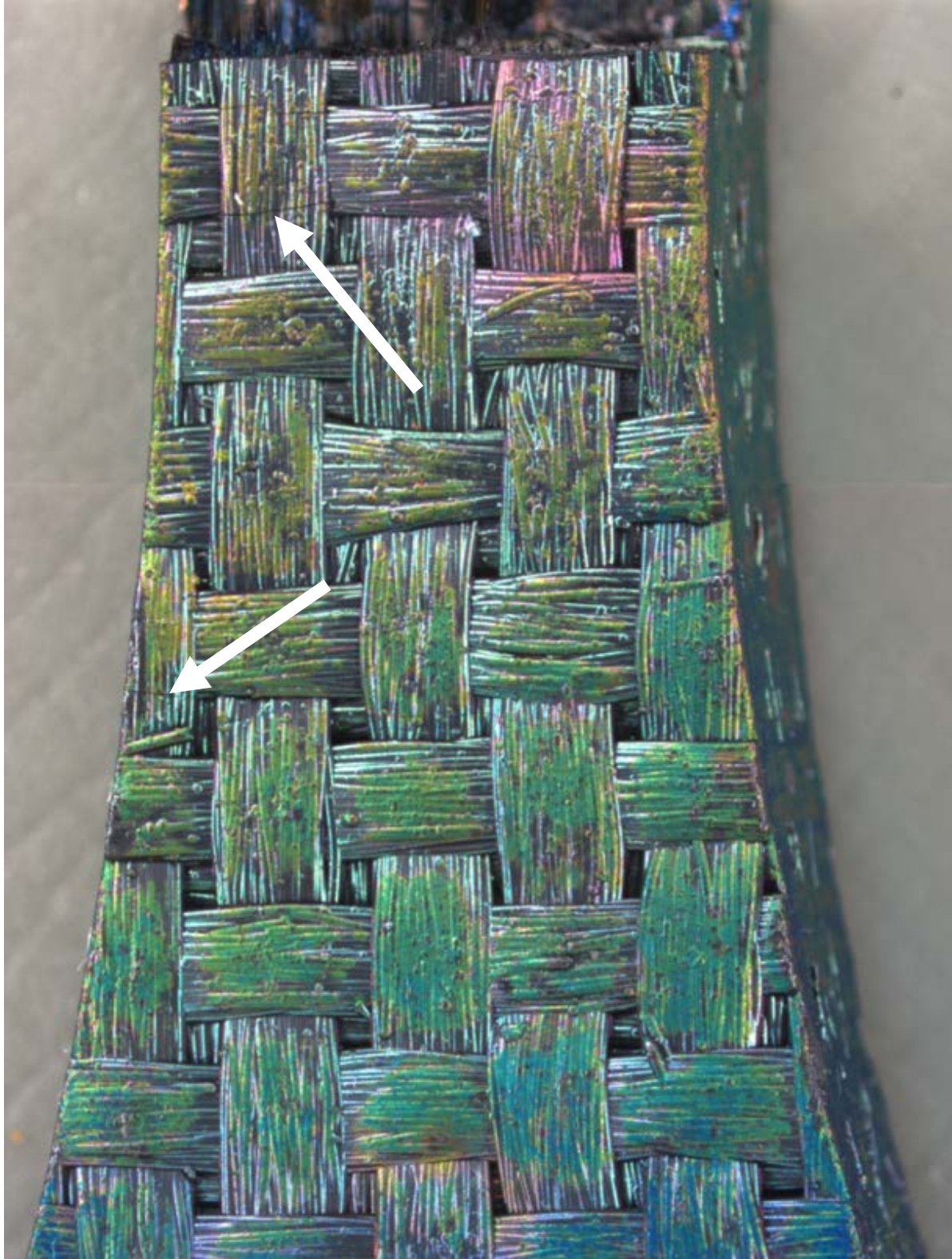
To gain insight into the effects of applied loading and test environment on composite microstructure, we examine the fracture surfaces with an SEM. The fracture surfaces of all DB-shaped specimens in this work were examined. In addition, the SEM study included the representative fracture surfaces of the HG-shaped specimens. Note that when a specimen failed the testing system was promptly shut off and the bottom half of the failed specimen was removed from the furnace. Hence, the interior of the fracture surface of the bottom half of the failed specimen was exposed to significant temperatures and prolonged oxidation for a few minutes at most. These are the fracture surfaces that were examined with the SEM.

The fracture surfaces obtained in fatigue tests performed in air with σ_{max} of 120 and 70 MPa are shown in Fig. 50 (a) and (b), respectively. The fracture surface produced in the 120 MPa fatigue test (Figure 50(a)) shows both unoxidized and oxidized regions. A relatively small *oxidized* region is seen emanating from two bottom corners of the fracture surface. The oxidized region is characterized by planar fracture without fiber pull-out as well as by oxidation of fibers and matrix. The rest of the fracture surface in Fig. 50(a) is *not oxidized*; it exhibits typical fiber pull-out and shows no apparent signs of oxidation. Recall that the specimen tested with σ_{max} of 70 MPa achieved fatigue run-out of $2x10^5$ cycles and was subsequently tested in tension to failure. The fracture surface in Fig. 50(b) exhibits virtually no signs of oxidation and is very similar to that produced in tensile test (Fig. 37). It is evident that oxidation embrittlement did not cause failure of this specimen. Recall that this specimen retained 100% of its tensile strength.

Higher magnification image in Fig. 51(a) shows evidence of oxidation found in the *oxidized* region of the fracture surface in Fig. 50(a). Oxidation of fibers and matrix are apparent as is the glassy phase covering the matrix fracture surface. Figure 51(c) shows the transition from the *oxidized* region at the corners to the *not oxidized* region in the interior of the fracture surface.

63

Figures 51 (b) and (d) show fiber pull-out, prevalent in the *not oxidized* region of the fracture surface.
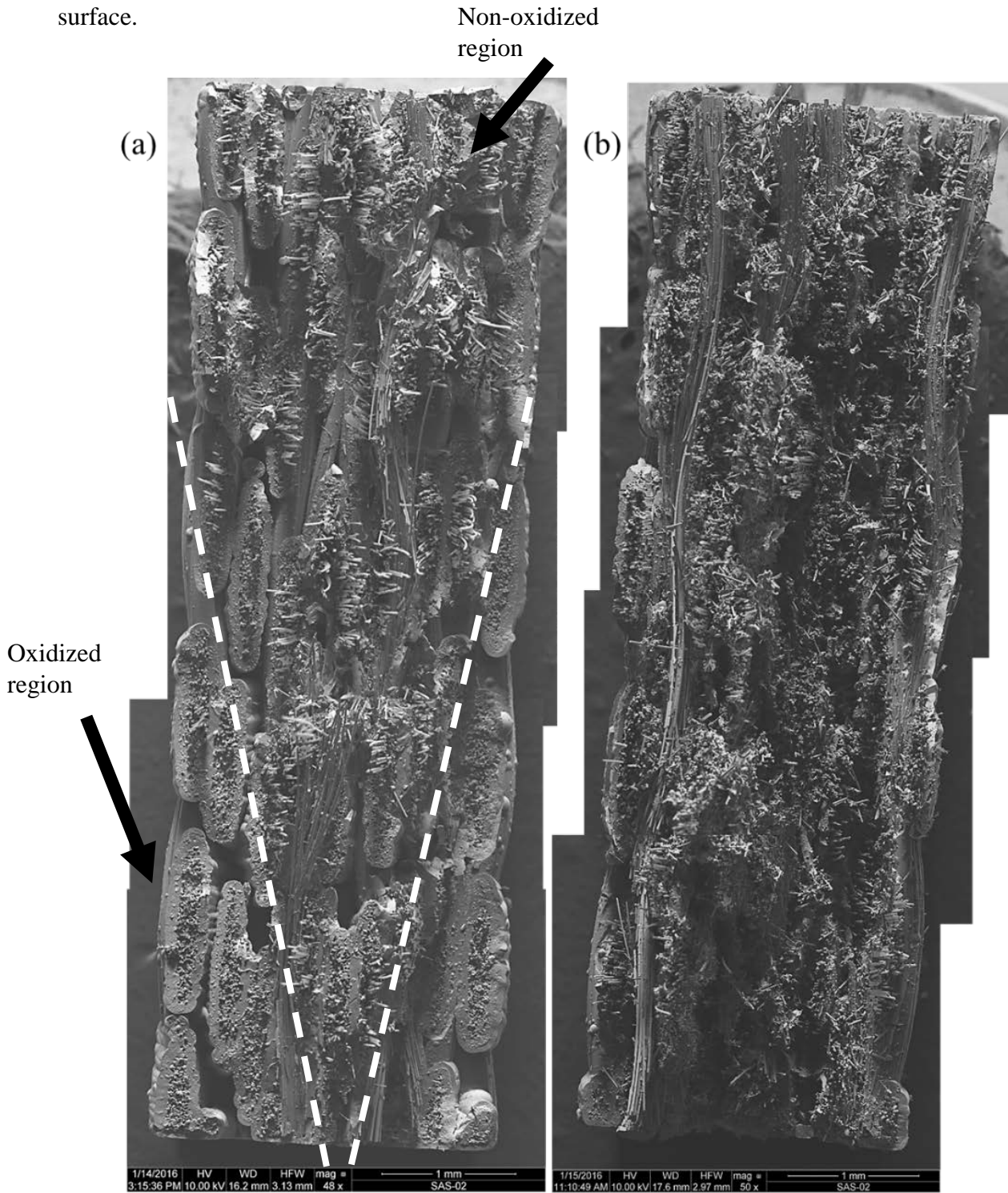
Figure 50. Fracture surface of the DB-shaped specimens tested in fatigue at 1.0 Hz at 1300°C in air. (a)σ_{max} = 120 MPa, N_f = 55,199, t_f = 15.3 h. (b)σ_{max} = 70 MPa, N_f = 200,000, t_f = 55.6 h

64
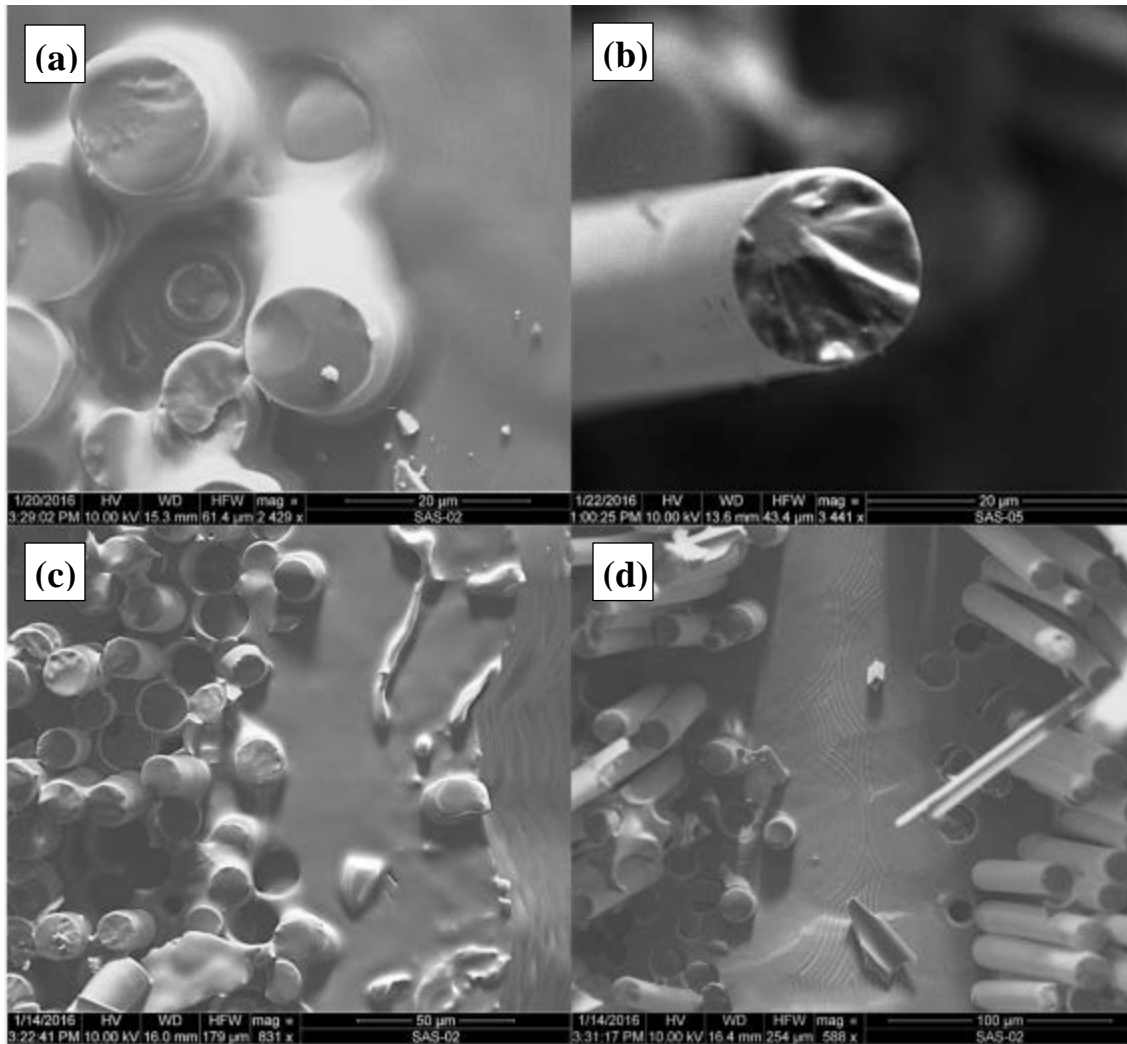
Figure 51. Fracture surface of the specimen tested in fatigue at 1.0 Hz with σ_{max} = 120 MPa at 1300°C in air, (N_f = 55,199, t_f = 15.3 h) Higher Magnification images showing: (a) glassy phase in the *oxidized* region covering matrix and fibers, (b) fiber pull-out and fracture in the *not oxidized* region, (c) *oxidized* region in the right half of the image transitioning to the *not* oxidized region in the left half of the image, and (d) fiber pull-out typical in the *not* oxidized region.

Higher magnification images of the fracture surface of the specimen achieved fatigue run-out at 70 MPa in air are shown in Figure 52. Recall that this fracture surface is predominantly *not oxidized*. The *oxidized* region, characterized by planar fracture without fiber pull-out as well as by oxidation of fibers and matrix, is minimal. The embrittlement is confined to a narrow band around the periphery of the fracture surface. The rest of the fracture surface is

not oxidized. This unembrittled region, comprising over 90% of the fracture surface, exhibits

typical fiber pull-out and shows no apparent signs of oxidation (see Figure 52).
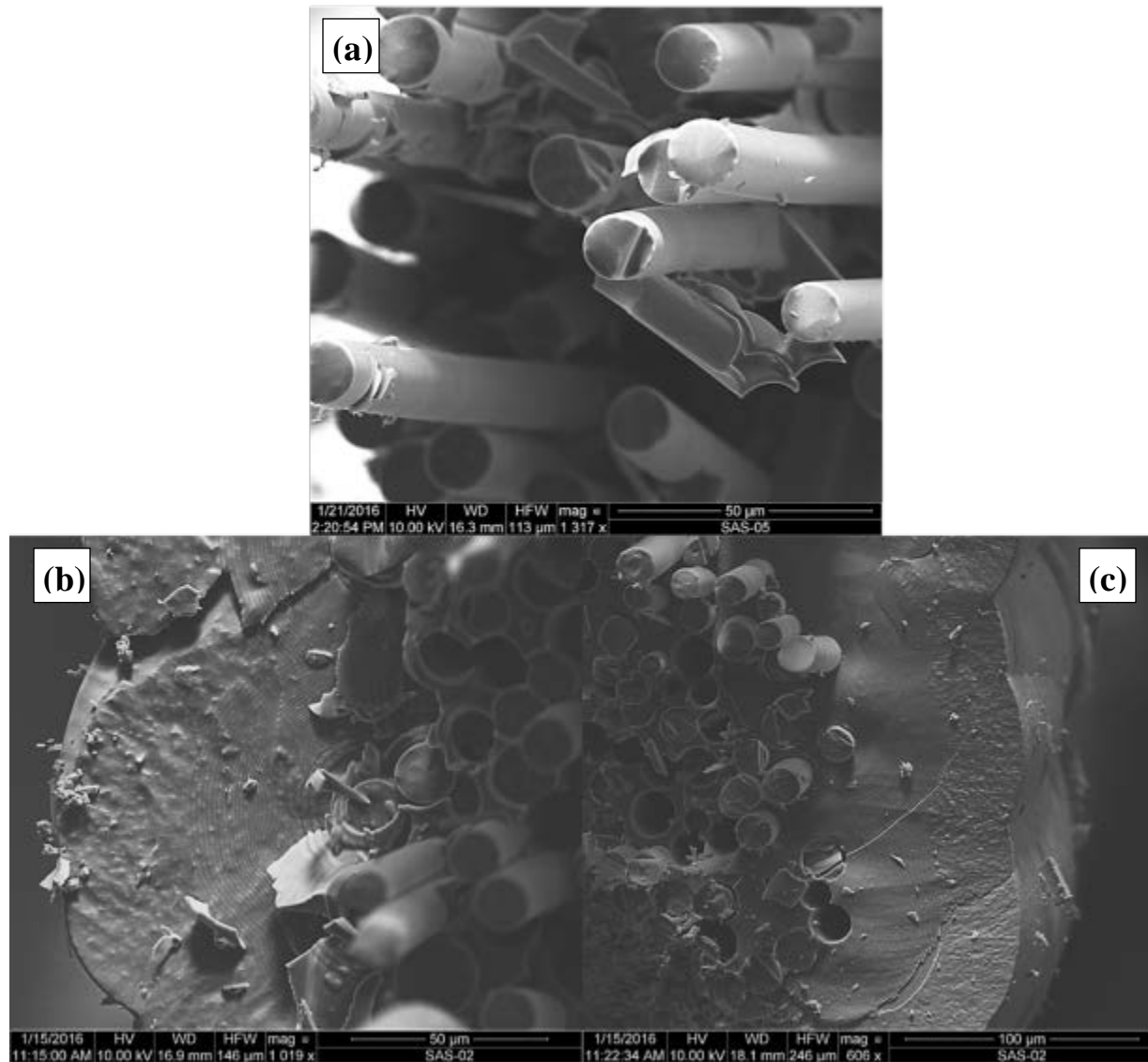
Figure 52. Fracture surface of the specimen tested in fatigue at 1.0 Hz with σ_{max} = 70 MPa at 1300°C in air, (N_f = 200,000, t_f = 55.6 h). Over 90% of the fracture surface remains unembrittled exhibiting typical fiber pull-out and no apparent signs of oxidation.

Note that only the SEM micrographs of the representative fracture surfaces obtained at 1300°C in air are shown in Figures 50-52. The micrographs of other fracture surfaces of the DB-shaped specimens produced at 1300°C in air are provided in Appendix B.

The SEM micrographs of the representative fracture surfaces of the DB-shaped specimens obtained at 1300°C in steam are shown in Figure 53. Both fracture surfaces in Figure 53 exhibit considerable signs of oxidation. Unlike in the case of the specimen that achieved fatigue runout in air, fracture surface of the specimen that achieved run-out in steam has a sizable oxidized region (Figure 53 (b)). Recall that the specimen tested in air retained 100% of its tensile strength while the specimen tested in steam retained only 51% of its tensile strength. Such low retention of the tensile strength is attributed to significant embrittlement. Now consider the fracture surface produced in the 140 MPa fatigue test in steam (Figure 53 (a)). A large portion of this fracture surface is oxidized, suggesting that an oxidation-assisted unbridged crack has formed prior to the ultimate failure of the composite.

Non-oxidized region

Oxidized region
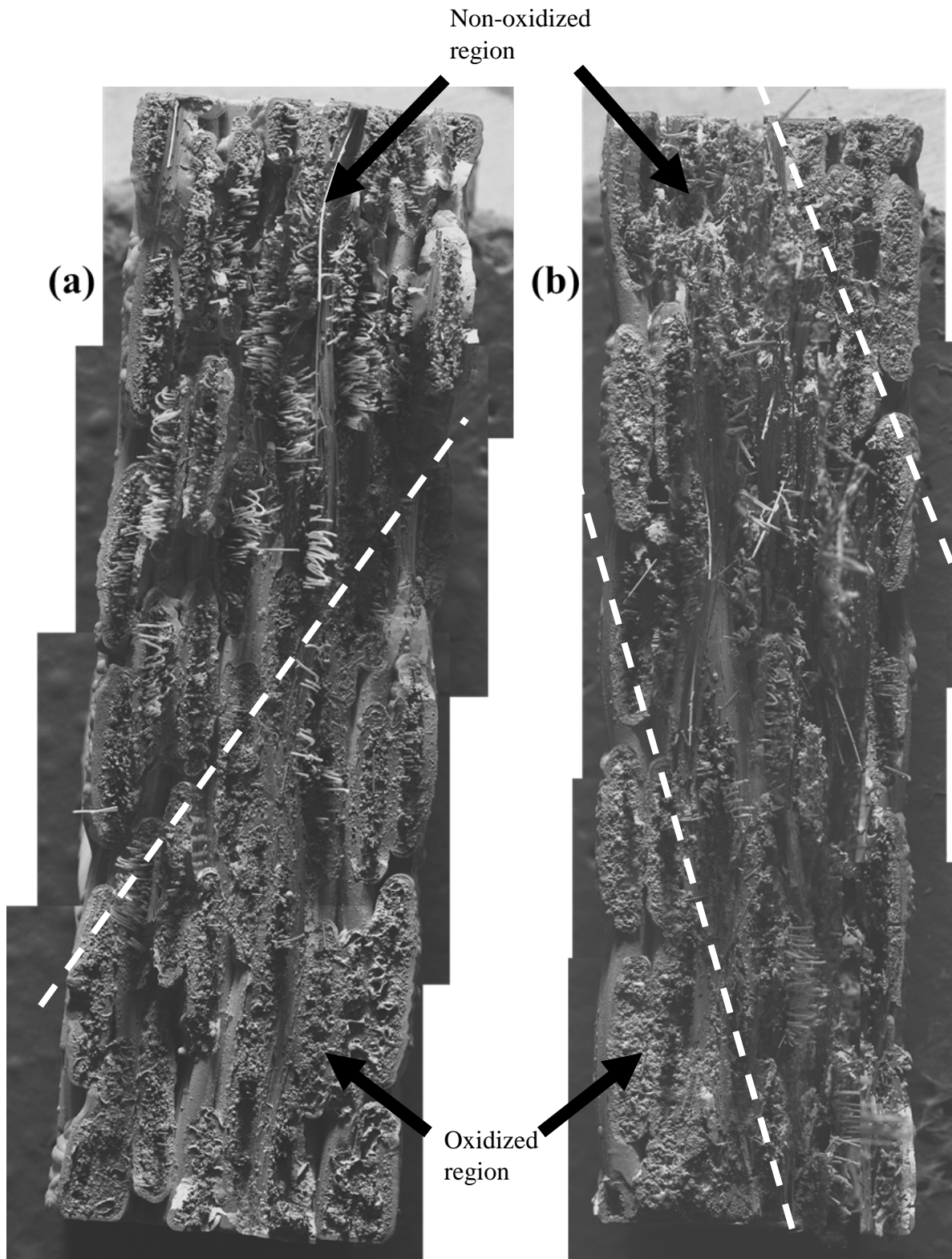
Figure 53. Fracture surface of the DB-shaped specimens tested in fatigue at 1.0 Hz at 1300°C in steam. (a) σ_{max} = 140 MPa, N_f = 72,074, t_f = 20.0 h. (b) σ_{max} = 100 MPa, N_f = 200,000, t_f = 55.6 h

Higher magnification images of the fracture surface produced in the 120 MPa fatigue test in steam are shown in Figure 54. Oxidation of fibers and matrix as well as the glassy phase covering the fracture surface in the oxidized region are evident. Transition from the *oxidized* region to the *not oxidized* region in the interior of the fracture surface is also seen. Note the bubbles in the glassy layer covering the fracture surface in Figure 54b. We postulate that at 1300°C in steam the oxidation of the B_4C layers and formation of boria glass is followed by the oxidation of the SiC matrix layers, thus resulting in the formation of the borosilicate glass during the test. Bubbles seen in Fig. 54b are most likely the gaseous reaction products diffusing through the borosilicate glass. Recall that the borosilicate glass has a higher viscosity than boria, thereby making it more difficult for the gaseous reaction products to escape. At 1300°C in steam, the viscosity of the SiO_2 layer decreases [14], allowing the gaseous reaction products to escape. Also note the "craters" in the fracture surface (Figs. 54 (b) and (d)), which are left in the SiO_2 glassy layer by escaping gases believed to be boron-containing complexes. Figure 55 below shows some of the major features of the specimen M12 that achieved run-out in steam at 1300°C with a maximum stress of 100 MPa.
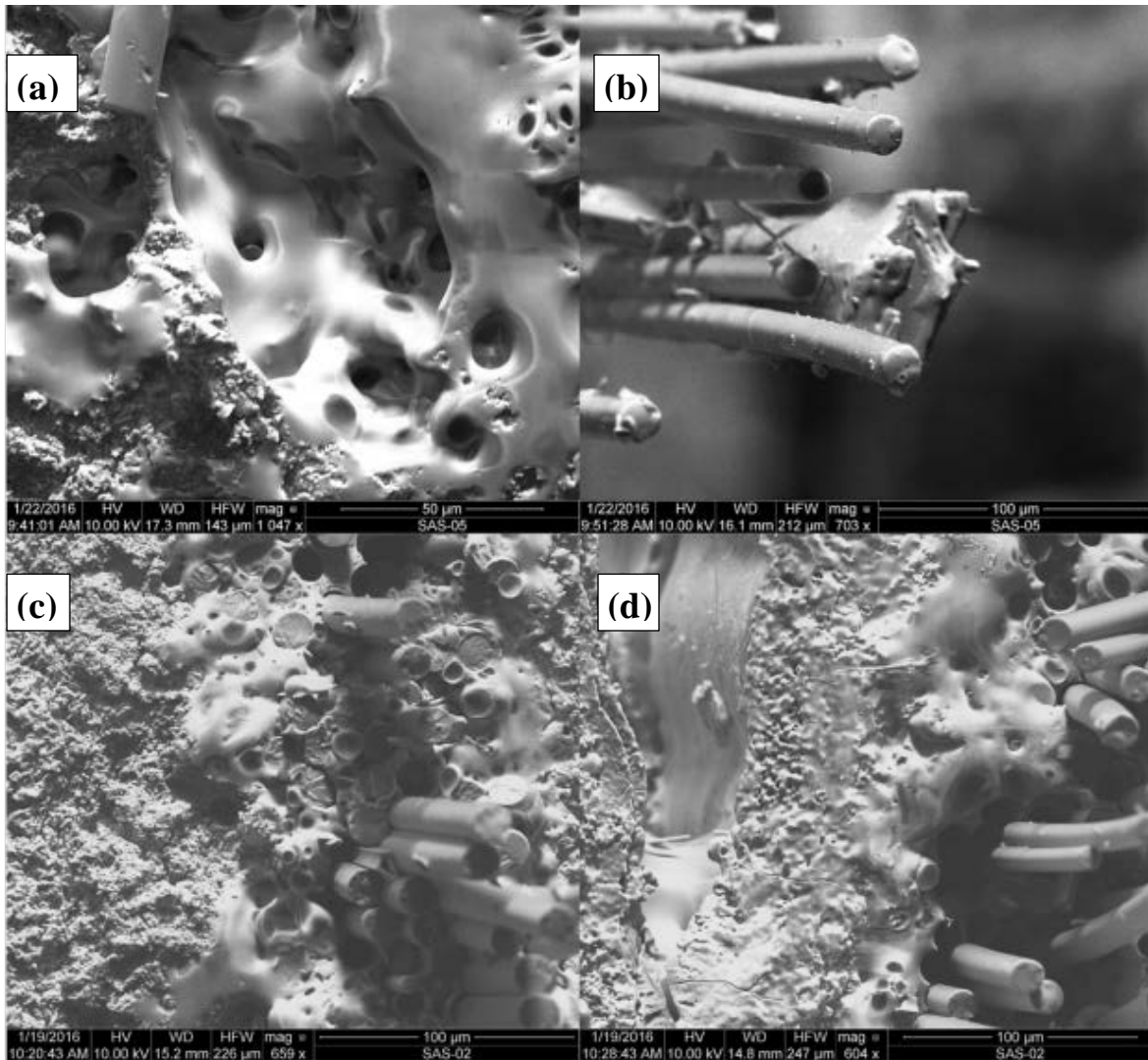
69
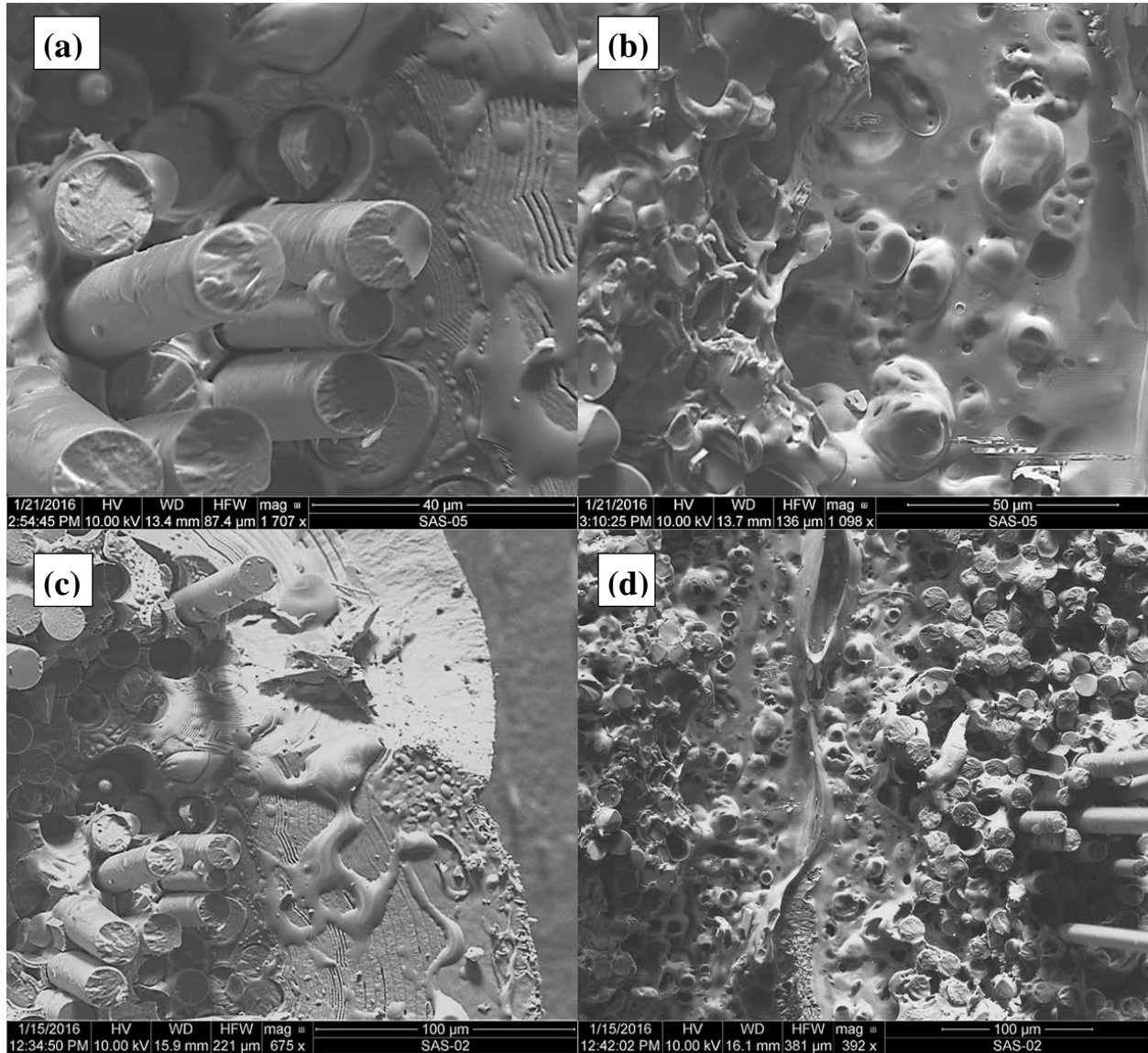
Figure 54. Fracture surface of the specimen tested in fatigue at 1.0 Hz with σ_{max} = 140 MPa at 1300°C in steam, (N_f = 72,074, t_f = 20.0 h). Higher magnification images showing: (a) and (c) transition from the *oxidized* region in the right half of the image to not oxidized region in the left half of the image, (b) and (d) glassy phase in the *oxidized* region covering matrix and fibers.

Higher magnification images of the fracture surface of the specimen that achieved fatigue run-out with a maximum stress of 100 MPa at 1300°C in steam are presented in Figure 55. The key features of the oxidized regions seen in Figure 55 are similar to those observed in the

70

fracture surface in Figure 54. Note the bubbles and craters in the glassy layer covering the
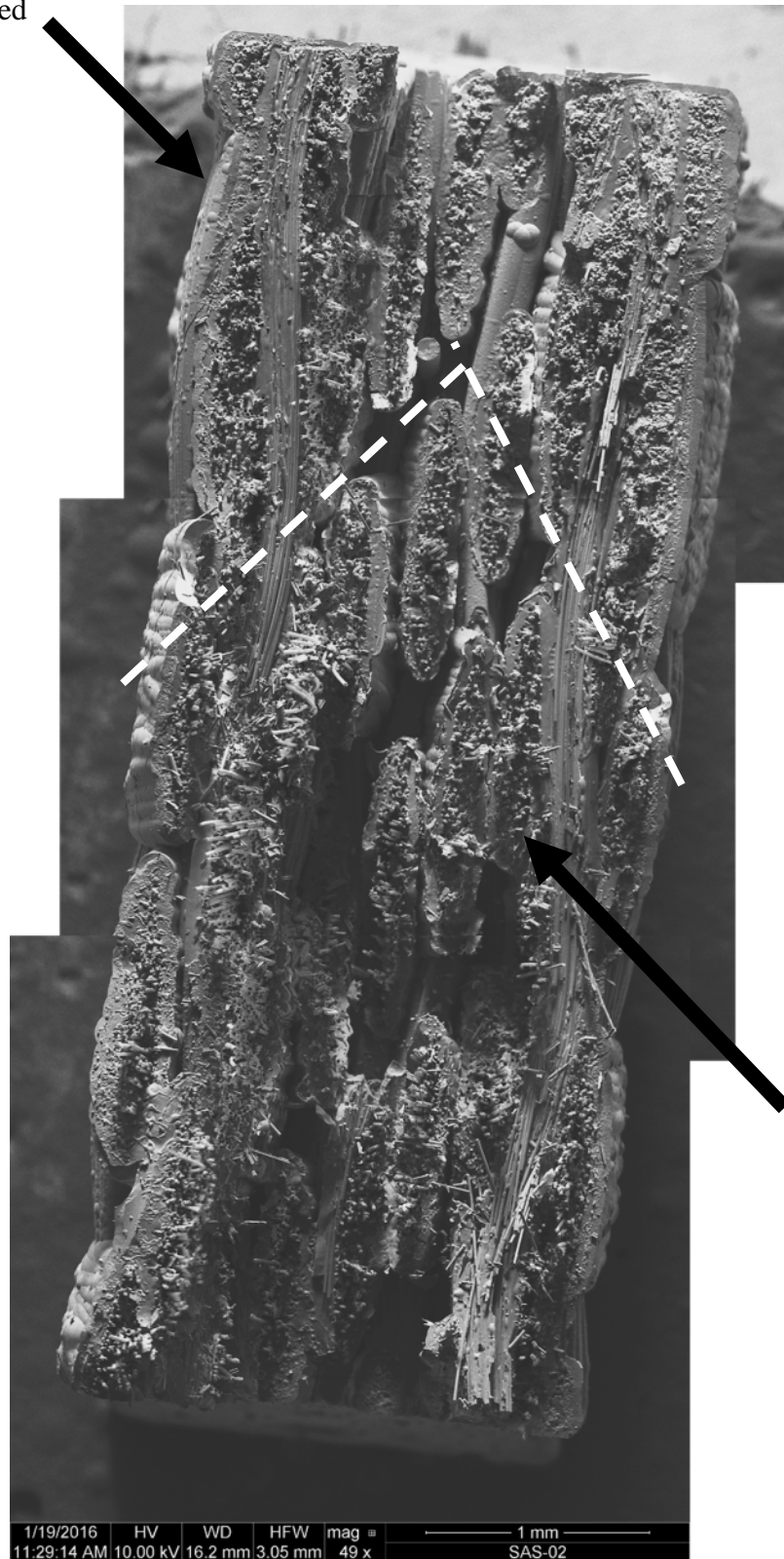
fracture surface in the oxidized region.

Figure 55. Fracture surface of the DB- shaped specimen tested in fatigue at 1.0 Hz with σ_{max} = 100 MPa at 1300°C in steam (N_f = 200,000, t_f = 55.6 h). Higher magnification images showing: (a) glassy phase in the *oxidized* region covering matrix and fibers, (b) oxidation of the fracture surfaces of the pulled-out fibers, (c) and (d) oxidized region occupying most of the image.

The representative fracture surfaces obtained for the HG-shaped specimens tested in air

and in steam are presented in Figure 56 and Figure 57, respectively. The fracture surfaces in

Figs. 56 and 57 exhibit distinctive signs of oxidation, although the oxidized regions are relatively

small. It is noteworthy that the fracture surfaces of the HG-shaped specimen tested in fatigue in air (Figure 56) is similar to that of the DB-shaped specimen subjected to fatigue in air (Figure 50a). Likewise, the fracture surfaces of the HG-shaped specimen (Figure 57) and of the DB-shaped specimen (Figure 53 (a)) tested in fatigue in steam exhibit similar morphology. The morphology of the fracture surface is influenced by test environment and test duration, but is little affected by specimen geometry. Higher magnification images showing different features of the fracture surfaces of the HG-shaped specimens tested in fatigue in air and in steam are provided for Figure 58 and Figure 59, respectively. We note once more that the typical features seen in the fracture surface of the HG-shaped specimen tested in air (Figure 58) are similar to those seen in the fracture surface of the DB-shaped specimen tested in air (Figure 53). Likewise the higher magnification images of the fracture surface of the HG-shaped specimen tested in steam (Figure 59) display features similar to those seen in the fracture surface of the DB-shaped specimen tested in stem (Figure 54). While all the specimens that failed in fatigue had similar fracture surfaces, the slightly increased fatigue life of the specimens in steam is supported by the presence of large oxidized regions along the fracture surface. This glassy phase would have been generated along propagating cracks sealing the interior of the specimen from further oxidation.

Additional SEM micrographs for all specimens examined in this work are provided in Appendix B.
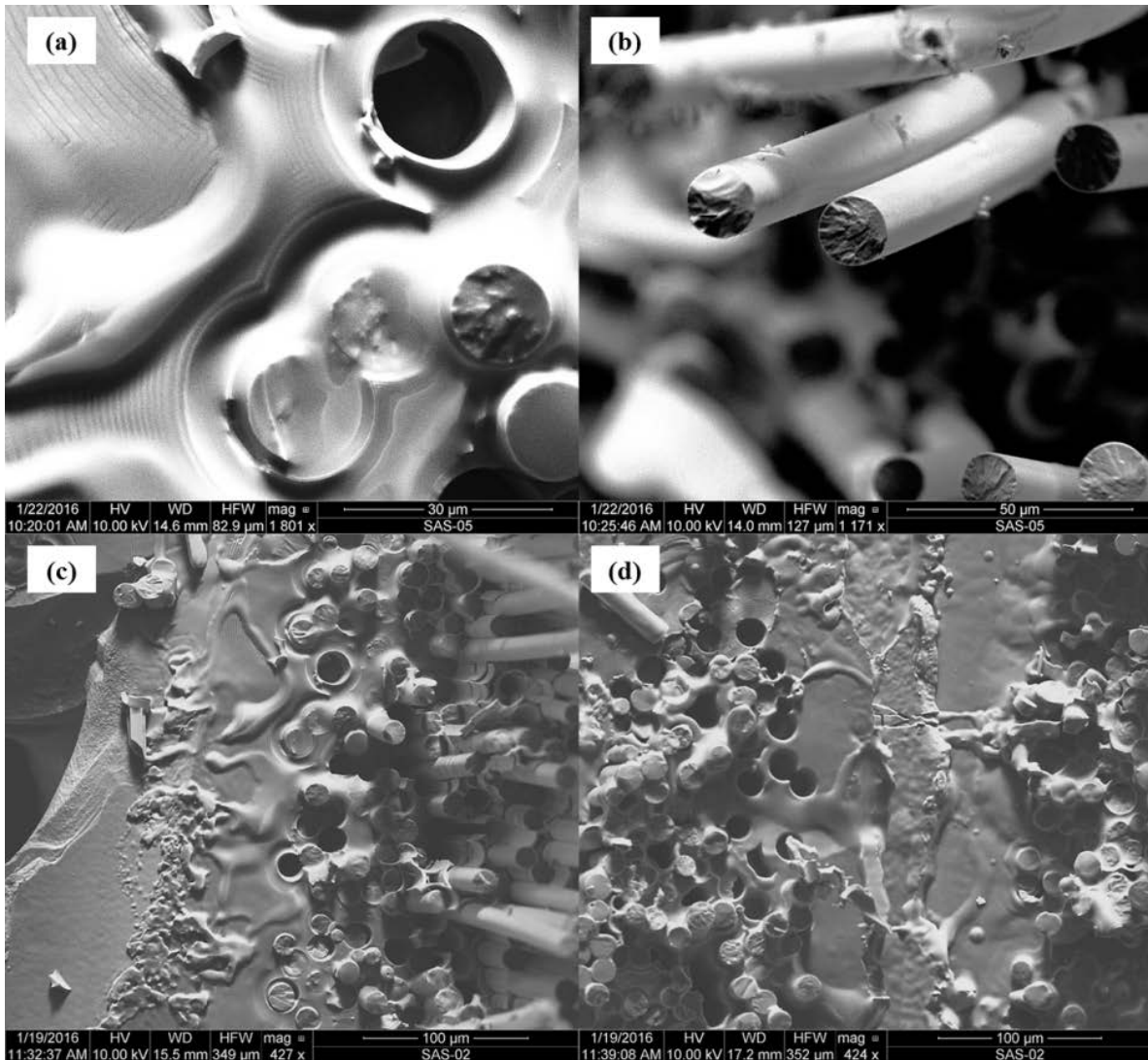
Oxidized region

Non-oxidized region

Figure 56. Fracture surface of the HG-shaped specimens tested in fatigue at 1.0 Hz at 1300°C in air, σ_{max} = 145 MPa, N_f = 68,831, t_f = 19.1 h.
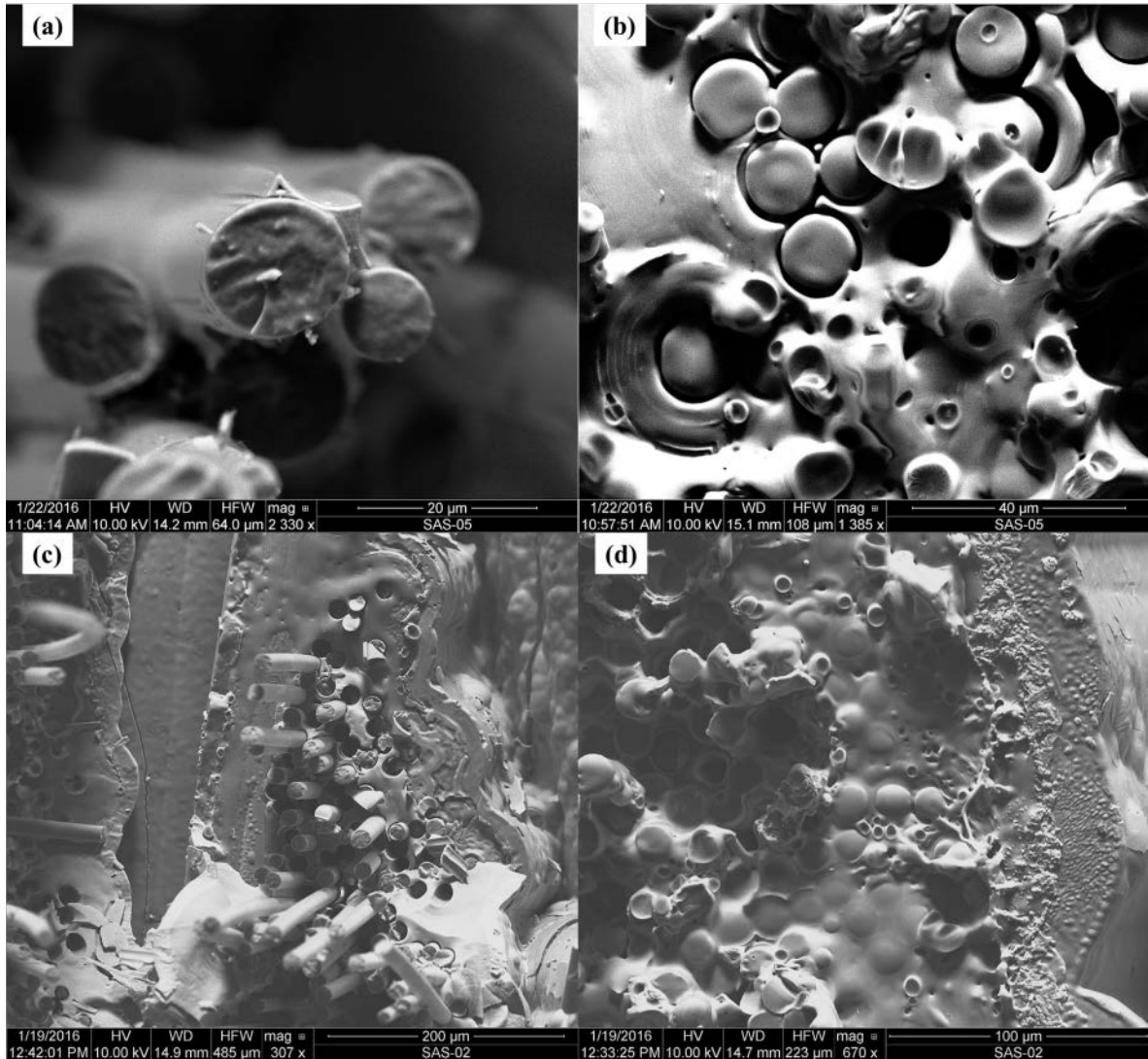
Oxidized region

Non-oxidized region

Figure 57. Fracture surface of the HG-shaped specimens tested in fatigue at 1.0 Hz at 1300°C in steam. σ_{max} = 150 MPa, N_f = 13,266, t_f = 3.7 h.

Figure 58. Fracture surface of the HG-shaped specimen tested in fatigue at 1.0 Hz with σ_{max} = 145 MPa at 1300°C in air, (N_f = 68,831, t_f = 19.1 h). Higher magnification images showing (a) glassy phase of in the *oxidized* region covering matrix and fibers, (b) pulled-out fibers, (c) and (d) *oxidized* region occupying most of the image.

Figure 59. Fracture surface of the HG-shaped specimen tested in fatigue at 1.0 Hz with σ_{max} = 150 MPa at 1300°C in steam, (N_f = 13,266, t_f = 3.7 h). Higher magnification images showing (a) fiber fracture surfaces, (b) glassy phase in the *oxidized* region covering matrix and fibers, (c) fiber pull-out in the non-oxidized region, and (d) planar fracture surface morphology in the oxidized region.

76

VI. Conclusions and Recommendation

6.1 Conclusions

The tensile stress-strain behavior of the Hi-Nicalon™/SiC-B$_4$C composite was investigated and the tensile properties measured at 1300°C. The UTS was 311 MPa, the elastic modulus, 180 GPa, and the failure strain, 0.57 %. The proportional limit was 117 MPa (~38 %UTS).

Tension-tension fatigue behavior of the Hi-Nicalon™/SiC-B$_4$C composite was studied at the loading frequency of 1.0 Hz at 1300°C in air and in steam. Fatigue stress levels ranged from 70 to 160 MPa. The fatigue run-out was achieved at 70 MPa (~23 %UTS) in air and at 100 MPa (~32%UTS) in steam for DB-shaped specimens. Presence of steam has only slight beneficial effect on the fatigue performance at this temperature. The fatigue run-out was achieved at 80 MPa (~26 %UTS) in air and at 100 MPa (~32%UTS) in steam for HG-shaped specimens. The HG-shaped specimens had a slightly higher fatigue life at 1300°C in air than the DB-shaped specimens. Notably the composite exhibited more strain ratcheting during fatigue at 1300°C than what was reported at 1200°C by Delapasse [10]. Hence, higher strains were accumulated in fatigue tests at 1300°C than at 1200°C. However, the increase in temperature from 1200 to 1300°C did not significantly affect the reduction in stiffness with increasing fatigue cycles.

Prior fatigue in air had no effect on the retained tensile strength or the retained stiffness of the composite, suggesting that no damage occurred to the fibers. In contrast, prior fatigue in steam caused significant reduction in tensile strength. Prior fatigue in steam reduced the tensile strength by 41-51% and the stiffness, by 36%. In steam, degradation in composite tensile strength is caused by fiber degradation. Yet, as pointed out in prior work [10], fiber degradation

is not caused by oxidation, but is most likely due to an intrinsic creep-controlled flaw growth mechanism.

Optical micrographs of the tested specimens revealed the presence of transverse cracks of some 0° fiber bundles on the specimen surface. These cracks become more plentiful and more pronounced as the maximum stress level increases. In the case of the DB-shaped specimens, such transverse cracks are more prevalent in the specimens tested in air. The DB-shaped specimens tested in steam and HG-shaped specimens tested in both environments showed very few if any transverse cracks on the specimen surface. For the DB-shaped specimens these transverse cracks are present throughout the gage section. The transverse cracks that were present on the HG-shaped specimens were localized near the fracture surface. The specimens tested in tension to failure test showed no transverse cracks. The SEM examination of the fracture surfaces revealed that the degree of oxidation of the specimens that failed in fatigue increased with increasing test duration. The fracture surfaces produced in tension tests to failure showed little to no oxidation. The fracture surfaces produced in fatigue tests of shorter duration had small oxidized regions around the perimeter of the fracture surface with the interior of the fracture surface remaining largely unoxidized. The fracture surfaces obtained in fatigue tests of longer duration exhibited larger oxidized regions. We note that the oxidation progressed more aggressively at 1300°C than at 1200°C.

6.2 Recommendations

In order to provide better confidence in the data collected in this research, more samples should be tested at each of the stress levels in each environment. Investigation of this material should be performed at lower temperatures to provide a full understanding of material behavior.
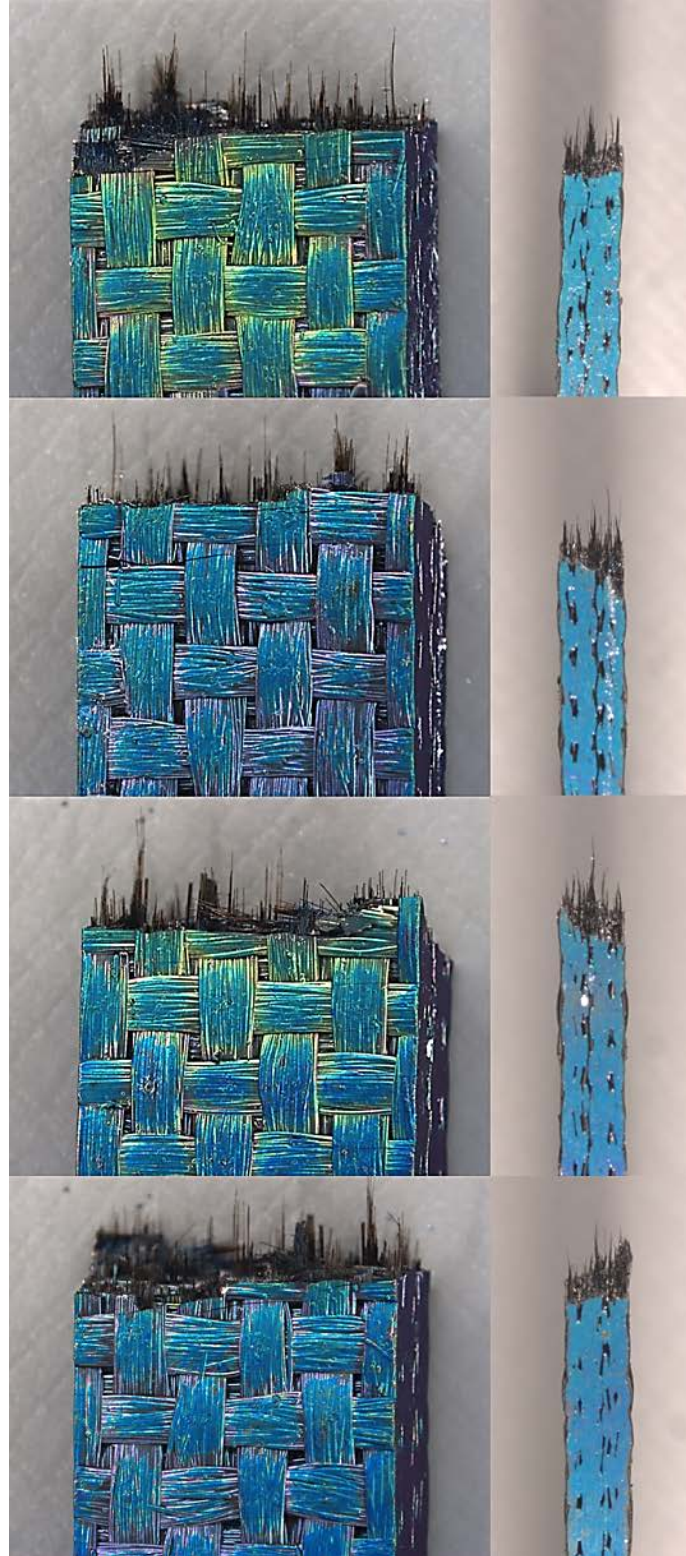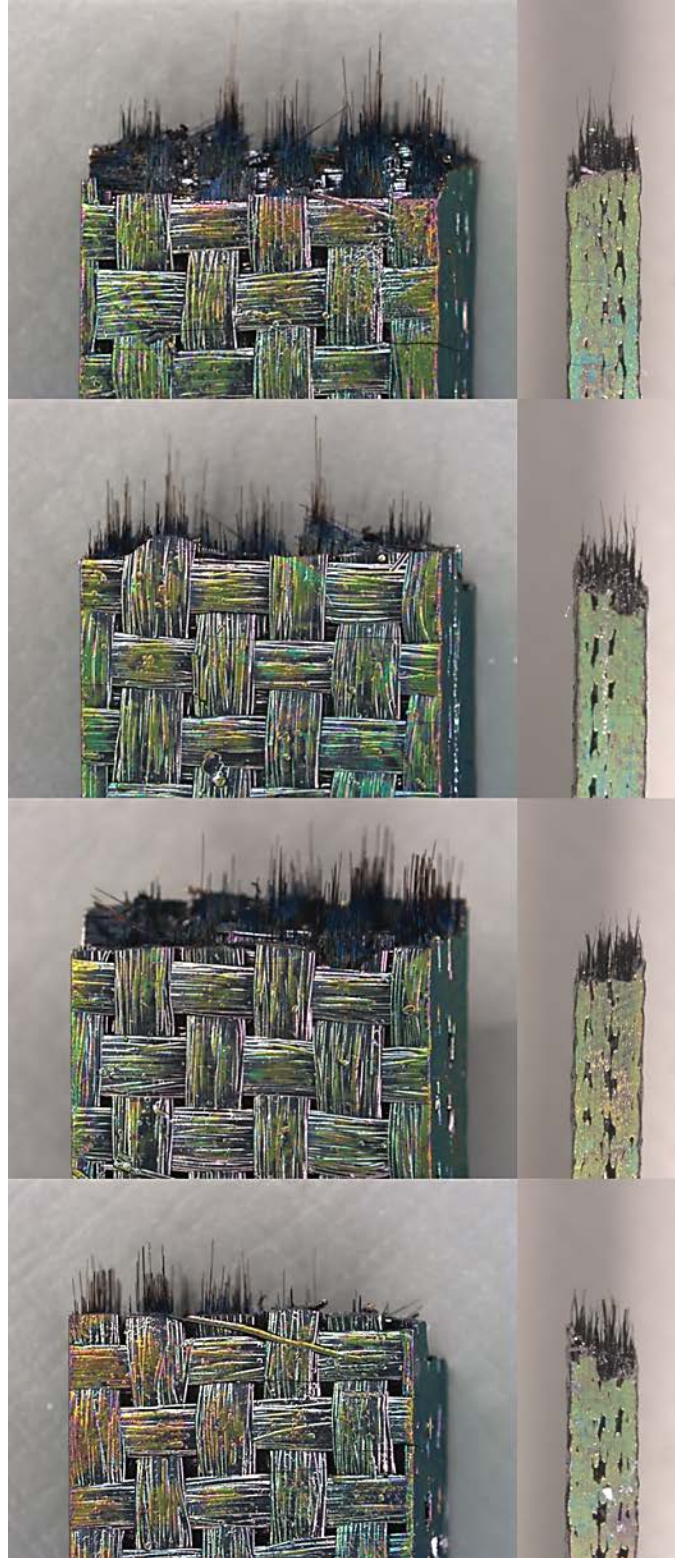
Appendix A

Figure 60: Fracture surface of the specimen tested in tension to failure at 1300 °C in air, 0.05 mm/s.
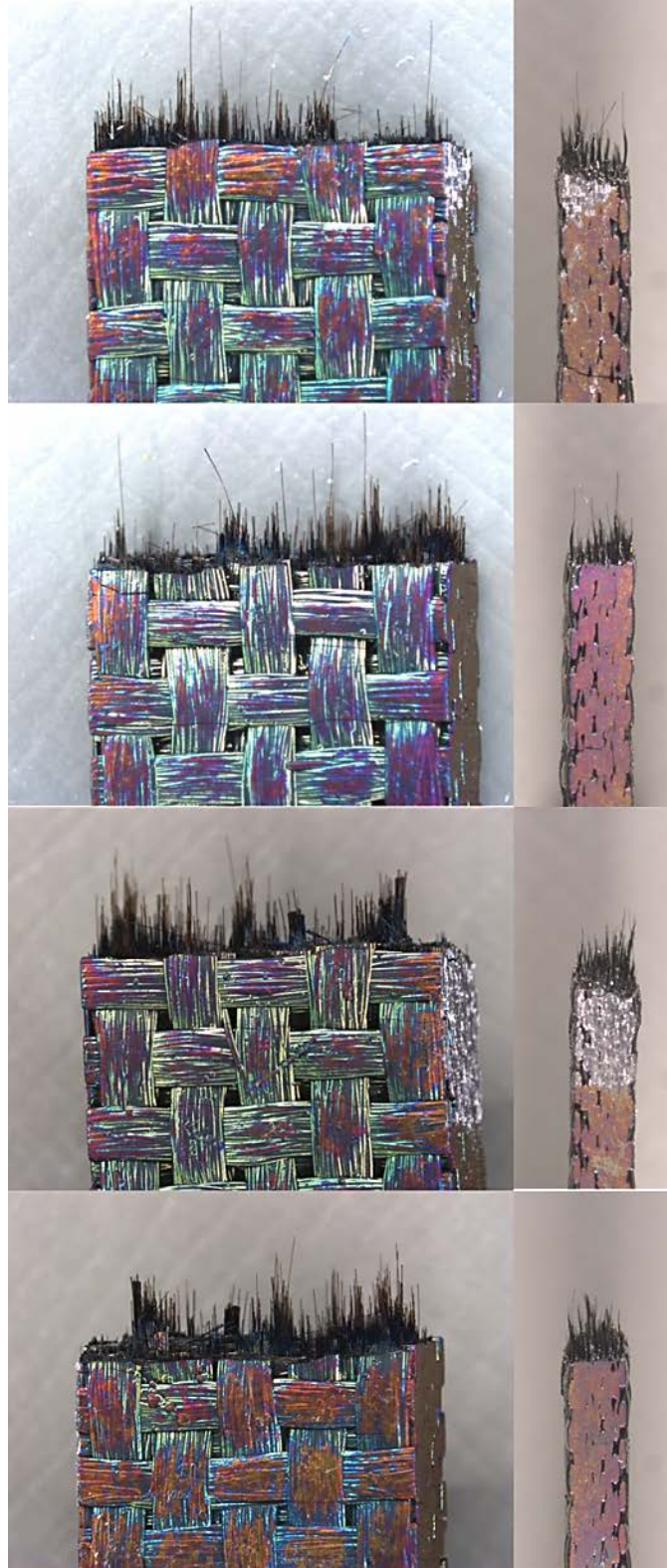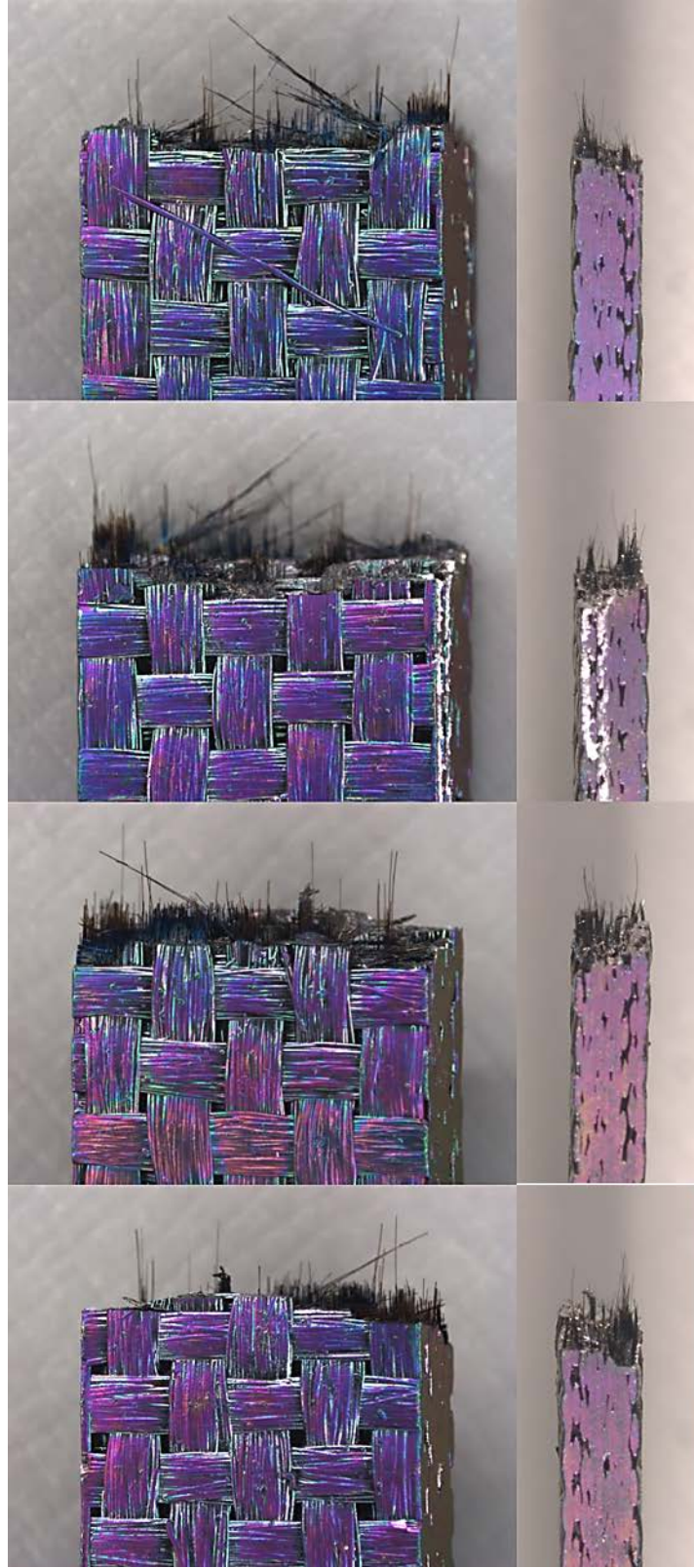
Figure 61: Fracture surface of the DB-shaped specimen tested in fatigue at 1300°C in air, σ_{max} = 140 MPa, N_f = 20,069, t_f = 5.6h
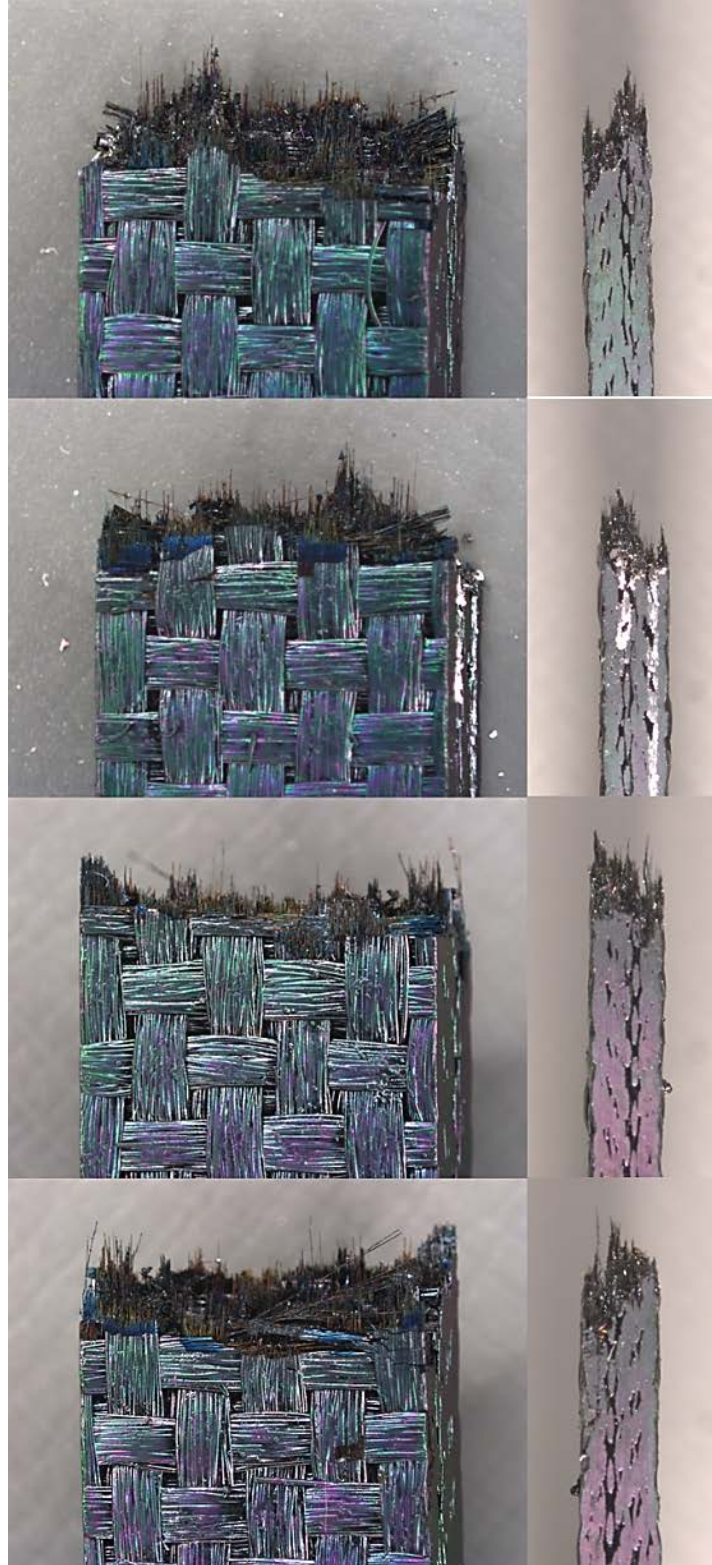
Figure 62: Fracture surface of the DB-shaped specimen tested in fatigue at 1300°C in air, $\sigma_{max} = 130$ MPa, $N_f = 38,828$, $t_f = 10.8h$
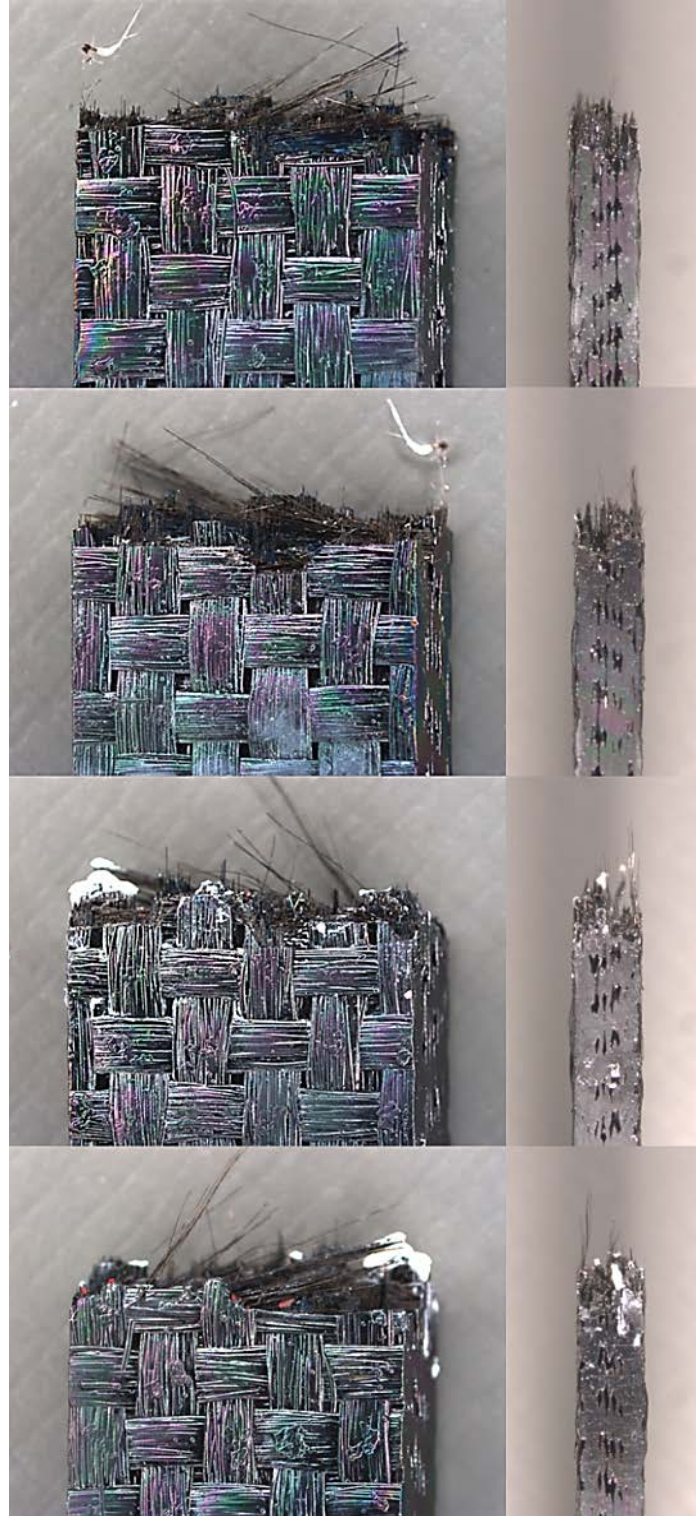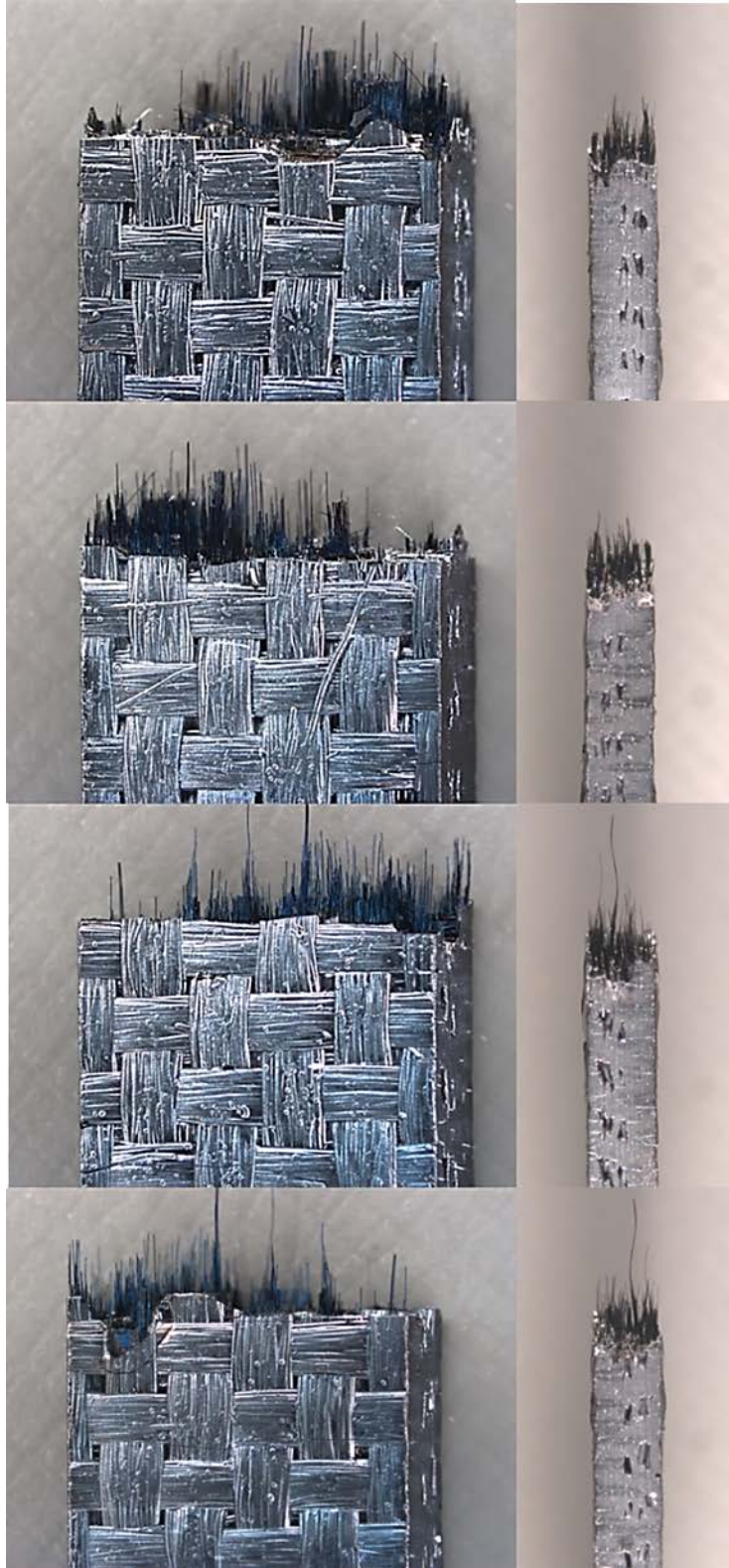
Figure 63: Fracture surface of the DB-shaped specimen tested in fatigue at 1300°C in air, σ_{max} = 120 MPa, N_f = 55,199, t_f = 15.3h

Figure 64: Fracture surface of the DB-shaped specimen tested in fatigue at 1300°C in air, σ_{max} = 100 MPa, N_f = 84,855, t_f = 23.6h

Figure 65: Fracture surface of the DB-shaped specimen tested in fatigue at 1300°C in air, σ_{max} = 70 MPa, N_f = 200,000, t_f = 55.6h
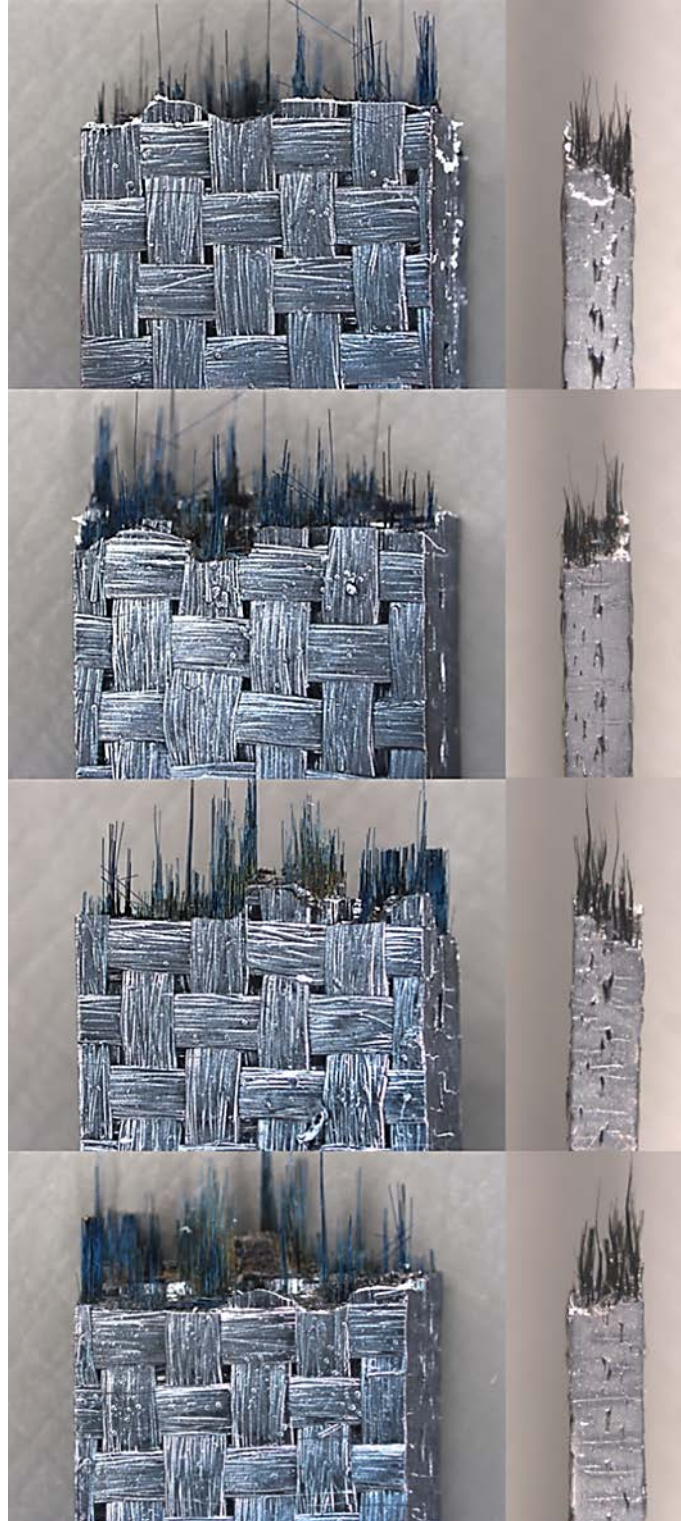
Figure 66: Fracture surface of the DB-shaped specimen tested in fatigue at 1300°C in steam, σ_{max} = 160 MPa, N_f = 17,811, t_f = 4.9 h
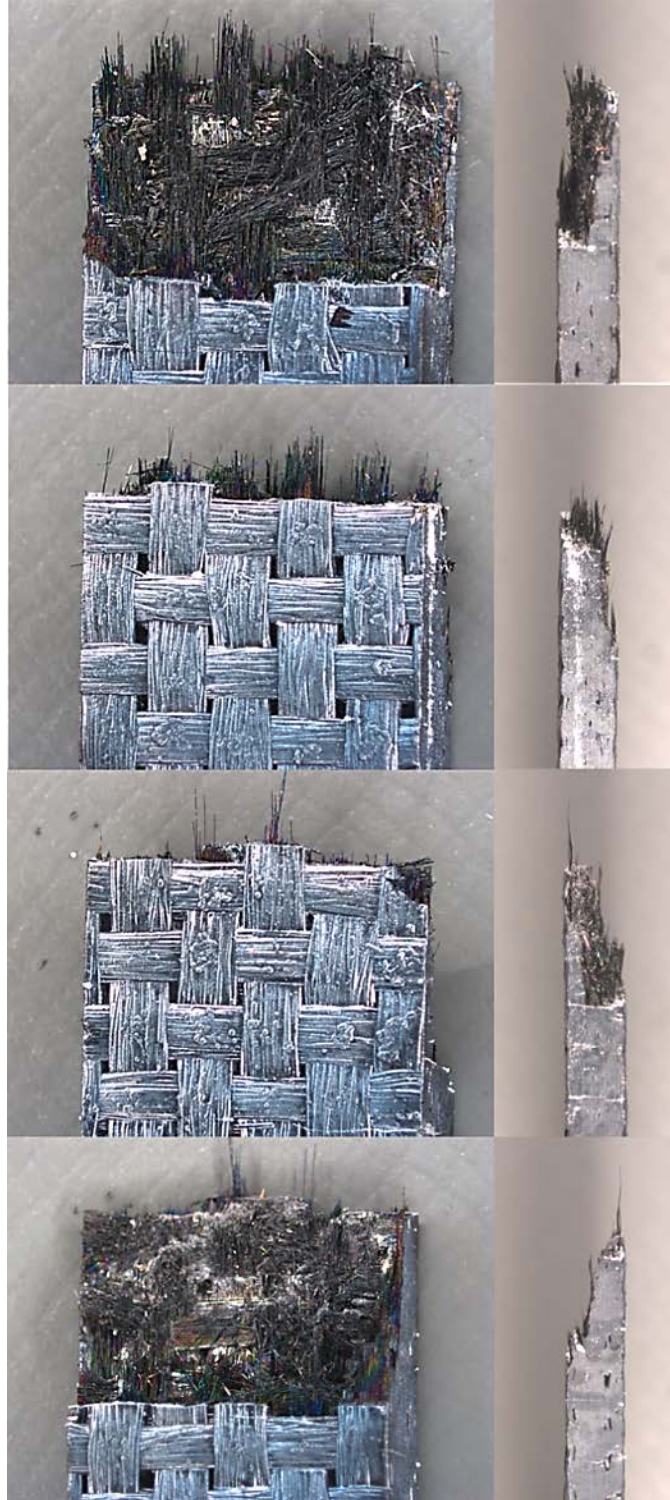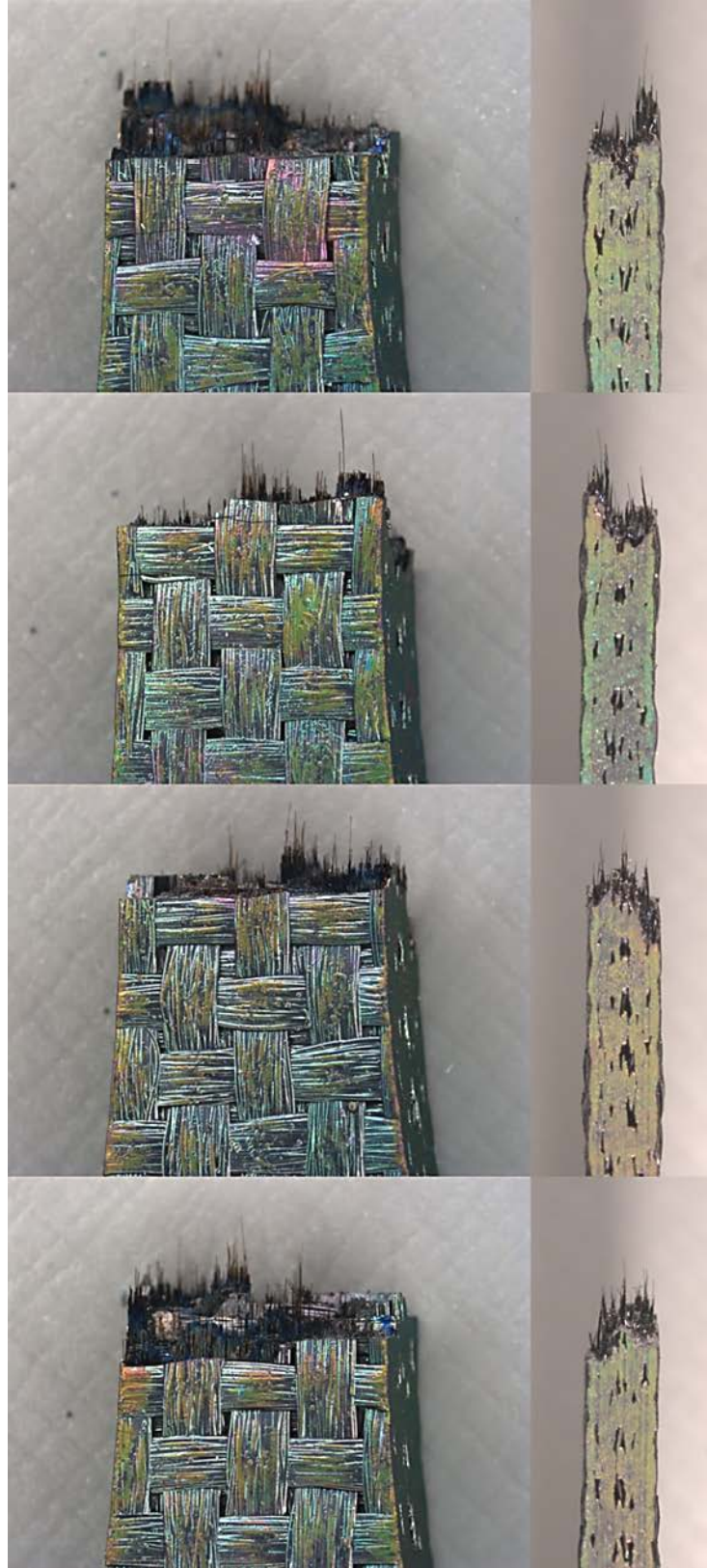
Figure 67: Fracture surface of the DB-shaped specimen tested in fatigue at 1300°C in steam, σ_{max} = 140 MPa, N_f = 72,074, t_f = 20.0 h
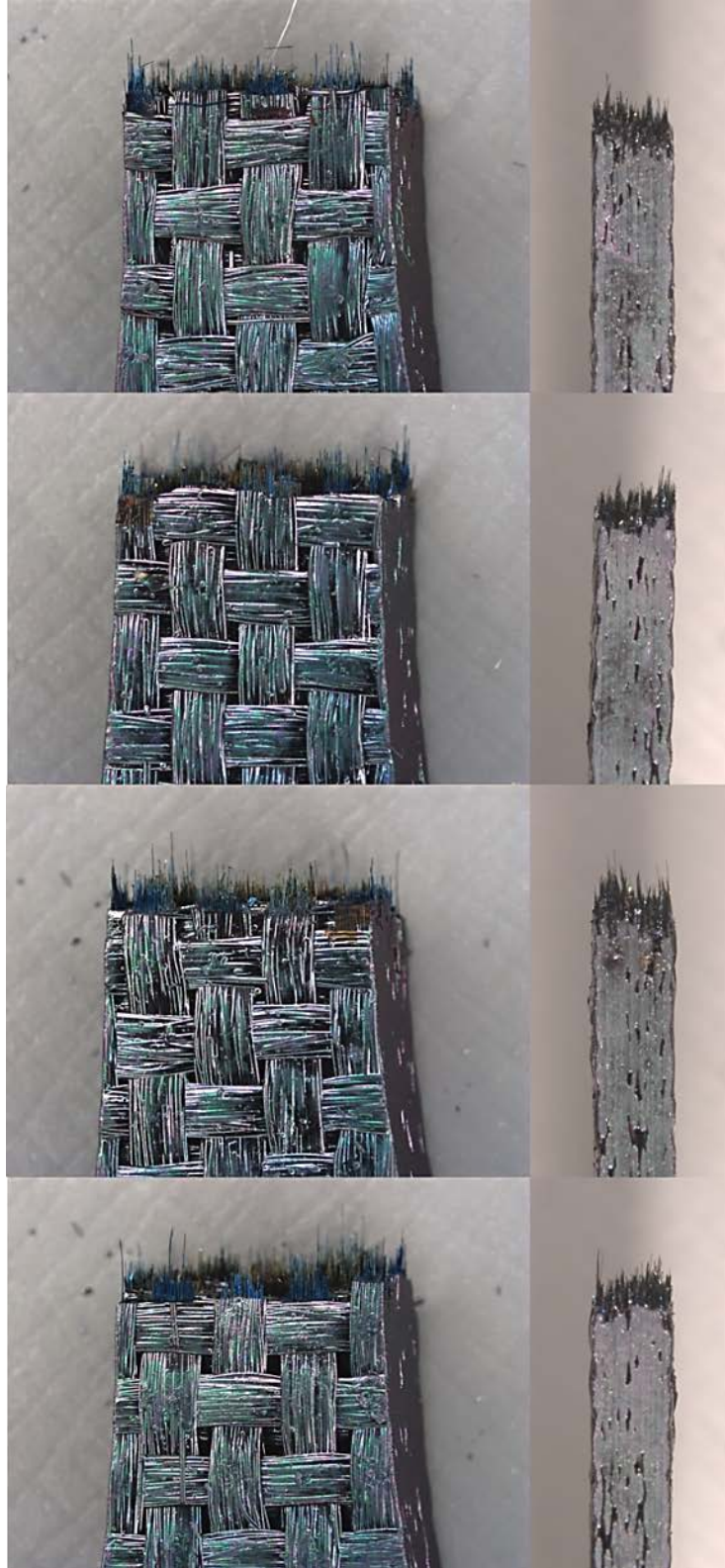
Figure 68: Fracture surface of the DB-shaped specimen tested in fatigue at 1300°C in steam, σ_{max} = 120 MPa, N_f = 93,016, t_f = 25.8 h
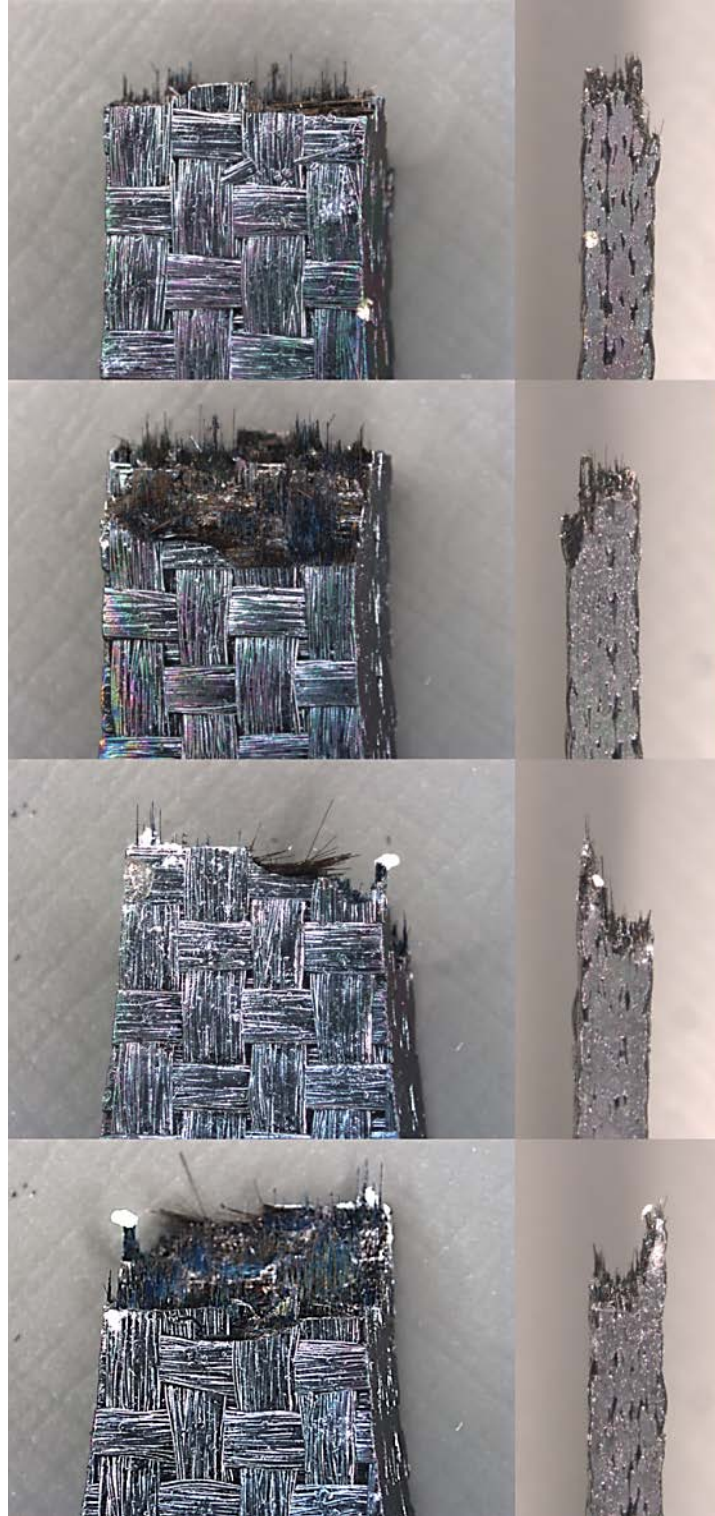
Figure 69: Fracture surface of the DB-shaped specimen tested in fatigue at 1300°C in steam, σ_{max} = 100 MPa, N_f = 200,000, t_f = 55.6 h
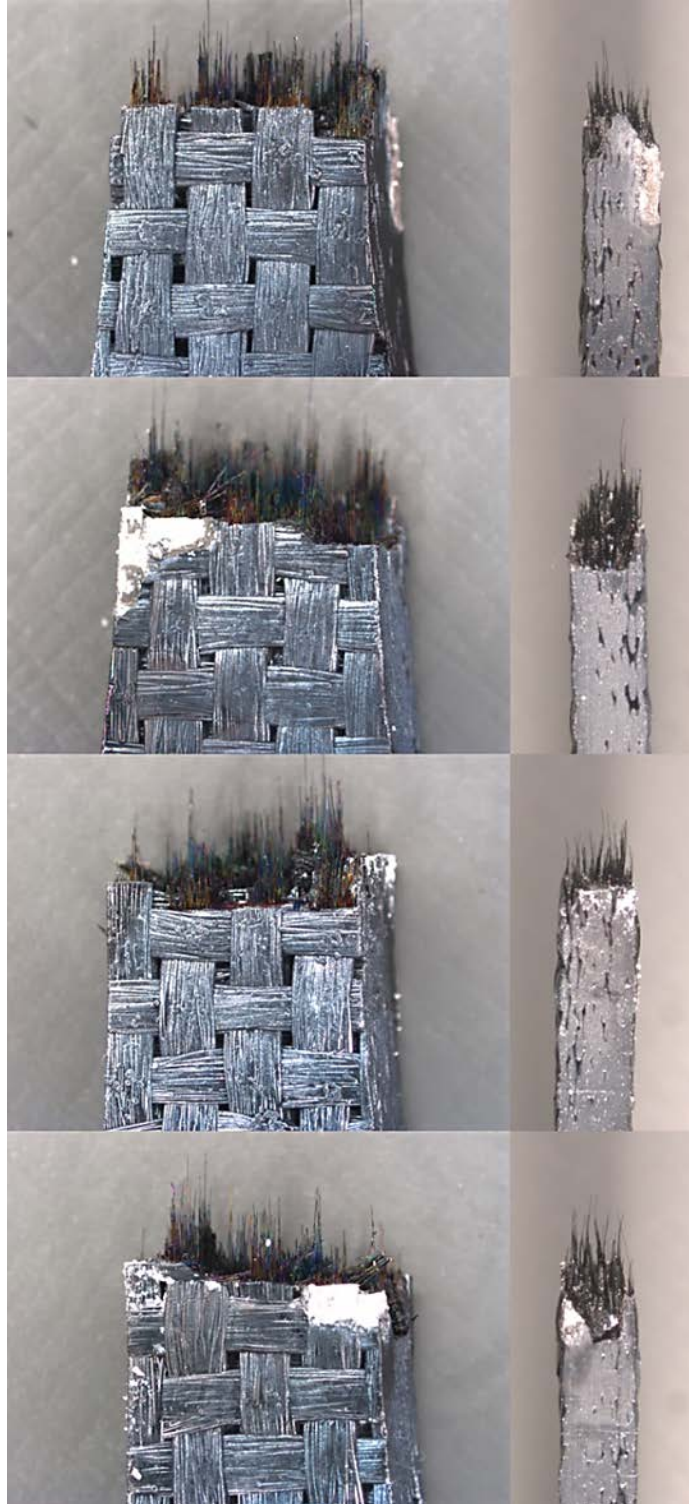
Figure 70: Fracture surface of the HG-shaped specimen tested in fatigue at 1300°C in air, σ_{max} = 145 MPa, N_f = 68,831, t_f = 19.1 h
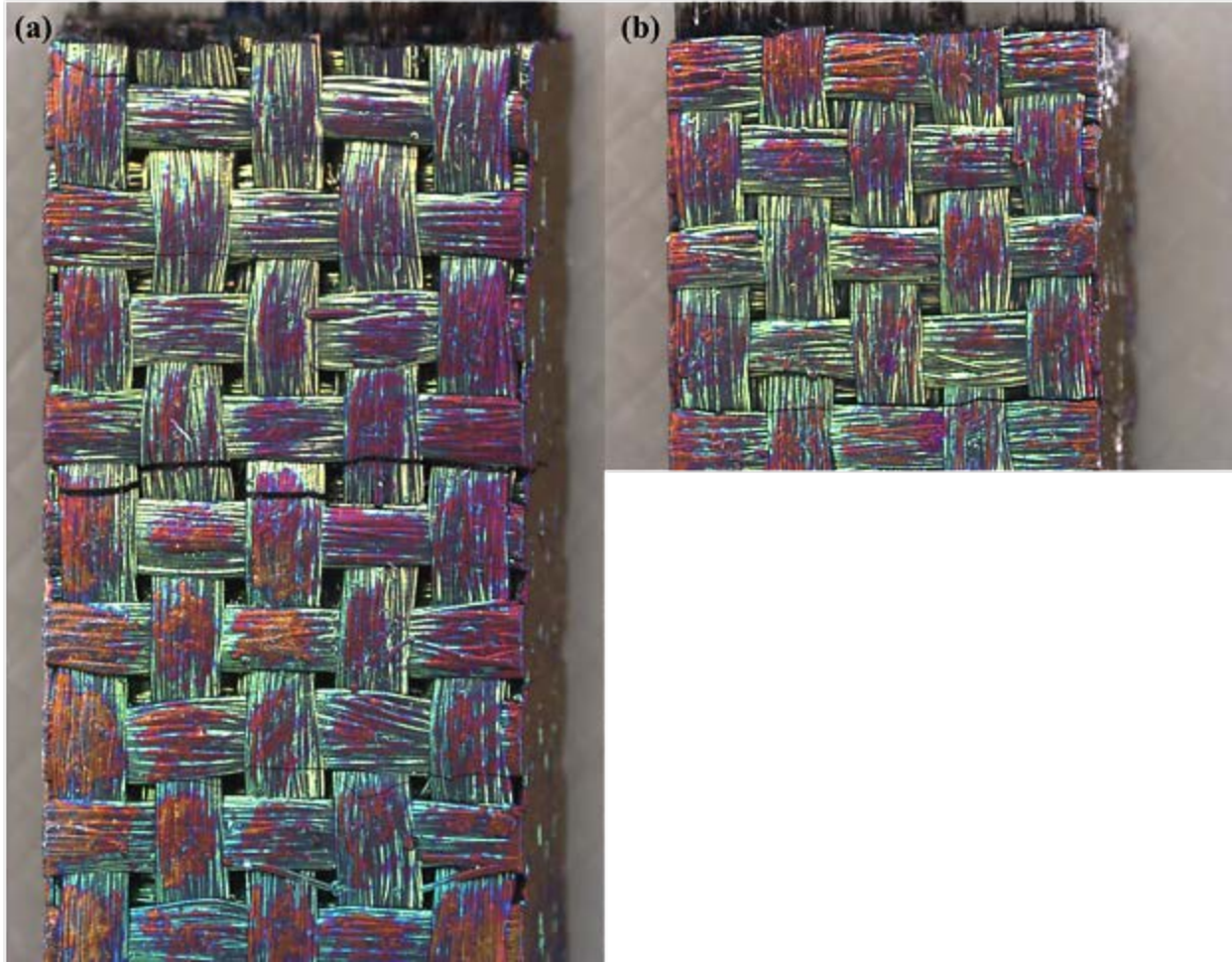
Figure 71: Fracture surface of the HG-shaped specimen tested in fatigue at 1300°C in air, $\sigma_{max} = 80$ MPa, $N_f = 200,000$, $t_f = 55.6$ h

Figure 72: Fracture surface of the HG-shaped specimen tested in fatigue at 1300°C in steam, σ_{max} = 150 MPa, N_f = 13,266, t_f = 3.7 h
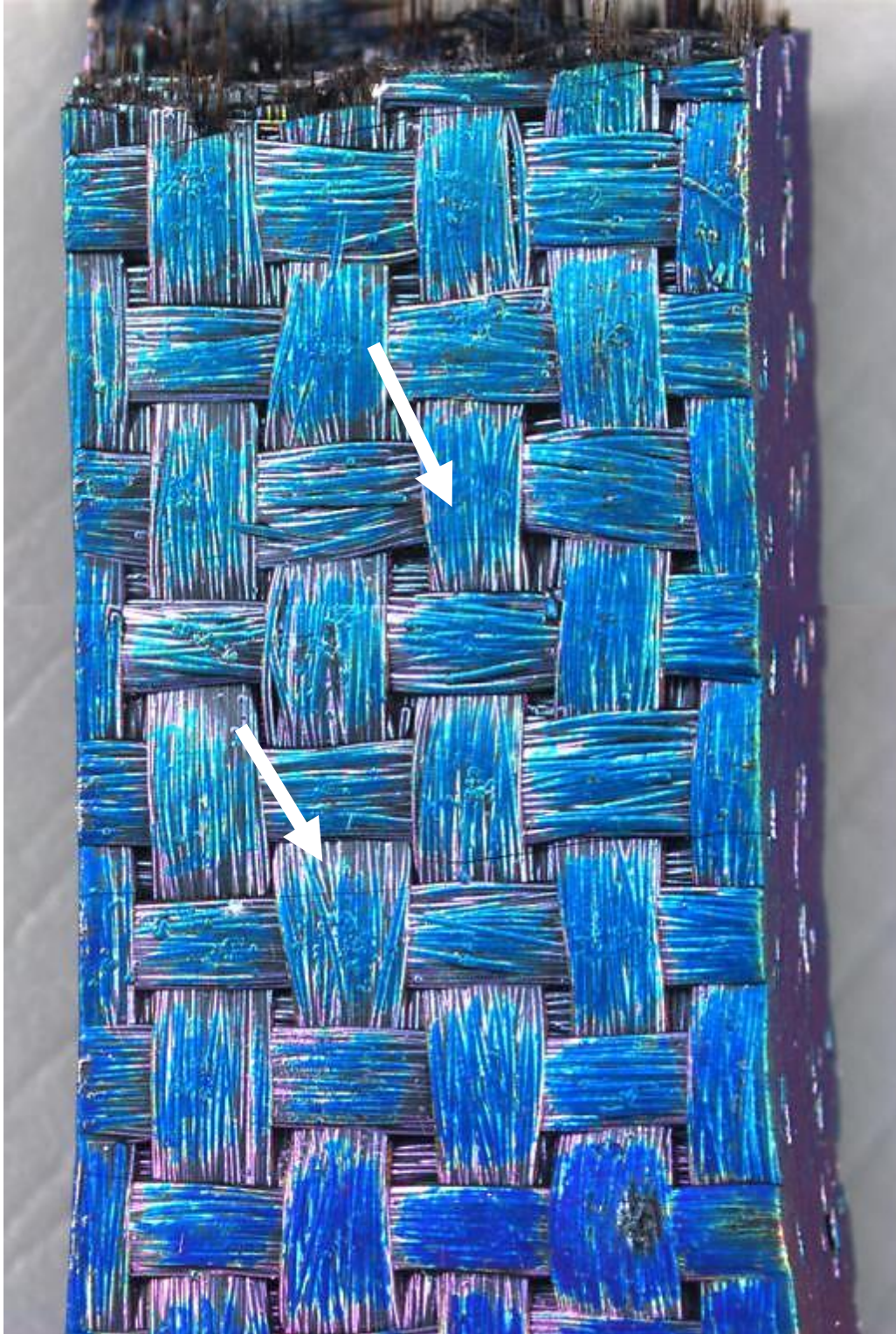
Figure 73: Fracture surface of the HG-shaped specimen tested in fatigue at 1300°C in steam, σ_{max} = 100 MPa, N_f = 200,000, t_f = 55.6 h
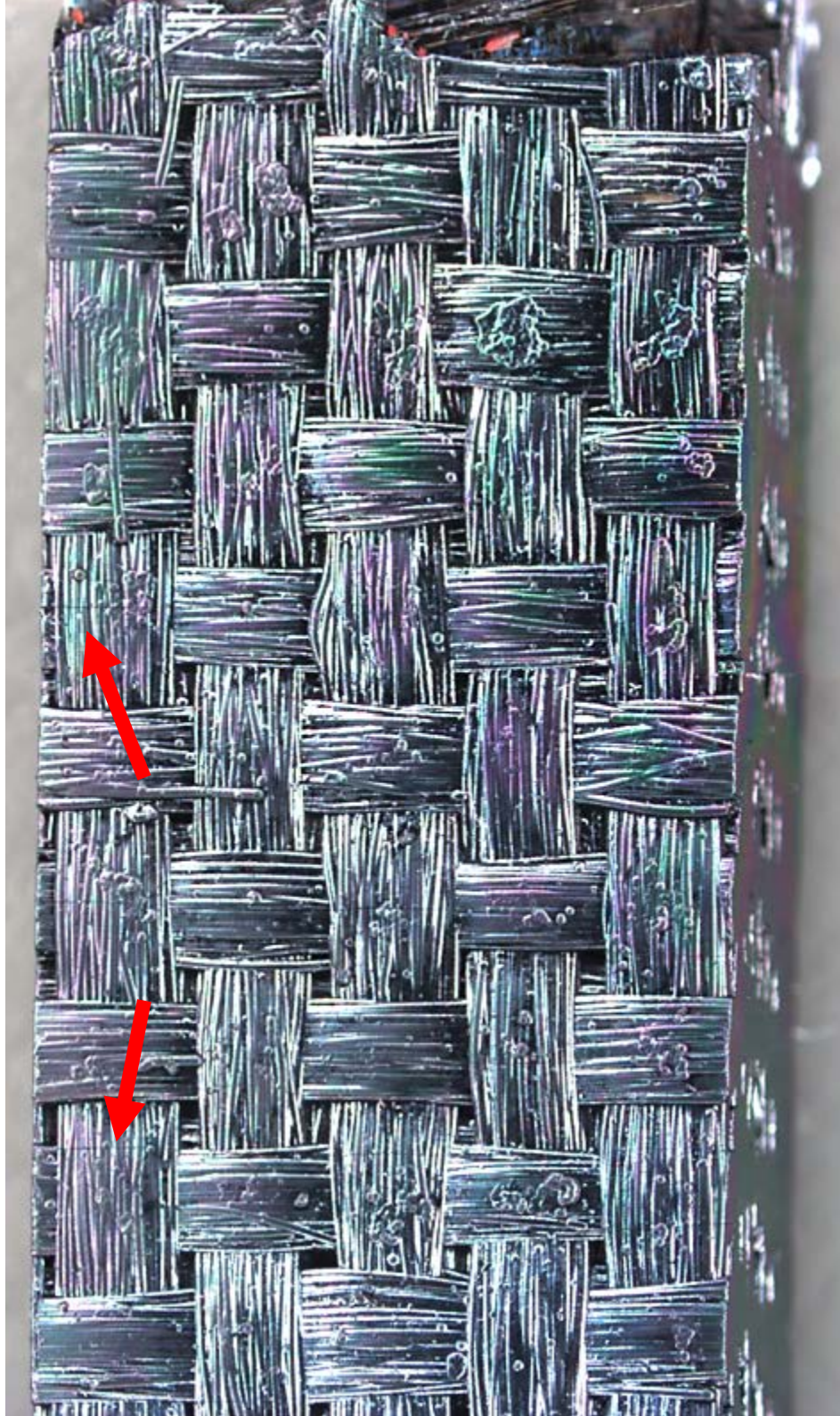
Figure 74: Gage section of the DB-shaped specimen tested in fatigue at 1300°C in air, σ_{max} = 140 MPa, N_f = 20,069, t_f = 5.6 h. Transverse cracks of the 0° fiber bundles are visible on the specimen surface down both the (a) front and (b) back sides of the specimen.

Figure 75: Gage section of the DB-shaped specimen tested in fatigue at 1300°C in air, σ_{max} = 130 MPa, N_f = 38,828, t_f = 10.8 h. Some transverse cracks of the 0° fiber bundles visible shown with arrows.

Figure 76: : Gage section of the DB-shaped specimen tested in fatigue at 1300°C in steam, σ_{max} = 160 MPa, N_f = 17,811, t_f = 4.9 h. Some transverse cracks visible shown with arrows.
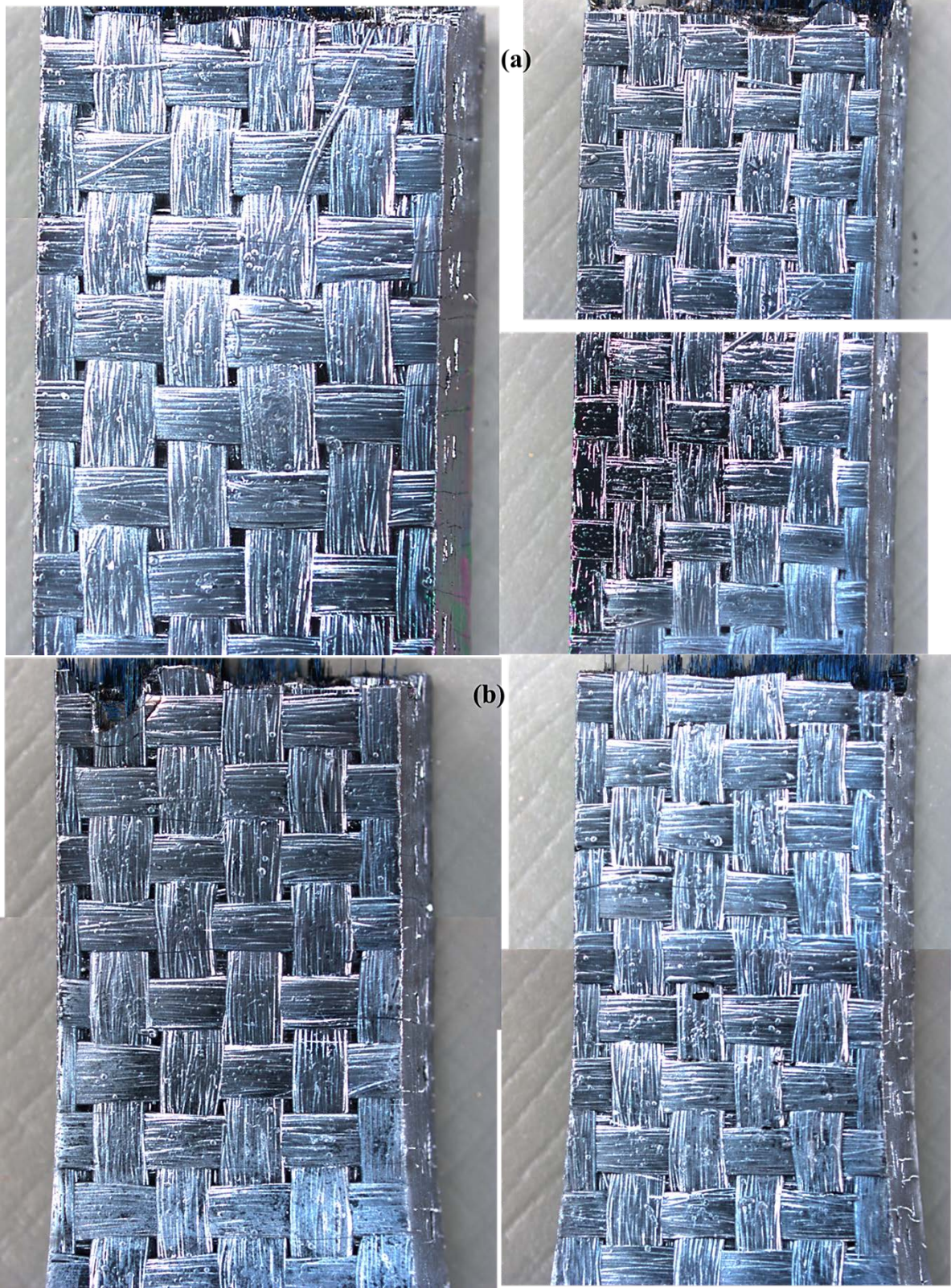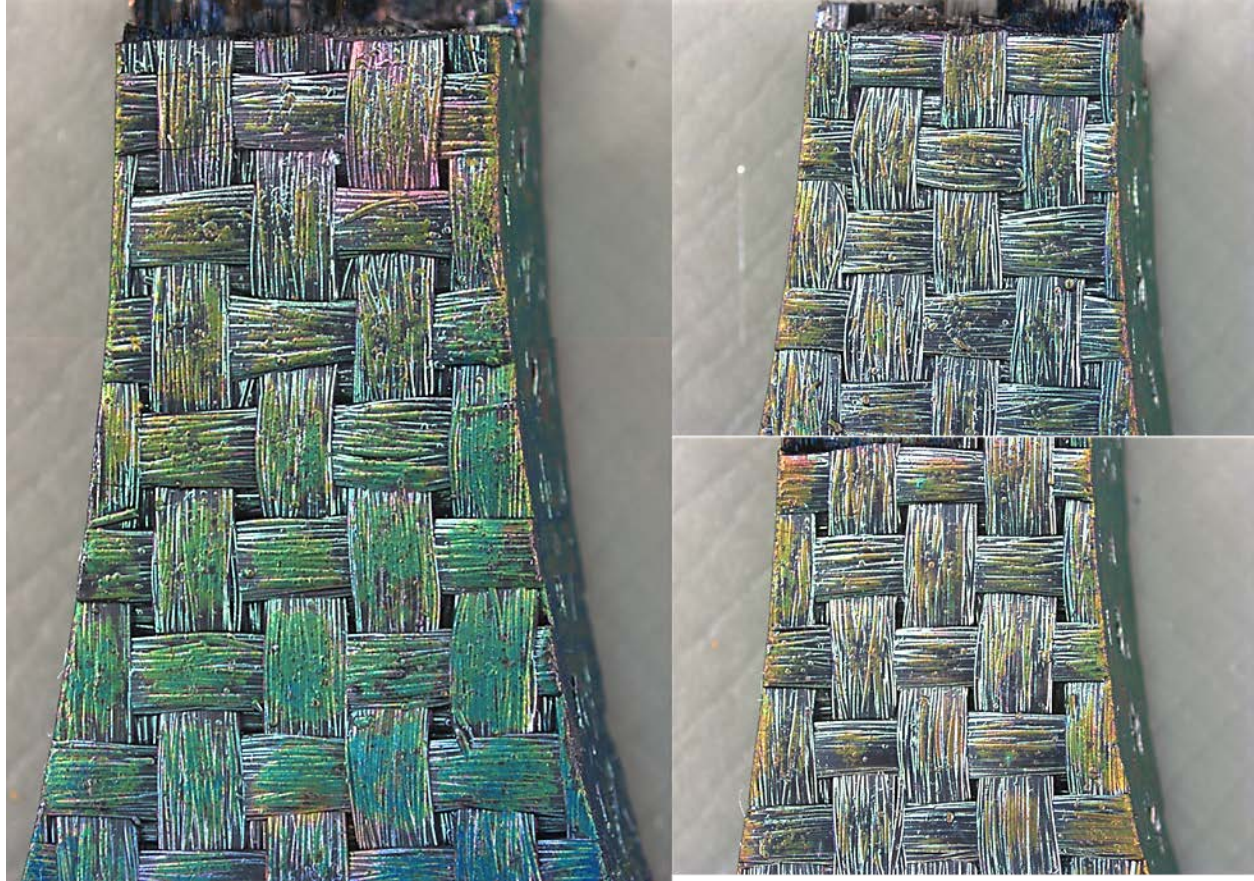
Figure 77: : Gage section of the DB-shaped specimen tested in fatigue at 1300°C in steam, σ_{max} = 140 MPa, N_f = 72,074, t_f = 20.0 h. Lower (a) and upper (b) halves

Figure 78: Gage section of the HG-shaped specimen tested in fatigue at 1300°C in air, σ_{max} = 145 MPa, N_f = 68,831, t_f = 19.1 h. Shows both upper and lower halves.
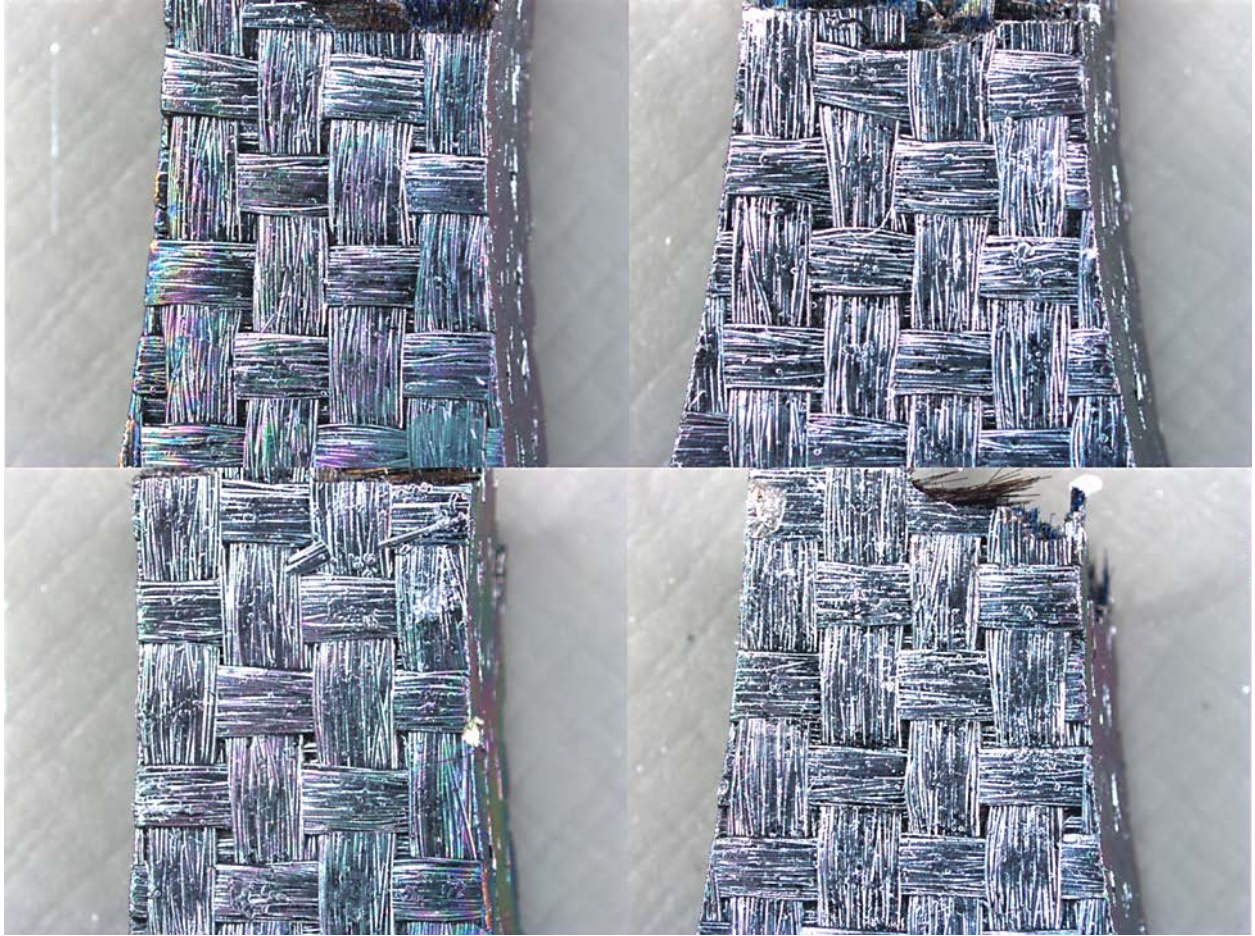
Figure 79: Gage section of the HG-shaped specimen tested in fatigue at 1300°C in steam, σ_{max} = 150 MPa, N_f = 13,266, t_f = 3.7 h. Shows both upper and lower halves.

Appendix B

Figure 80: Fracture surface of the specimen tested in tension to failure at 1300 °C.
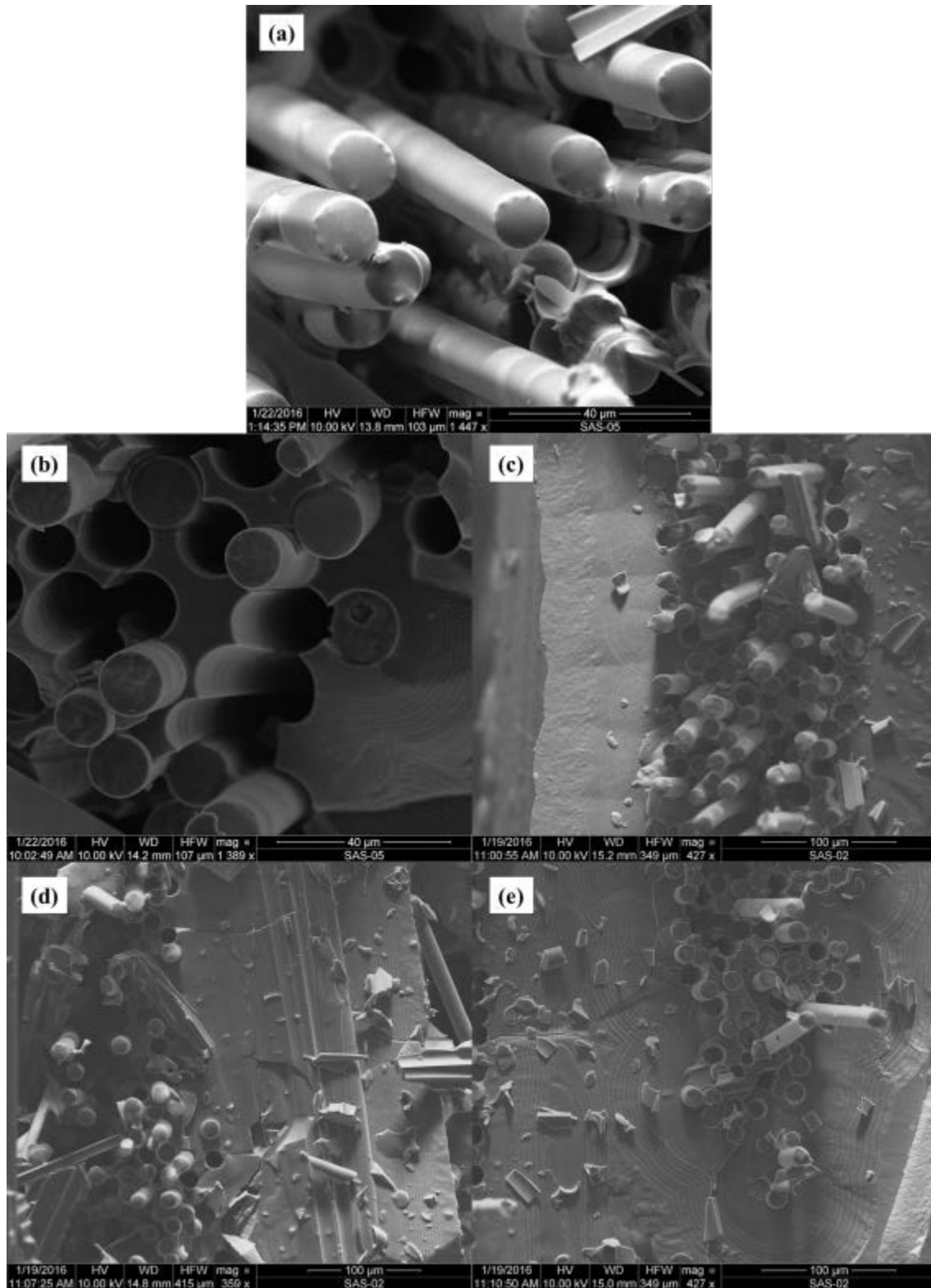
Figure 81: Fracture surface of the specimen tested in tension to failure, 0.05 mm/s at 1300 °C in air. Showing (a) pull-out fibers with oxidized tips, (b) non-oxidized region of matrix with fiber pull-out, (c), (d), and (e) non-oxidized regions with fiber pull-out

Figure 82: Fracture surface of the DB-shaped specimen tested in fatigue at 1300°C in air, σ_{max} = 140 MPa, N_f = 20,069, t_f = 5.6 h. Oxidation visible around the longitudinal fiber tows.
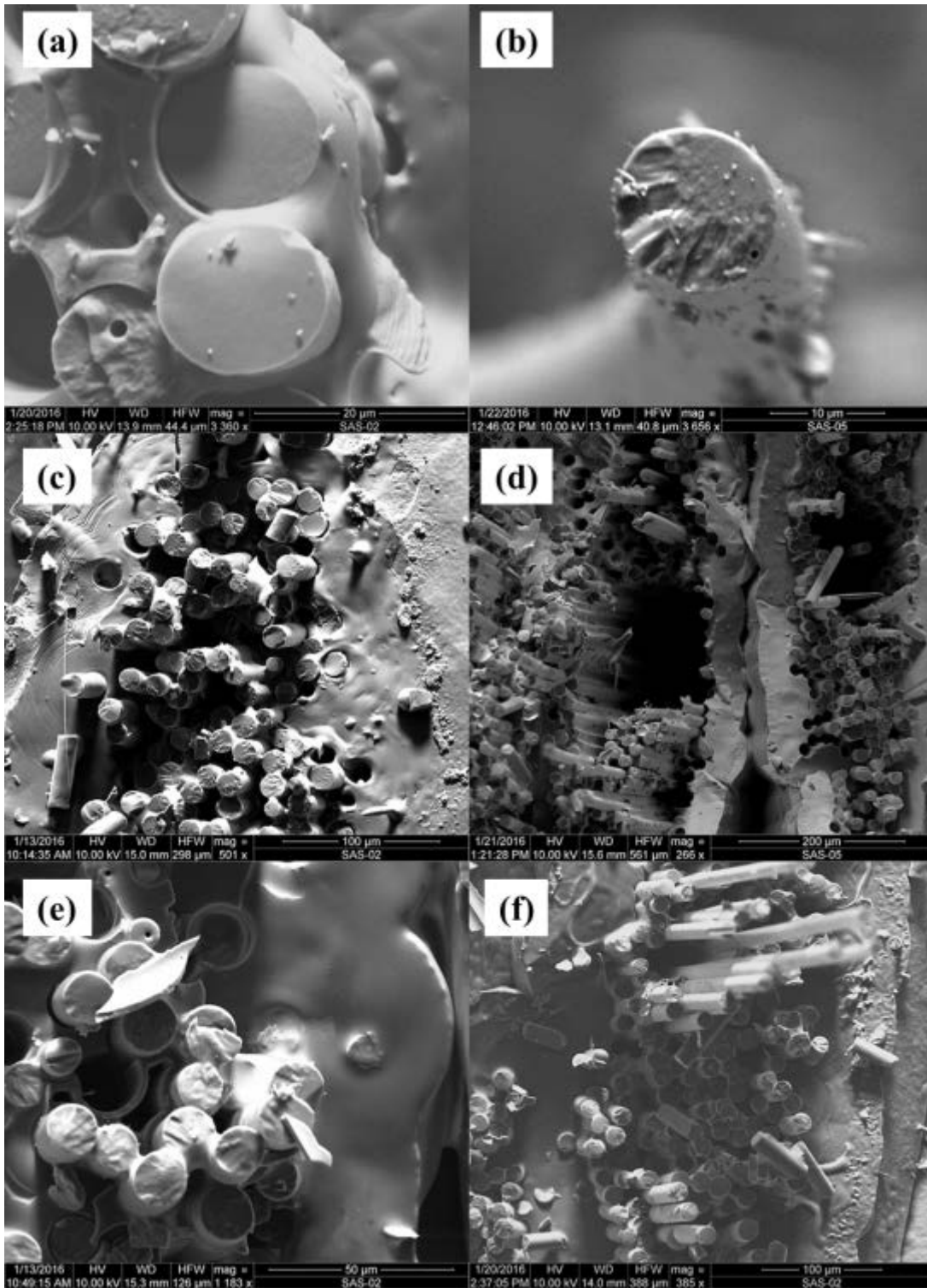
Figure 83: Fracture surface of the DB-shaped specimen tested in fatigue at 1.0 Hz with σ_{max} = 140 MPa at 1300°C in air, (N_f = 20,069, t_f = 5.6 h). Higher magnification images showing: (a) *oxidized* region covering matrix and fibers, (b) non-oxidized pull-out fiber surface, (c) oxidized region with fibers, (d) non-oxidized region with large fiber pull-out, (e) oxidized region with oxidized fibers, and (f) non-oxidized region with pull-out
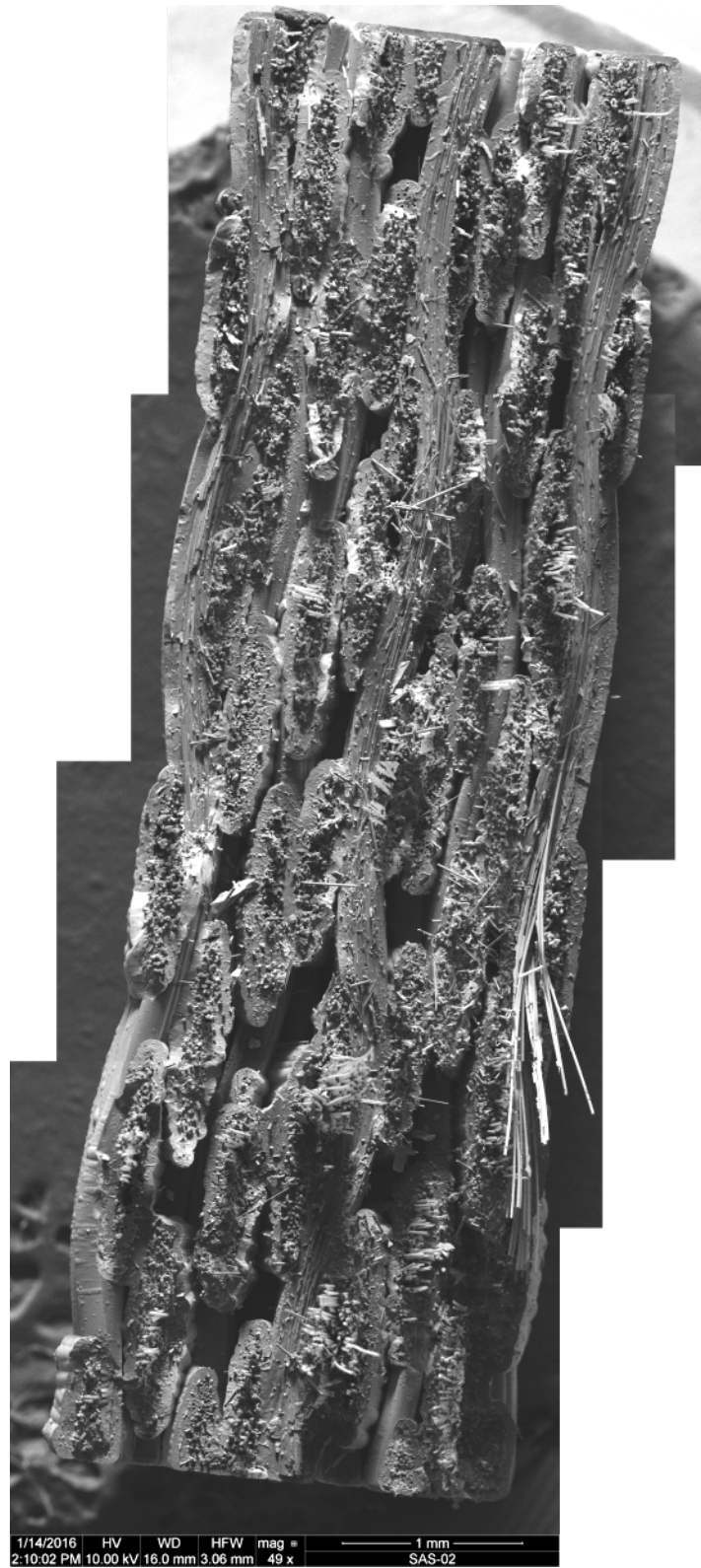
Figure 84: Fracture surface of the DB-shaped specimen tested in fatigue at 1300°C in air, $\sigma_{max} = 130$ MPa, $N_f = 38{,}828$, $t_f = 10.8$ h.
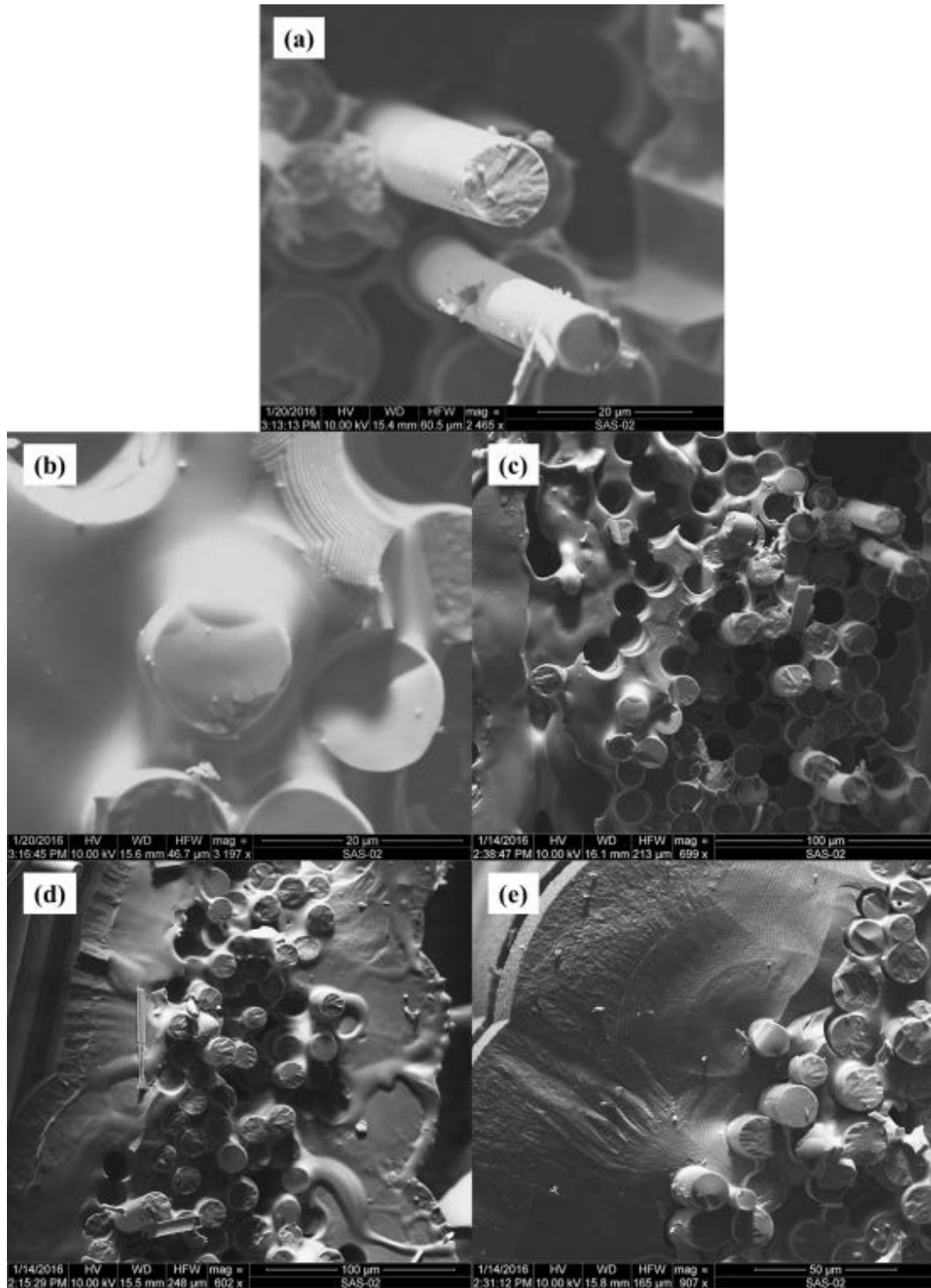
103

Figure 85: Fracture surface of the DB-shaped specimen tested in fatigue at 1.0 Hz with σ_{max} = 130 MPa at 1300°C in air, (N_f = 38,828, t_f = 10.8 h). Higher magnification showing: (a) non-oxidized region with pull-out fibers, (b) glassy phase in *oxidized* region covering fibers, (c) *oxidized* region in the left half of the image transitioning to non-oxidized region with pull-out in the right half of the image, (d) *oxidized* region occupying most of the image, and (e) non-oxidized matrix with some fiber oxidation.

104

Figure 86: Fracture surface of the DB-shaped specimen tested in fatigue at 1300°C in air, σ_{max} = 120 MPa, N_f = 55,199, t_f = 15.3 h.
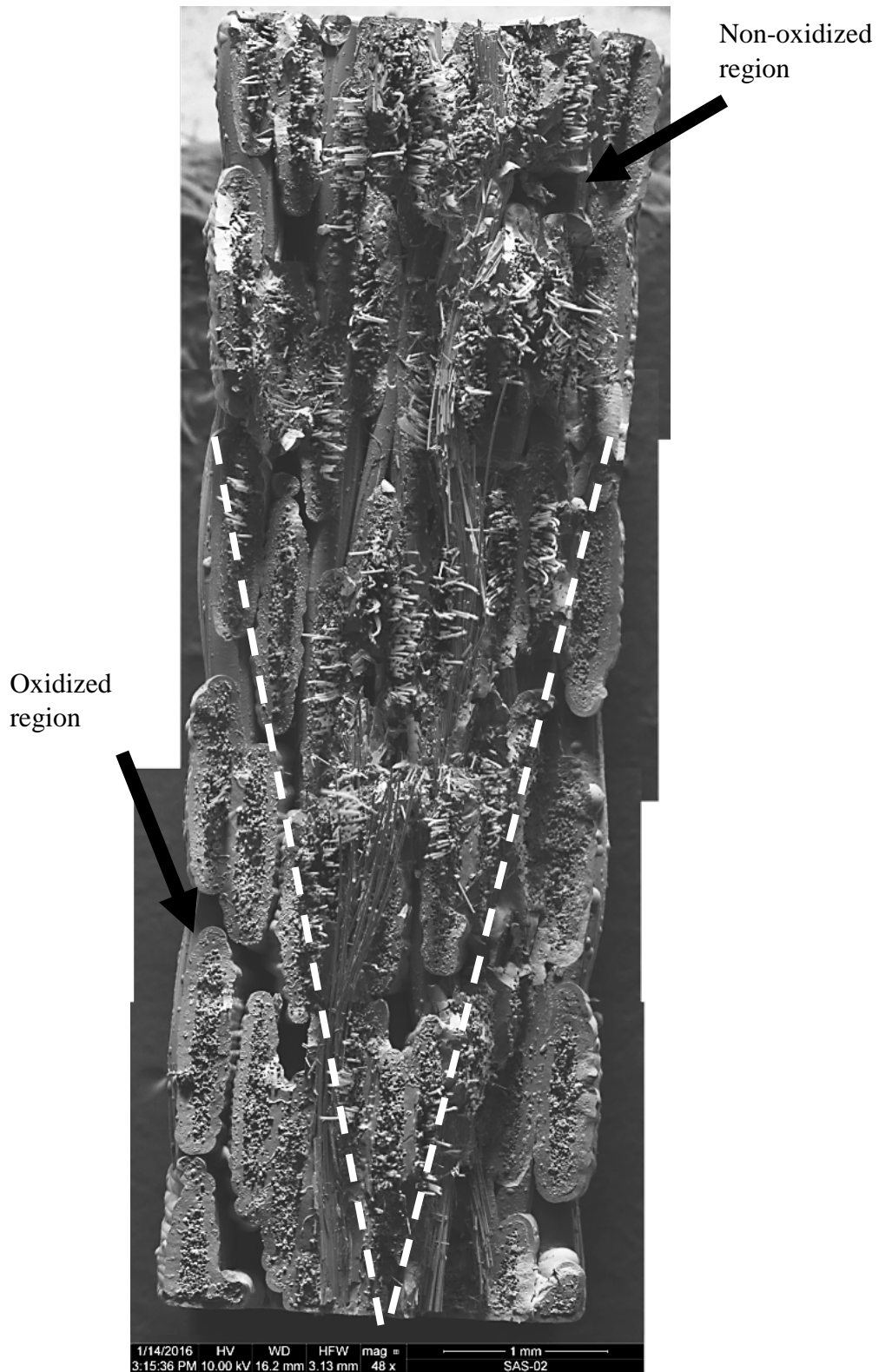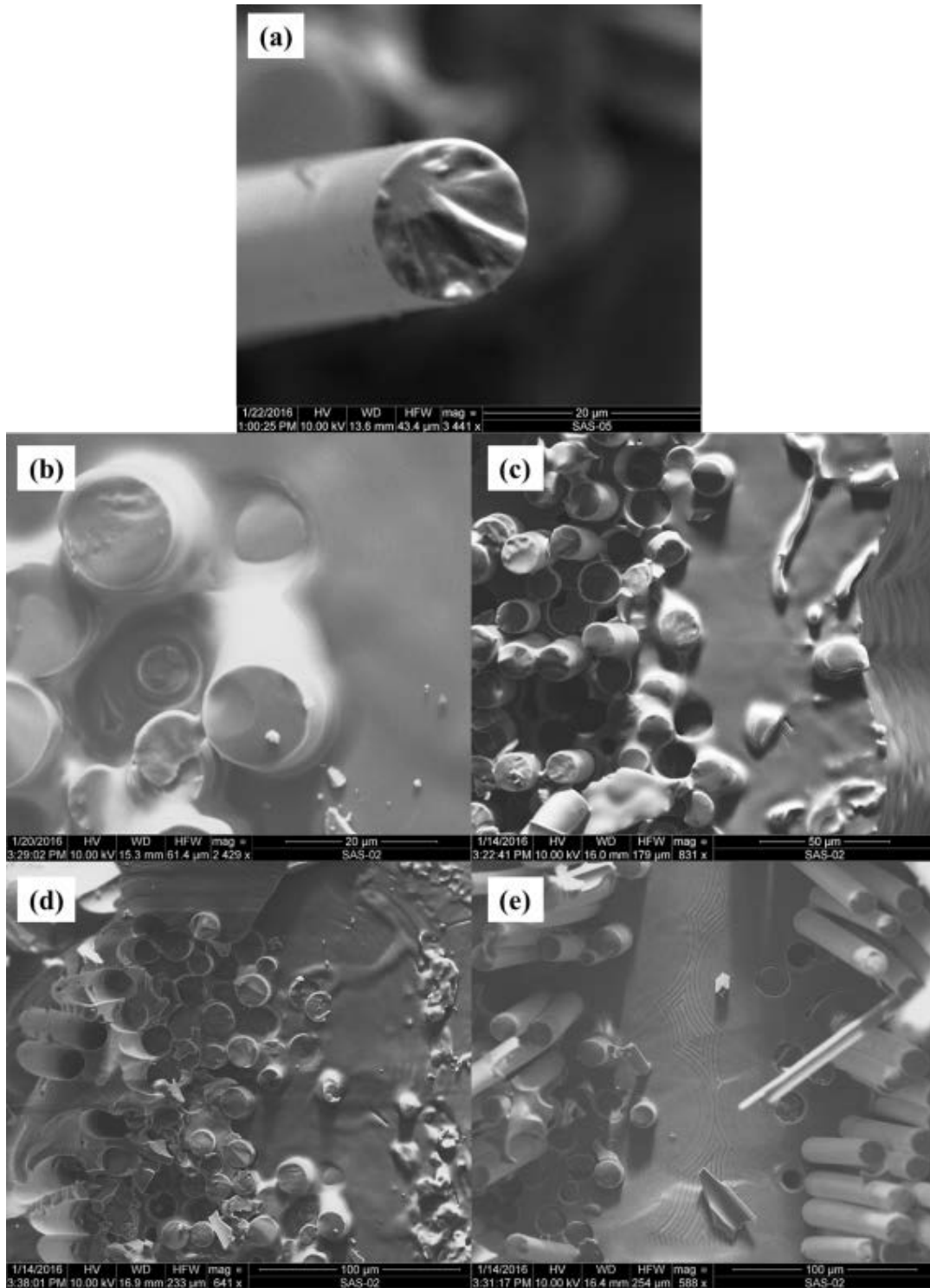
Figure 87: Fracture surface of the DB-shaped specimen tested in fatigue at 1.0 Hz with σ_{max} = 120 MPa at 1300°C in air, (N_f = 55,199, t_f = 15.3 h). Higher magnification showing: (a) glassy phase in the *oxidized* region covering matrix and fibers, (b) fiber pull-out and fracture in the *not oxidized* region, (c)and (d) *oxidized* region in the right half of the image transitioning to the *not* oxidized region in the left half of the image, and (e) fiber pull-out typical in the *not* oxidized region.

Figure 88: Fracture surface of the DB-shaped specimen tested in fatigue at 1300°C in air, σ_{max} = 100 MPa, N_f = 84,855, t_f = 23.6 h.
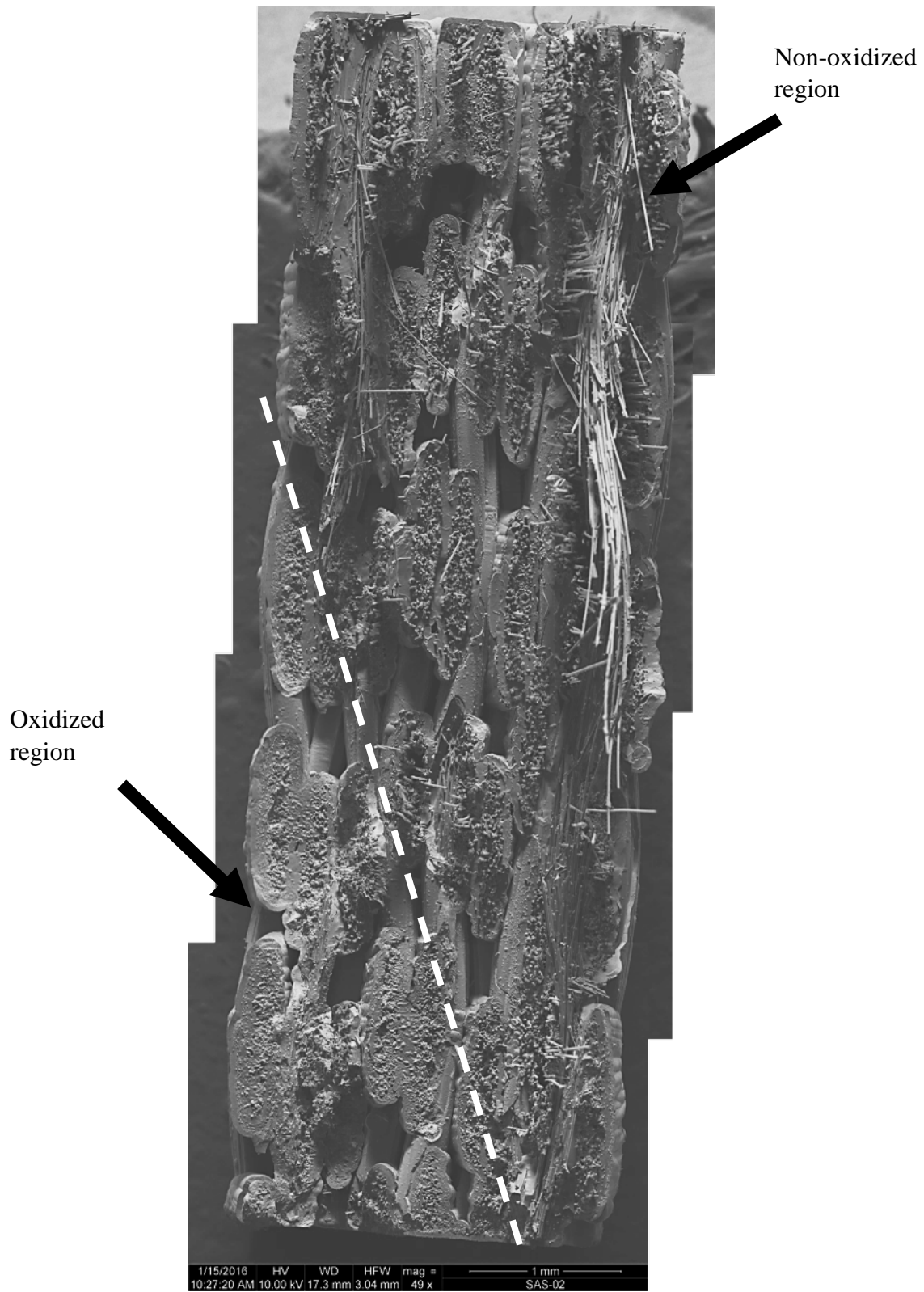
107

Figure 89: Fracture surface of the DB-shaped specimen tested in fatigue at 1.0 Hz with σ_{max} = 100 MPa at 1300°C in air, (N_f = 84,855, t_f = 23.6 h). Higher magnification images showing: (a) non-oxidized region with pull-out fibers, (b) and (d) glassy phase in *oxidized* region covering fibers and matrix, (c) *oxidized* region in the left half of the image transitioning to the non-oxidized region in the right half of the image with fiber pull-out, and (e) *oxidized* region occupying most of the image.
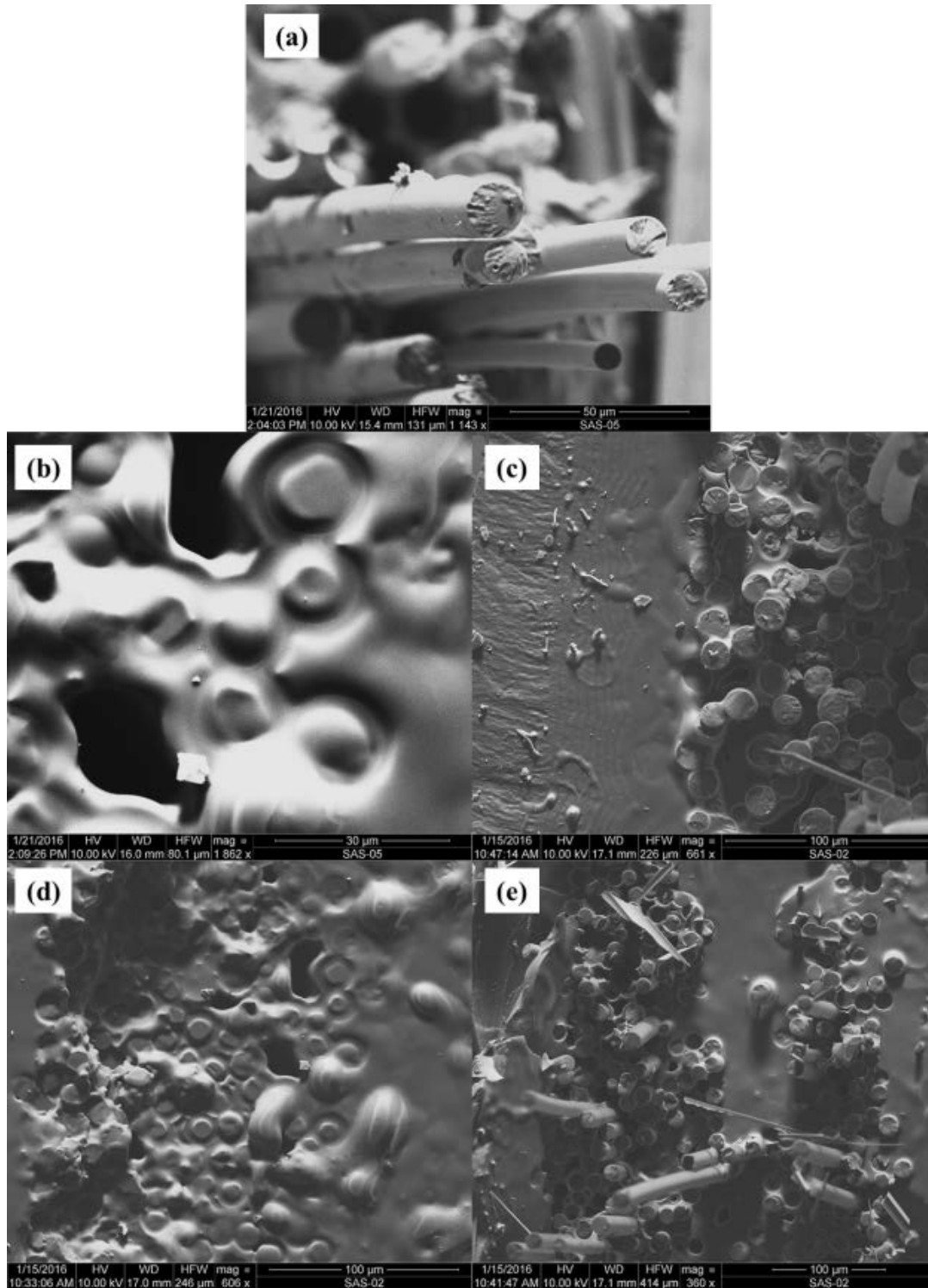
Figure 90: Fracture surface of the DB-shaped specimen tested in fatigue at 1300°C in air, σ_{max} = 70 MPa, N_f = 200,000, t_f = 55.6 h.

Figure 91: Fracture surface of the DB-shaped specimen tested in fatigue at 1.0 Hz with σ_{max} = 70 MPa at 1300°C in air, (N_f = 200,000, t_f = 55.6 h). Higher magnification images showing: (a) fiber pull-out with oxidized tips, (b) and (c) regions showing non-oxidized matrix and fiber pull-out

Figure 92: Fracture surface of the DB-shaped specimen tested in fatigue at 1300°C in steam, σ_{max} = 160 MPa, N_f = 17,811, t_f = 4.9 h.
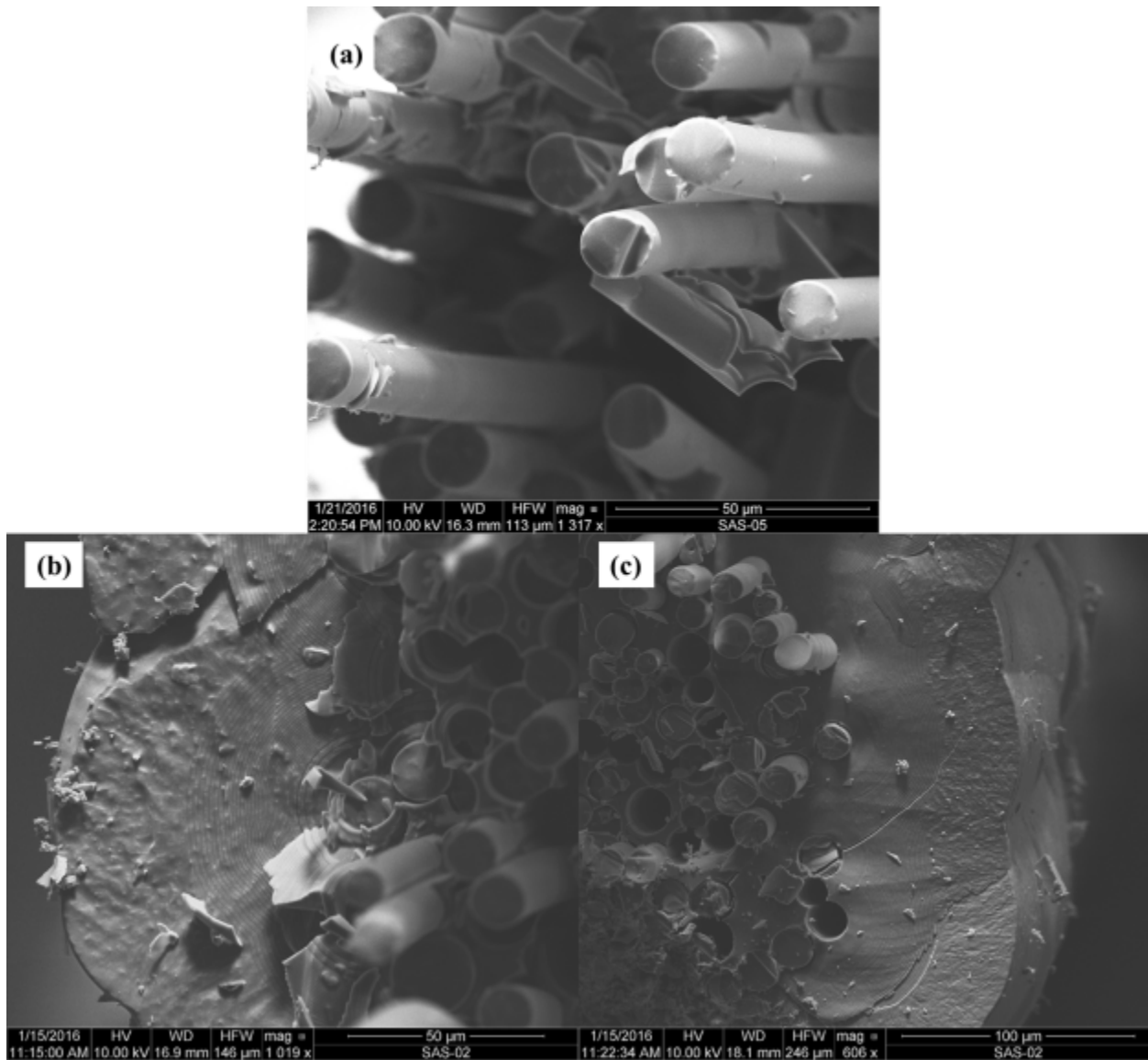
Figure 93: Fracture surface of the DB-shaped specimen tested in fatigue at 1.0 Hz with σ_{max} = 160 MPa at 1300°C in steam, (N_f = 17,811, t_f = 4.9 h). Higher magnification images showing: (a) glassy phase in *oxidized* region covering matrix and fibers, (b) non-oxidized region with pull-out fiber fracture surfaces, (c) *oxidized* region in the left half of the image transitioning to a non-oxidized region with fiber pull-out, and (d) *oxidized* region in the right half of the image transitioning to non-oxidized region with fibers pulled-out.
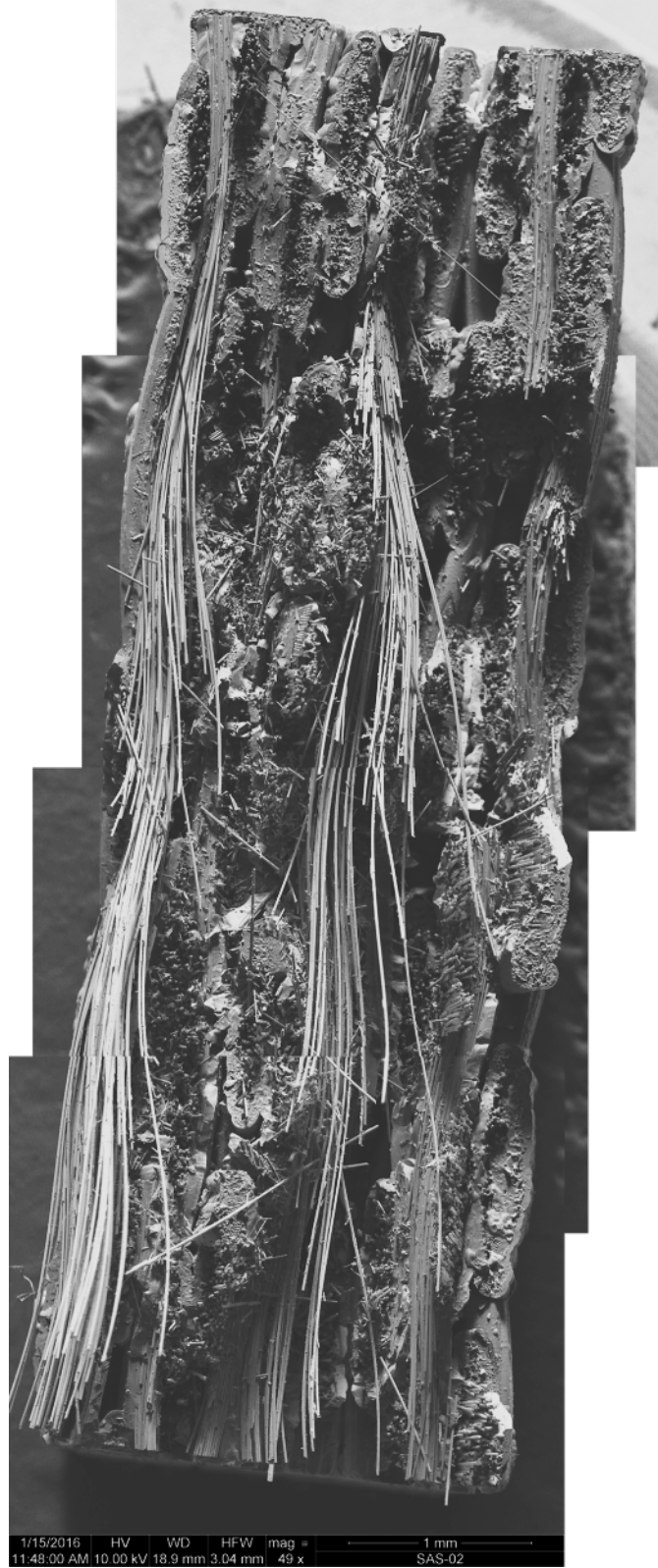
Non-oxidized region

Oxidized region

Figure 94: Fracture surface of the DB-shaped specimen tested in fatigue at 1300°C in steam, σ_{max} = 140 MPa, N_f = 72,074, t_f = 20.0 h.
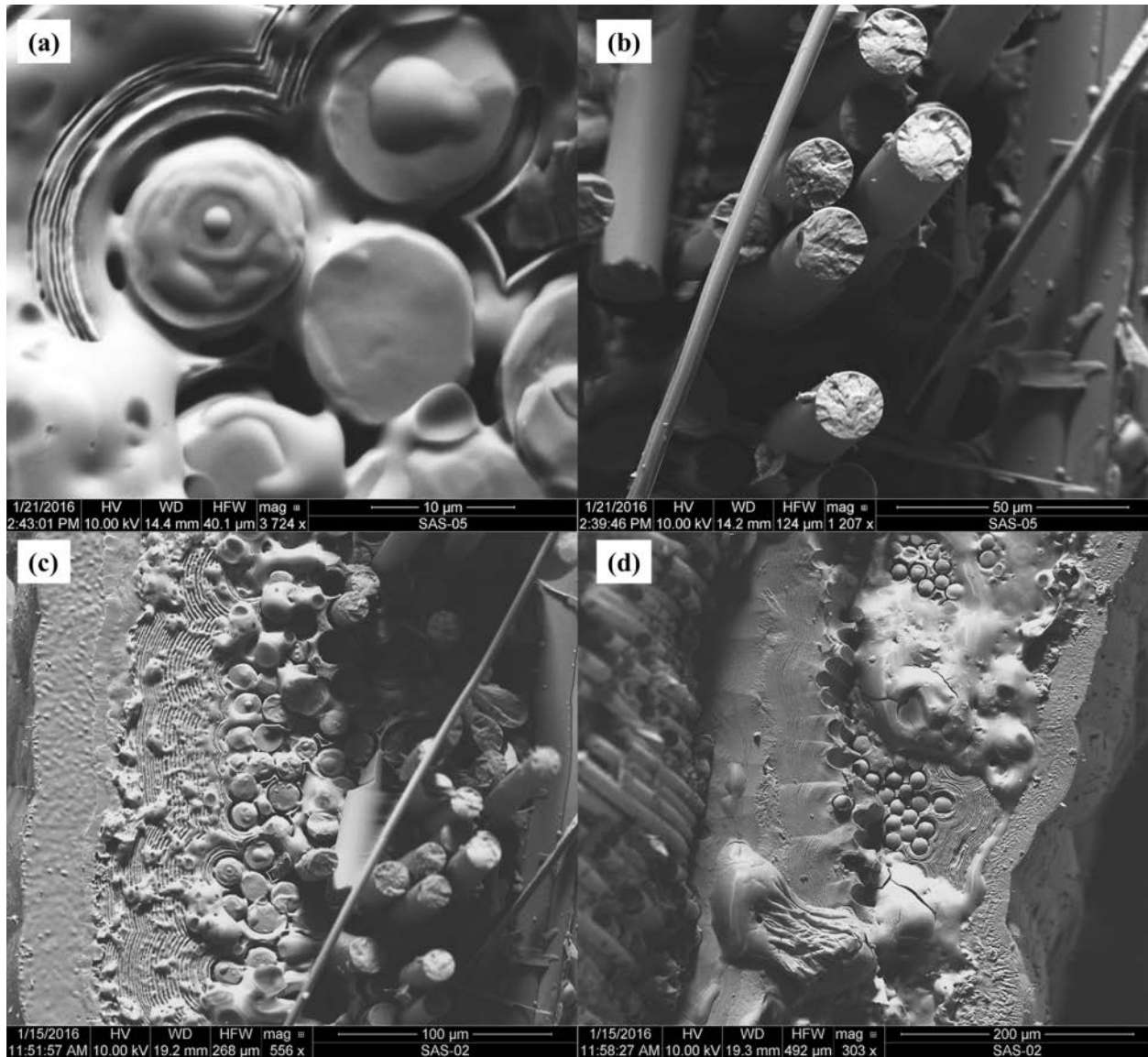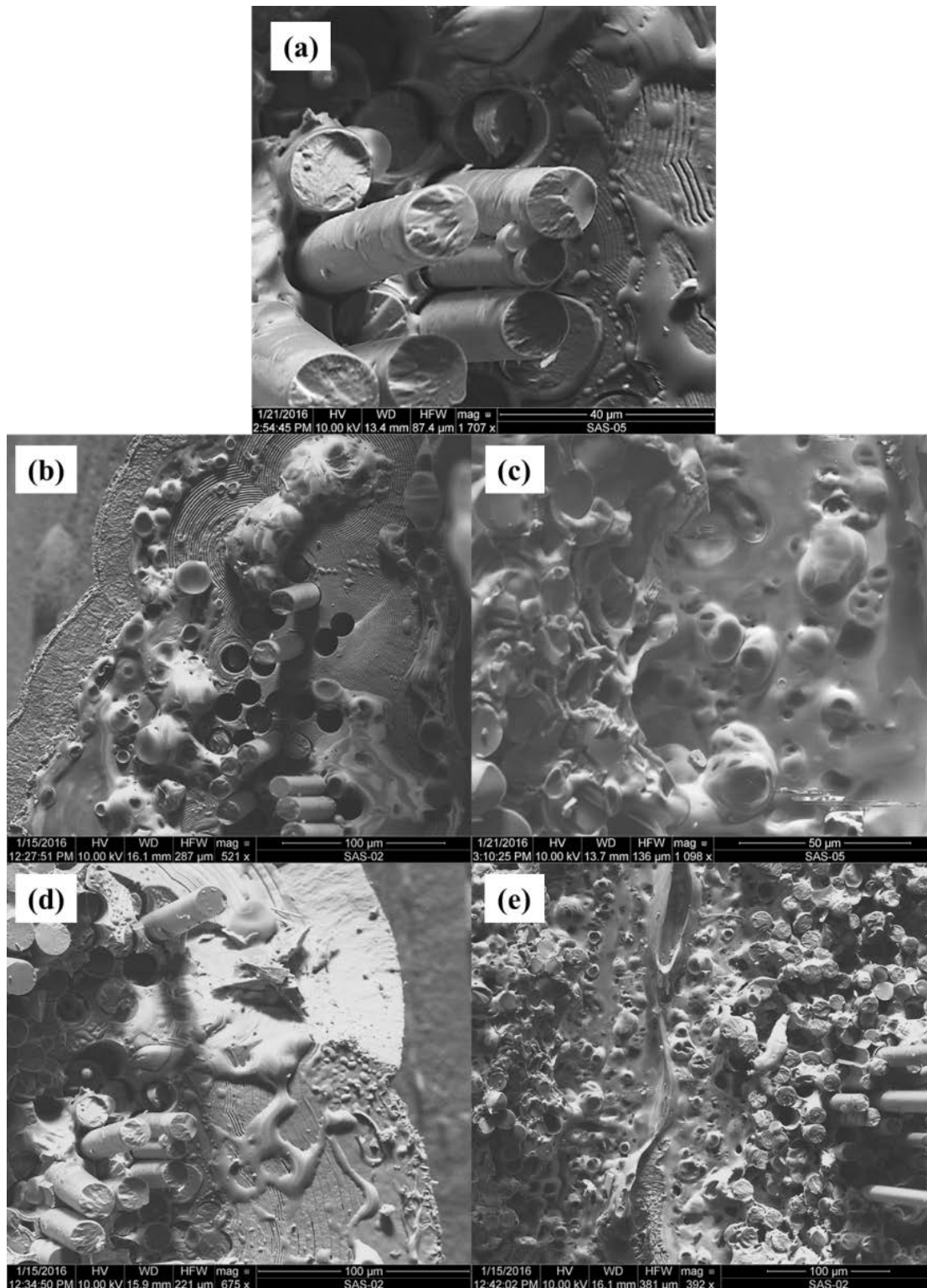
113

Figure 95: Fracture surface of the DB-shaped specimen tested in fatigue at 1.0 Hz with σ_{max} = 140 MPa at 1300°C in steam, (N_f = 72,074, t_f = 20.0 h). Higher magnification images showing: (a) and (d) transition from the *oxidized* region in the right half of the image to not oxidized region in the left half of the image covering matrix with brittle fiber fracture surfaces, (c) and (e) glassy phase in the *oxidized* region covering matrix and fibers.

114

Figure 96: Fracture surface of the DB-shaped specimen tested in fatigue at 1300°C in steam, σ_{max} = 120 MPa, N_f = 93,016, t_f = 25.8 h. Visible oxidation regions with an approximate transition to fiber pull-out occurring along the dotted line.

115

Figure 97: Fracture surface of the DB-shaped specimen tested in fatigue at 1.0 Hz with σ_{max} = 120 MPa at 1300°C in steam, (N_f = 93,016, t_f = 25.8 h). Higher magnification images showing: (a) non-oxidized region with brittle fiber fracture and fiber pull-out, (c) glassy phase in *oxidized* region covering fibers and matrix, (d) and (e) *oxidized* region occupying most of the image.
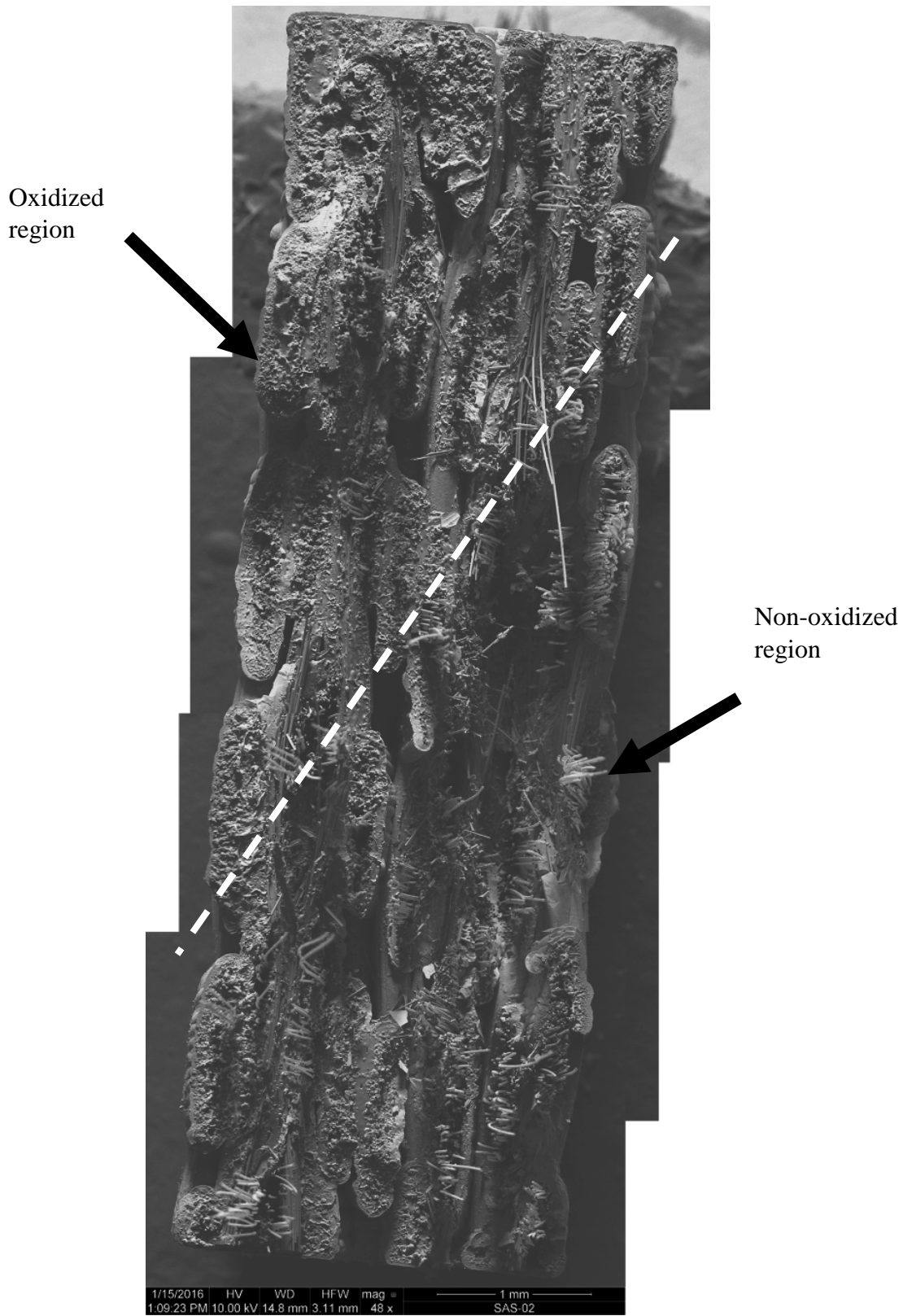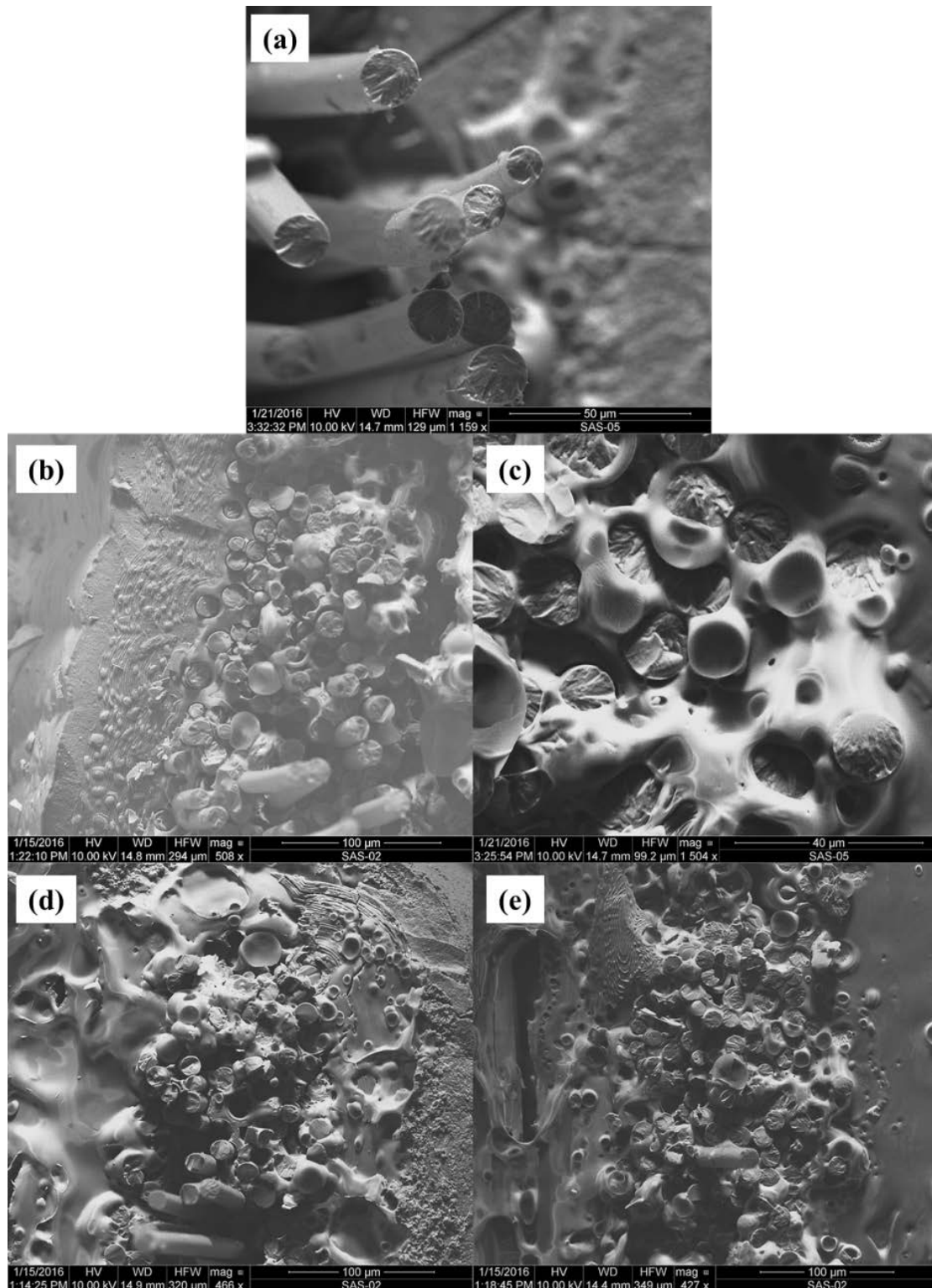
Figure 98: Fracture surface of the DB-shaped specimen tested in fatigue at 1300°C in steam, σ_{max} = 100 MPa, N_f = 200,000, t_f = 55.6 h. Visible oxidation regions with an approximate transition to fiber pull-out occurring along the dotted line.
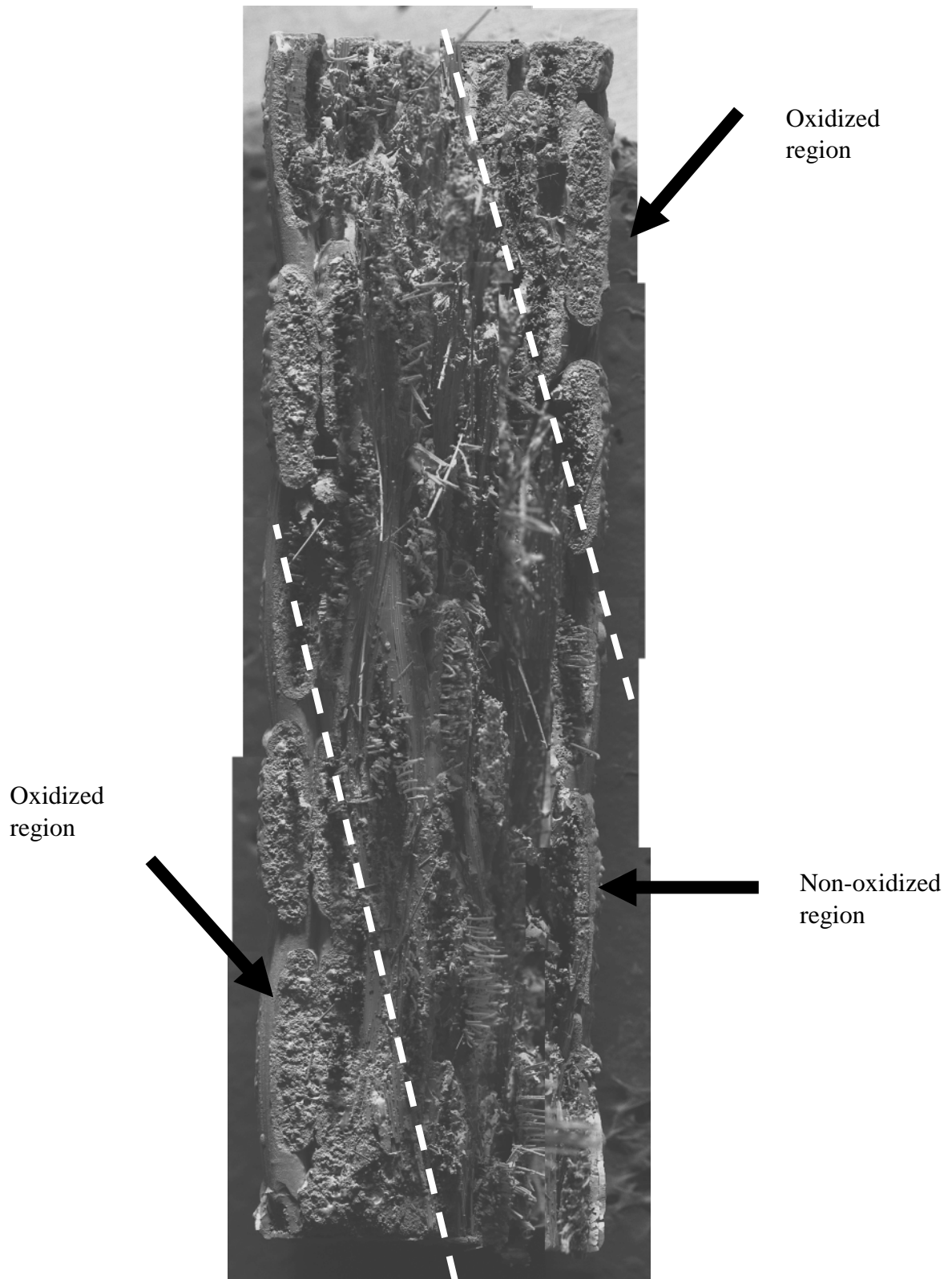
Figure 99: Fracture surface of the DB-shaped specimen tested in fatigue at 1.0 Hz with σ_{max} = 100 MPa at 1300°C in steam, (N_f = 200,000, t_f = 55.6 h). Higher magnification images showing: (a) oxidation of the fracture surfaces of the pulled-out fibers, (b) glassy phase in the *oxidized* region covering matrix and fibers, (c), (d), and (e) oxidized region occupying most of the image.

118

Figure 100: Fracture surface of the HG-shaped specimen tested in fatigue at 1300°C in air, σ_{max} = 145 MPa, N_f = 68,831, t_f = 19.1 h.
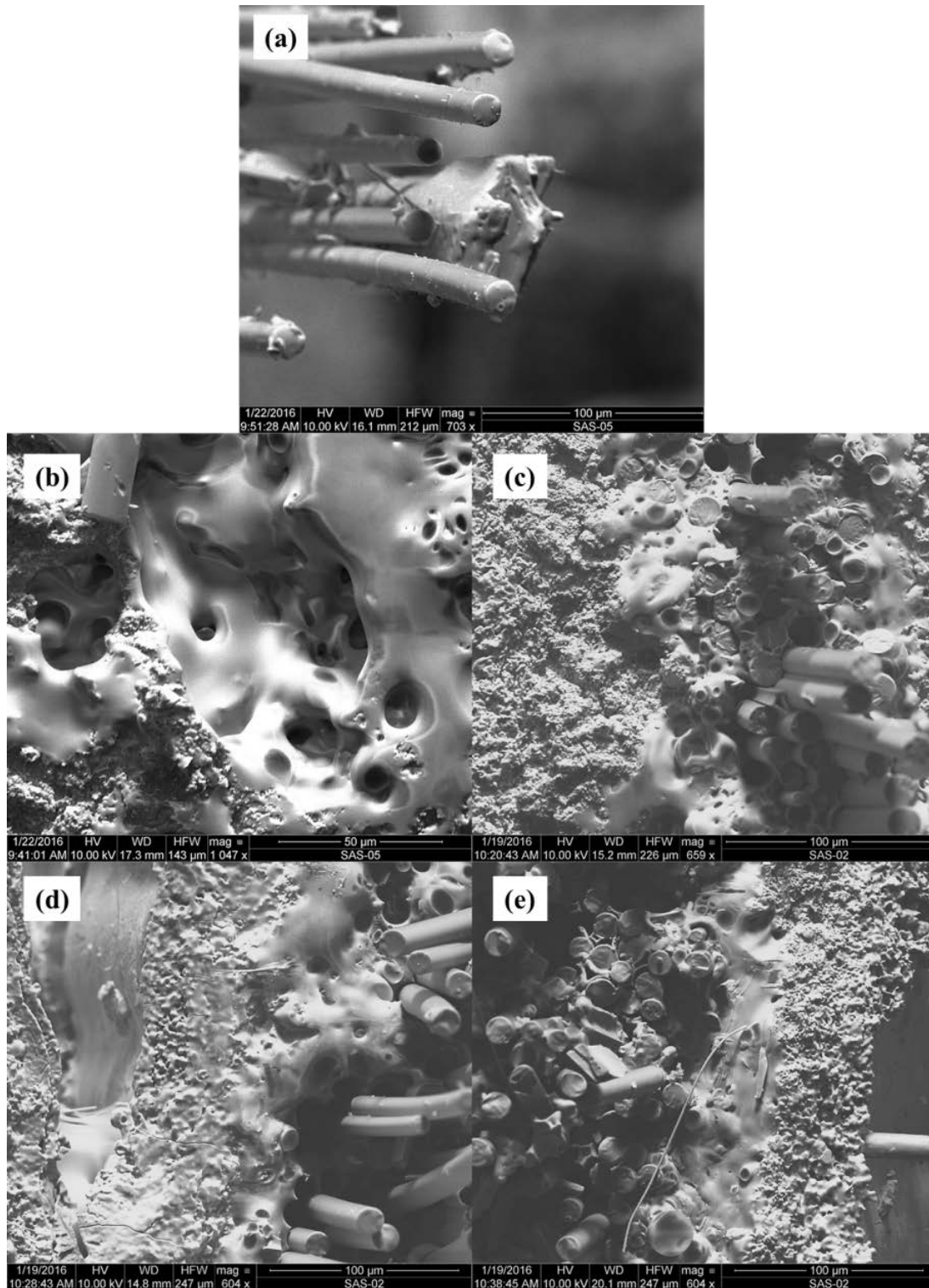
Figure 101: Fracture surface of the HG-shaped specimen tested in fatigue at 1.0 Hz with σ_{max} = 145 MPa at 1300°C in air, (N_f = 68,831, t_f = 19.1 h). Higher magnification images showing: (a) glassy phase of in the *oxidized* region covering matrix and fibers, (b) pulled-out fibers, (c) and (d) *oxidized* region occupying most of the image.

Figure 102: Fracture surface of the HG-shaped specimen tested in fatigue at 1300°C in air,
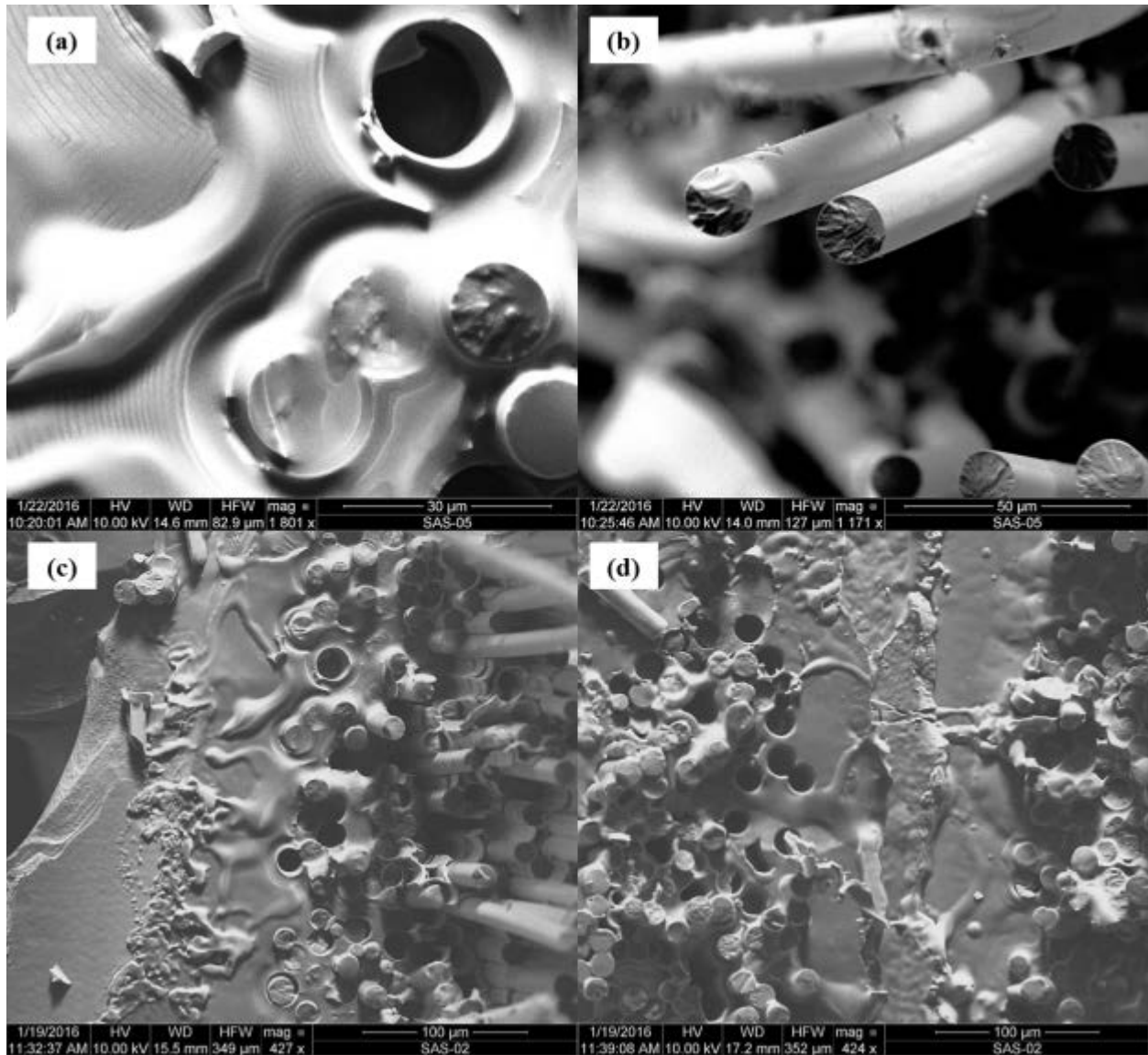$\sigma_{max} = 80$ MPa, $N_f = 200{,}000$, $t_f = 55.6$ h.

Figure 103: Fracture surface of the HG-shaped specimen tested in fatigue at 1.0 Hz with σ_{max} = 80 MPa at 1300°C in air, (N_f = 200,000, t_f = 55.6 h). Higher magnification images showing regions with no matrix oxidation.

Figure 104: Fracture surface of the HG-shaped specimen tested in fatigue at 1300°C in steam, σ_{max} = 150 MPa, N_f = 13,266, t_f = 3.7 h.

www.manaraa.com

Figure 105: Fracture surface of the HG-shaped specimen tested in fatigue at 1.0 Hz with σ_{max} = 150 MPa at 1300°C in steam, (N_f = 13,266, t_f = 3.7 h). Higher magnification images showing: (a) fiber fracture surfaces, (b) glassy phase in the *oxidized* region covering matrix and fibers, (c) fiber pull-out in the non-oxidized region, and (d) planar fracture surface morphology in the oxidized region.
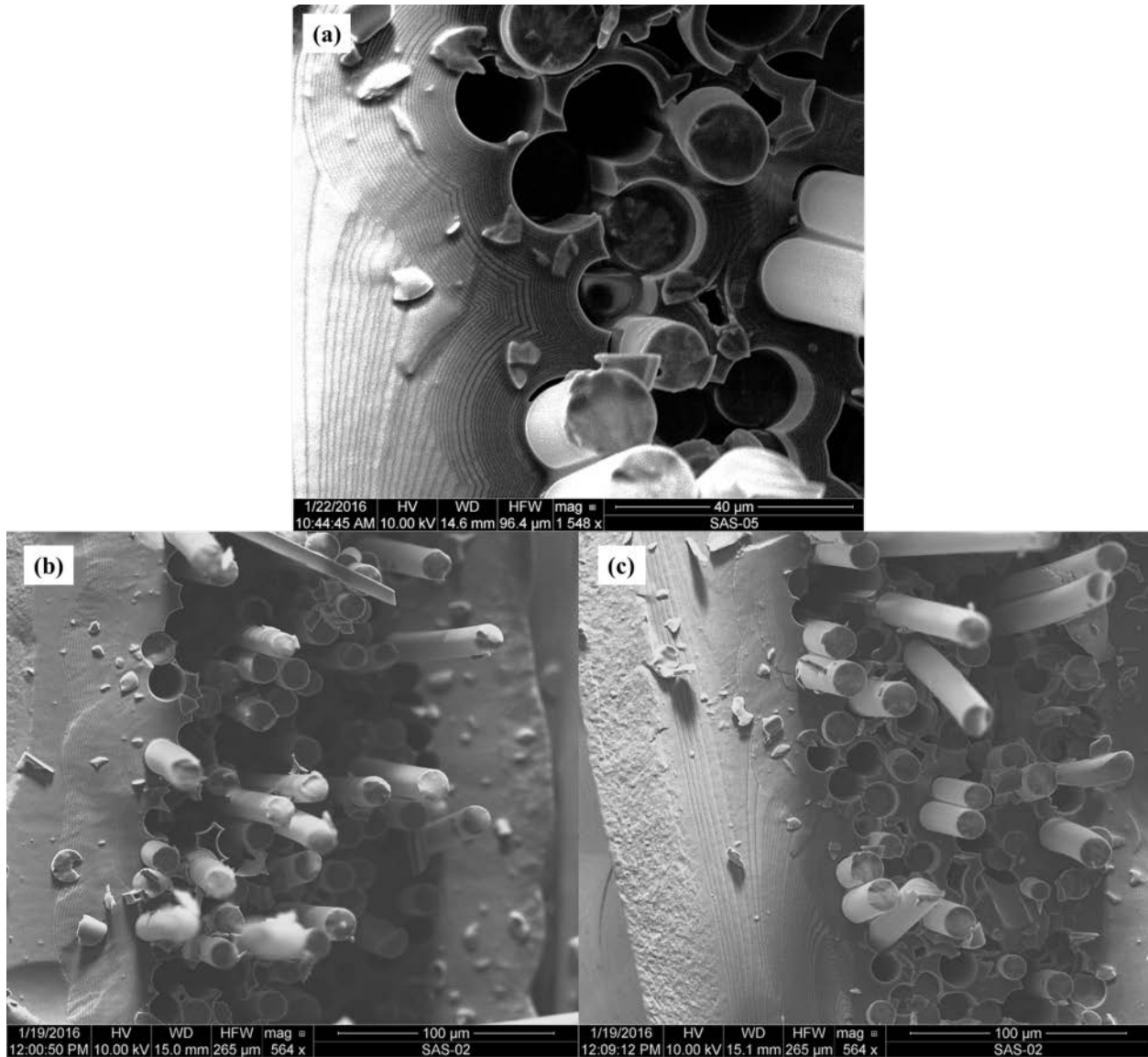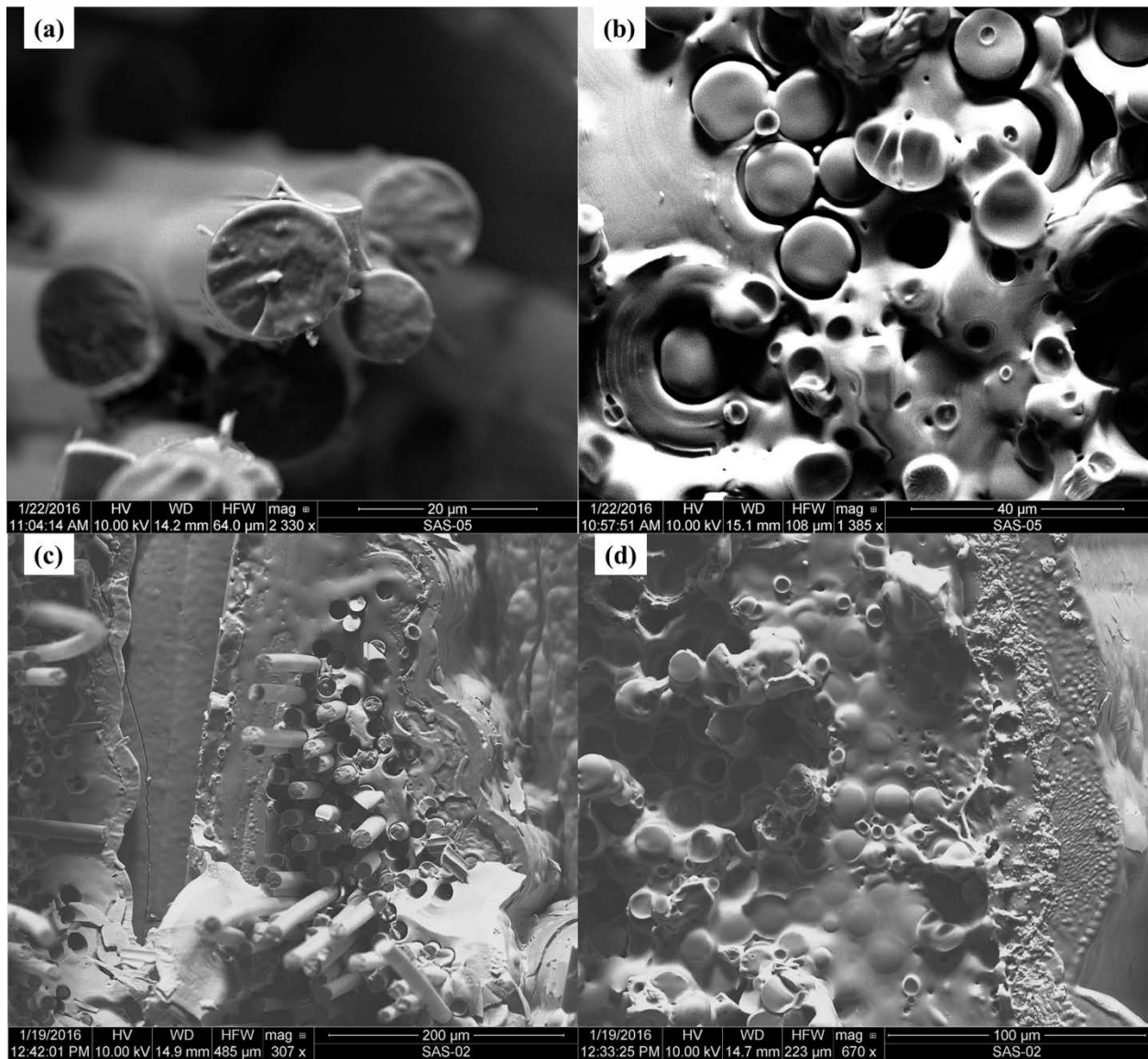
124

Figure 106: Fracture surface of the HG-shaped specimen tested in fatigue at 1300°C in steam, σ_{max} = 100 MPa, N_f = 200,000, t_f = 55.6 h.
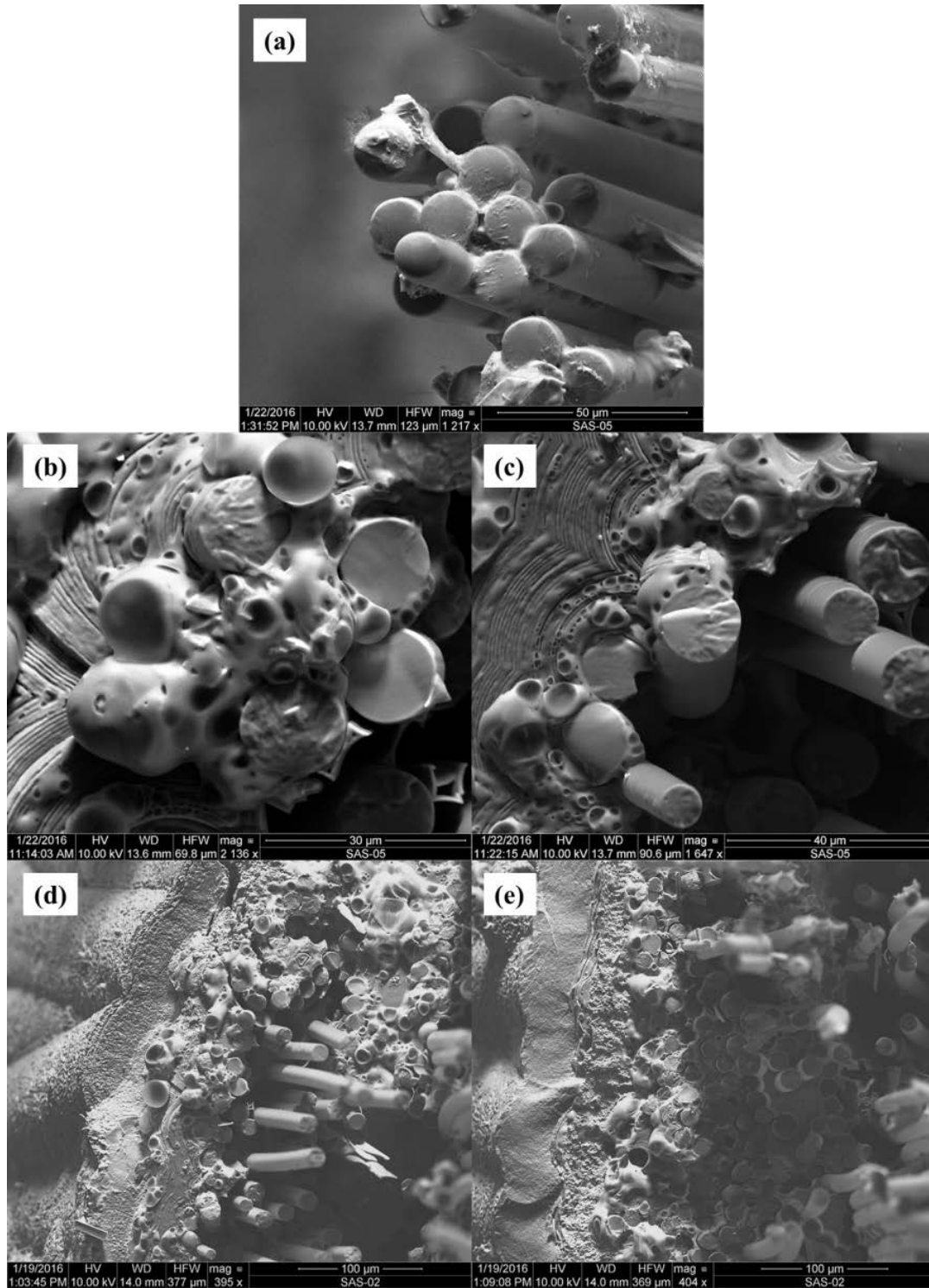
Figure 107: Fracture surface of the HG-shaped specimen tested in fatigue at 1.0 Hz with σ_{max} = 100 MPa at 1300°C in steam, (N_f = 200,000, t_f = 55.6 h). Higher magnification images showing: (a) oxidation of the fracture surfaces of the pulled-out fibers, (b) glassy phase in *oxidized* region covering matrix and fibers, (c) oxidized region with pull-out fibers, (d) and (e) *Oxidized* region in the left half of the image transitioning non-oxidized region in the right half of the image with pulled-out fibers.

Bibliography

1. Ashby, M. F. *Materials Selection in Mechanical Design.* Butterworth Heinemann, 1999.

2. Baker, A., Stuart Dutton, and Donald Kelly. *Composite Materials for Aircraft Structures (Second Edition).* Reston: American Institute of Aeronautics and Astronautics, inc, 2004. Print.

3. Bansal, Narottam P. "Tensile Strength and Microstructure of Hi-Nicalon Fibers Extracted from Celsian Matrix Composites." In *Advances in Ceramic Matrix Composites IV*, by J.P. Singh and Narottam P. Bansal. Westerville: The American Ceramic Society, 1999.

4. Bar-Cohen, Y. *High Temperature Materials and Mechanisms*. Boca Raton: CRC Press Taylor and Francis Group, 2008.

5. Chawla, K.K. *Ceramic Matrix Composites (Second Edition).* Boston: Kluwer Acadmic Publishers, 2003.

6. Chawla, Krishah K. *Composite Materials Science and Engineering (Second Edition).* New York: Springer, 1998.

7. Christensen, D. *Fatigue Behavior of an Advanced SiC/SiC Composite at Elevated Temperature in Air and Steam*. MS thesis, AFIT/GAE/ENY/09-D02. School of Engineering and Management, Air Force Institute of Technology (AU), Wright-Patterson AFB, OH, December 2009.

8. Cowles, B.A. "High cycle fatigue in aircraft gas turbines-an industry perspective." In *International Journal of Fracture, 22*: 1996: 147-163.

9. Daniel, I., Ori Ishai. *Engineering Mechanics of Composite Materials (Second Edition).* New York: Oxford University Press Inc., 2006.

10. Delapasse, J. *Fatigue Behavior of an Advaanced SiC/SiC Composite With an Oxidation Inhibited Matrix at 1200°C in Air and in Steam.* MS thesis, AFIT/GAE/ENY/10-M07, School of Engineering and Management, Air Force Institute of Technology (AU), 2010.

11. Kollins, K., Pierce, J., Przybyla, C., Private communications with AFRL.

12. Kopeliovich, D. *Ceramic Matrix Composites.* Substances and Technologies. <http://www.substech.com/dokuwiki/doku.php?id=interphases> Accessed 17 June 2015.

13. Krenkel, W. *Ceramic Matrix Composites.* Weinheim: Wiley-Vch Verlag Gmbh & Co. KGaA, 2008.

14. Parikh, N.M., "Effect of Atmosphere on Surface Tension of Glass," J Am Ceram Soc, Vol. 41, No. 1, 1958, pp. 18-22.

15. Przybyla, Craig; Private communications with AFRL.

16. Ohnabe, H., S. Masaki, M. Onozuka, K. Muyahara, and T. Sasa. "Potential Applications of Cermic Matrix Compsites to Aero-engine Components." *Composites: Part A, 30*, 1999: 489-496.

17. Opila, E.J. "Variation of the Oxidation Rate of Silicon Carbide with Water Vapor Pressure." *Journal of American Ceramic Society*, 1999: 625-636. Opila, E.J. "Variation of the Oxidation Rate of Silicon Carbide with Water Vapor Pressure." *Journal of American Ceramic Society*, 1999: 625-636.

18. Schmidt, S., H. Knabe, H. Immich, R. Mestring, and A. Gessler. "Advanced Ceramic Matrix Composite Material fo Current and Future Propulsion Technology Applications." *Acta Astronautica, 55*, 2004: 409-420.

19. Smith, W., *Principles of Material Science.* Orlando: McGraw-Hill Inc., 1996.

20. Rossol, M., Rajan, V., Zok, F. "Effects of weave architecture on mechanical response of 2D ceramic composits." *Composites: Part A*, 74: 2015: 141-151.

21. Zok, F. W. "Mechanical Properties of Porous-matrix Ceramic Composites." *Advanced Engineering Materials*, 2001: 15-23.

1. REPORT DATE (DD-MM-YYYY) 26-02-2016	2. REPORT TYPE Master's Thesis	3. DATES COVERED (From – To) January 2015 – March 2016

TITLE AND SUBTITLE Fatigue behavior of an advanced SiC/SiC composite at 1300° C in air and steam	5a. CONTRACT NUMBER
	5b. GRANT NUMBER
	5c. PROGRAM ELEMENT NUMBER

6. AUTHOR(S) Public, Michael L., 2d Lieutenant, USAF	5d. PROJECT NUMBER
	5e. TASK NUMBER
	5f. WORK UNIT NUMBER

7. PERFORMING ORGANIZATION NAMES(S) AND ADDRESS(S) Air Force Institute of Technology Graduate School of Engineering and Management (AFIT/ENY) 2950 Hobson Way, Building 640 WPAFB OH 45433-8865	8. PERFORMING ORGANIZATION REPORT NUMBER AFIT-ENY-MS-16-M-223

9. SPONSORING/MONITORING AGENCY NAME(S) AND ADDRESS(ES) Air Force Research Lab, Materials and Manufacturing Division POC: Craig Przybyla (937-255-9396) craig.przybyla@us.af.mil Wright Patterson Air Force Base, OH 45433-7750	10. SPONSOR/MONITOR'S ACRONYM(S) AFRL RXCCP
	11. SPONSOR/MONITOR'S REPORT NUMBER(S)

12. DISTRIBUTION/AVAILABILITY STATEMENT DISTRIBUTION STATEMENT A. APPROVED FOR PUBLIC RELEASE; DISTRIBUTION UNLIMITED

13. SUPPLEMENTARY NOTES This material is declared a work of the U.S. Government and is not subject to copyright protection in the United States.

14. ABSTRACT

The fatigue behavior of an advanced silicon carbide/silicon carbide (SiC/SiC) ceramic matrix composite (CMC) was investigated at 1300 ºC in laboratory air and in steam environments. The composite was manufactured using chemical vapor infiltration (CVI). The composite consisted of an oxidation-inhibited matrix, which was comprised of alternating layers of silicon carbide and boron carbide and was reinforced with laminated Hi-Nicalon™ fibers woven in a plain weave. Fiber preforms had pyrolytic carbon fiber coating with boron carbon overlay applied. Two specimen geometries were evaluated, a dog bone and an hourglass geometry. Tensile stress-strain behavior and tensile properties were evaluated at 1300 ºC. Tension-tension fatigue tests were conducted in both laboratory air and in steam at 1300 ºC at 1.0 Hz with a minimum to maximum stress ratio of R = 0.05. Fatigue behavior was evaluated for a maximum stress of 70-160 MPa in air and in steam environments. Fatigue run-out was defined as 2×10^5 cycles. Strain accumulation with cycles and modulus evolution with cycles were analyzed for each fatigue test. The CMC fatigue performance was affected little by the presence of steam. The fatigue limit was between 80 and 100 MPa. Retained tensile properties were characterized for all specimens that achieved fatigue run-out. Failure surfaces were examined to study composite microstructure as well as damage and failure mechanisms.

15. SUBJECT TERMS Ceramics, ceramic matrix composite, fatigue, high temperature, microstructure

16. SECURITY CLASSIFICATION OF:			17. LIMITATION OF ABSTRACT	18. NUMBER OF PAGES	19a. NAME OF RESPONSIBLE PERSON Marina Ruggles-Wrenn, AFIT/ENY
a. REPORT U	b. ABSTRACT U	c. THIS PAGE U	UU	147	19b. TELEPHONE NUMBER (Include area code) (937) 255-3636, ext 4641 (Marina.ruggles-wrenn@afit.edu)

Standard Form 298 (Rev. 8-98)
Prescribed by ANSI Std. Z39-18